Doctoral Dissertation
Doctoral Program in Mechanical Engineering (35th Cycle)

Data driven and physics based methods to assess the mechanical response of advanced materials

From experiments to efficient predictions

By

Alberto Ciampaglia

Supervisors:
Prof. D. S. Paolino
Prof. G. Belingardi

Doctoral Examination Committee:
Prof. W.K. Liu , Referee, Northwestern University, US
Prof. F. Berto , Referee, Università La Sapienza, ITA

Politecnico di Torino
2023

Declaration

I hereby declare that the contents and organization of this dissertation constitute my own original work and does not compromise in any way the rights of third parties, including those relating to the security of personal data.

Alberto Ciampaglia

2023

* This dissertation is presented in partial fulfilment of the requirements for **Ph.D. degree** in the Graduate School of Politecnico di Torino (ScuDo).

I would like to dedicate this thesis to my loving wife.

Acknowledgment

I want to sincerely acknowledge the unvaluable contributions of all the professors, researchers, students, and engineers that shared their thoughts, opinions and suggestions with me.

Abstract

This PhD thesis pioneers an innovative approach, merging physics-based models with data science techniques to efficiently define and predict the mechanical properties of advanced materials. Focusing on composite materials and additive manufactured metals with intricate microstructures, we aim to bridge the gap between microstructural features and material properties, vital for enhancing the design of advanced materials.

Traditional Machine Learning (ML) approaches often prioritize accuracy over physics compliance. In response, this thesis introduces the concept of Mechanistic Data Science (MDS), which combines the predictive power of ML with the grounding in physics laws. At its core, MDS integrates physics knowledge with advanced machine learning methods, offering a solution to a longstanding challenge: efficiently predicting the mechanical properties of complex materials with intricate microstructures. While the objective is clear—to establish a link between microstructural features and material properties—the true achievement lies in the methodology itself. The thesis unfolds in a series of interconnected chapters, each contributing to the overarching goal.

A Physics-Informed Neural Network (PINN) with a customized architecture is developed to learn the constitutive behaviour of orthotropic materials from the distributed strain measurements acquired with the Digital Image Correlation (DIC). Being the Neural Network (NN) a universal approximator, the proposed architecture can learn arbitrary constitutive models avoiding the definition of parametric models and defining the constitutive properties of the materials from the experimental data. With the proposed approach the full elastic constitutive model

of an orthotropic material can be defined with a single test, and different damaging laws can be inferred using the same architecture. The model is validated on artificial data - i.e., generated with a Finite Element Model (FEM) - and later applied to experimental data. This PINN approach eliminates the need for defining parametric models, allowing for rapid characterization of material properties.

Moving forward, the thesis combines DIC data with microstructural reconstructions from Fiber Reinforced Polymer (FRP) samples to characterize composite material stiffness, accounting for manufacturing-induced defects and fiber misalignment. This information contributes to the development of a Stochastic Volume Element (SVE), a mesoscale representation of the FRP, which have a microstructure sampled from the experimental reconstructions and variable material properties statistically calibrated from the experiments. When the SVE is integrated into a multiscale Finite Element Model (FEM), offers a unique capability to provide probabilistic predictions of structural responses.

The thesis further extends the application of MDS to predict the crushing behavior of origami-shaped carbon FRP structures at the part scale, optimizing design processes with a significant reduction in computational cost. The model evaluates the crushing force and the absorbed energy of the thin-walled structure by preserving the physics relationship between the two quantities, which is governed by the energy conservation law. The good accuracy of the method and the reduced computational cost, permit to perform an optimization study of the origami tube with a full exploration of the design space reducing the optimization time by 30 times. The results of the PINN are compared with the FEM, showing a remarkable accuracy of the surrogate model.

The final chapter focuses on the fatigue response of aluminium alloys produced through Additive Manufacturing (AM). By combining experimental observations of manufacturing parameters with a damage-tolerant model developed by Murakami, a customized Neural Network (NN) architecture is employed. This chapter demonstrates remarkable accuracy in predicting the fatigue response, offering designers a potent tool to assess the influence of manufacturing processes on material properties and avoid impractical experimental investigations.

The MDS methods presented in this thesis puts its roots in the governing laws of the mechanics, leveraging on the increasing data that are nowadays available thanks to innovative experimental techniques (e.g., micro-CT, DIC) and shared database, or can be reliably generated through experimentally calibrated models (e.g., FEM).

In summary, this thesis showcases the novel MDS framework, effectively combining empirical and theoretical knowledge with abundant data to advance materials science and design. While the abstracted methodology connects various chapters, it is the transformative potential of MDS that unites these diverse investigations, paving the way for future research to refine and expand upon this innovative approach.

Contents

List of Figures

List of Tables

Abbreviation	**Meaning**
ML	Machine Learning
MDS	Mechanistic Data Science
NN	Neural Network
ReLU	Rectified Linear Unit
SELU	Scaled Exponential Linear Unit
SGD	Stochastic Gradient Descent
PIDS	Physically Informed Data Science
ANN	Artificial Neural Network
ROM	Reduced Order Model
PINN	Physics-Informed Neural Network
PDE	Partial Derivative Equation
DIC	Digital Image Correlation
FEM	Finite Element Method
FRP	Fiber Reinforced Polymer
RVE	Representative Volume Element
SVE	Stochastic Volume Element
FFT	Fast Fourier Transform
DOF	Degree Of Freedom
MSE	Mean Squared Error
RMSE	Root Mean Squared Error
AE	Absolute Error
CNN	Convolutional NN
GNN	Graph NN
ICME	Integrated Computational Material Engineering
AM	Additive Manufacturing
SLM	Selective Laser Melting
SIF	Stress Intensity Factor
ELU	Exponential Linear Unit
VHCF	Very High Cycle Fatigue

1 Introduction

1.1 The new data driven scientific paradigm

The practice of science has undergone significant changes throughout its history, as new technologies and methodologies have been developed to enhance our understanding of the world around us. These changes can be characterized by four key paradigms defined in [1]: Empirical, Model-Based, Computational, and Data-Driven Science.

- Empirical Science: Empirical Science is the earliest form of scientific inquiry and is characterized by observation and experimentation. In this paradigm, experience is the only source of knowledge. Scientists would observe natural phenomena, perform experiments, and use these observations to build simple models or explanations of the world. This paradigm is best exemplified by early natural philosophers such as Aristotle, who used observation and logical reasoning to understand the world around him.
- Model-Based Science: After the scientific revolution in early 1600, the development of Model-Based Science marked a new phase in the evolution of science, characterized by the use of mathematical models to better understand complex systems. Scientists in this paradigm use mathematical models to describe natural processes and simulate their behaviour under different conditions. The models allow for the extrapolations of the system response beyond the observed domain, giving a wider understanding of the phenomena, later confirmed by experiments. The pillars of science have been built in this era, such as the law of kinematics, mechanics, and thermodynamics.
- Computational Science: The rise of Computational Science marked another important shift, characterized by the increasing use of high-performance computing and simulation to tackle problems in fields such as physics, chemistry, and biology. The invention of the computer allowed scientists to solve complex systems described by a large

number of equations, whose solution would have otherwise required an unsustainable amount of human work. Scientists in this paradigm use computers to perform complex simulations and analyse large data sets. For example, molecular dynamics simulations are used to study the behaviour of biological molecules, such as proteins, at the atomic level. Computational science gave birth to numerical models such as Density Functional Theory or Finite Element Analysis.

- Data-Driven Science: The most recent paradigm in the evolution of science, Data-Driven Science, is characterized by the central role of large, complex data sets in scientific discovery. With the increasing availability of big data and the development of new computational tools for processing and analysing these datasets, Data-Driven Science is poised to play an important role in shaping our understanding of the world. In this paradigm, scientists use Machine Learning (ML) algorithms and statistical models to identify patterns in data and make predictions about future trends. For example, scientists are using data-driven methods to predict the spread of diseases, understand the behaviour of financial markets, and even discover new species. Data-driven science leverages a huge amount of real and artificial information to develop methods with improved predictive capacity.

Each of these paradigms has been driven by advances in technology and the changing nature of scientific knowledge. Scientists today are faced with the challenge of balancing the accumulated scientific knowledge with the vast amounts of data generated from high-fidelity models, experiments, and real-world observations. To ensure the preservation of the underlying physics, while also utilizing ML algorithms to model scientific phenomena, there has been a growing interest in a new field of data science known as *Mechanistic Data Science* [2] (MDS). This field combines established mechanical principles and data collection to enhance the knowledge extraction process and improve predictive capabilities.

The following section discusses the fundamentals of MDS, giving an overview of essential concepts and approaches that can be used to develop the MDS method in the field of predictive physics.

1.2 Mechanistic Data Science

The paradigm shift in science has begun to take place in areas such as social sciences[3–5], medicine[6–8], and biology[9–13], but there are still fields where the spreading of data-driven science is limited. An example is the disciplines where the modelling tool can rely on an established mathematical understanding of physics, like solid mechanics, computational physics, or fluid dynamics.

The available data gathered in these fields are the results of centuries of scientific knowledge and a black-box algorithm without any information about it could lead to wrong prediction. Moreover, scientific problems suffer from a paucity of data while involving many variables that interact in complex and non-stationary ways. Therefore, it is expected that purely data-driven methods can give wrong predictions outside the observed domain. Another main concern about the application of this methodology is the lack of interpretability of the models. Physically based models are not only useful for making predictions, but their interpretable formulations help in gaining knowledge through the interpretation of their structure, parameters, and mathematical properties.

One way to gain explainability in ML methods is to incorporate scientific knowledge about the observed phenomena into the ML algorithm, following the MDS approach. Combining the predictive capabilities of ML algorithms with the scientific consistency and interpretability of physically-based models is a solution to the shortcomings of purely data-driven methods.

Three different types of MDS problems can be defined based on the nature of the knowledge, scientific or data-based, and how it is combined to get an understanding of the phenomena. When referring to scientific knowledge, it is of utmost importance to differentiate between two types of knowledge, namely, physical general principles such as conservation and thermodynamic laws that are widely acknowledged as capable of describing the fundamental structure of the universe, and phenomenological models such as macroscopic material constitutive relationships, which are simplification and homogenization of molecular-level interactions derived from available experimental data. While, in theory, it might be possible to derive real mechanistic constitutive relationships from first physical principles, the massive number of degrees of freedom involved in the relevant temporal and spatial scales required for real-world applications makes this a practically unattainable goal[14]. Therefore, the combination of physical principles and phenomenological models, under well-defined hypotheses, has proven to be highly effective in accurately solving complex real problems while maintaining mathematical tractability.

Defining how the scientific knowledge and the data are fused to solve the physic-based problems, we can distinguish three different types of problems (Figure 1.1) that MDS can tackle[2,15]:

1. Purely data-driven: problems with abundant data and undeveloped or unavailable scientific fundamental principles. In this scenario, a purely data-driven algorithm can model the effect of different features and their interplay on the state of the system. There is not an explicit theory associated with the problem, making unavailable any interpretation of the governing laws.
2. Limited data and scientific knowledge: problems where neither the data nor the scientific principles provide a complete solution. Problems where general models that govern the phenomena are known, like universal laws, but a precise formulation modelling the evolution of the system is missing, fall in this category. In this scenario, a specific ML algorithm can be developed to leverage a modest quantity of data that combined with scientific knowledge can lead to the development of an efficient and physically consistent predictive algorithm.
3. Known mathematical science principles with uncertain parameters: problems where a parametric description of the problem is known, and a limited amount of data is used to estimate the parameters.

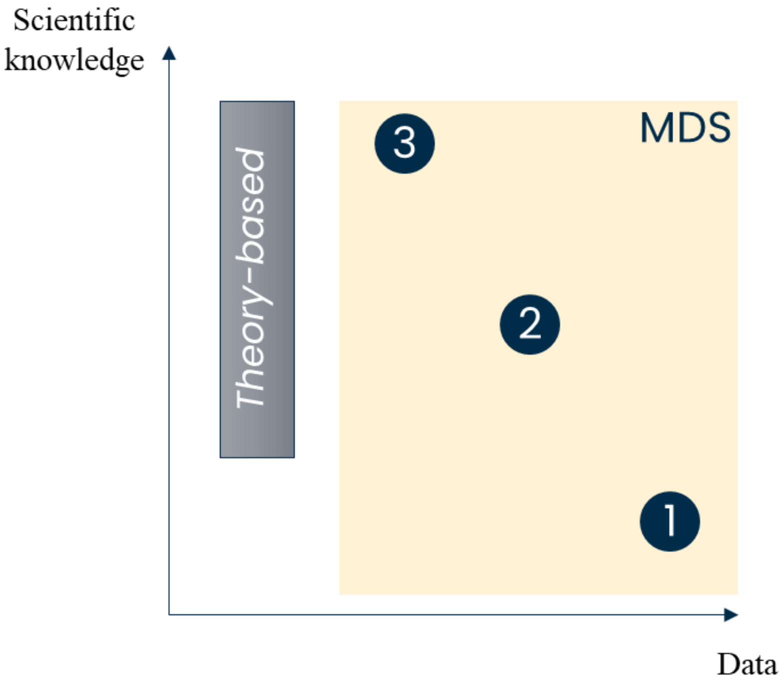

Figure 1.1 Scientific and data knowledge balance for the three types of mechanistic data science problems

MDS can be broken down into six fundamental steps: multimodal data generation and collection, feature engineering, dimension reduction, reduced order modelling, regression, and classification. The first step comprises the collection of significant data from different sources (e.g., experiments with different measurements, and high-fidelity models). The data are then processed to extract relevant information from an engineering perspective, using time-frequency-space transformations. Data are then reduced with either data-science technique or knowledge-based reductions (reduced order models) to reduce the dimensionality of the problem. Finally, deep learning models can be used to perform classification or regression tasks on the processed data and model the mechanistic phenomena.

Having laid down the fundamentals of MDS, the next section focuses on problems in the field of solid mechanics, evidencing the main challenges and how they can be tackled with MDS.

1.3 Data-driven methods in solid mechanics

Mechanical engineering is defined as the discipline of studying the design of a mechanism from the material definition to manufacturing. Over the centuries, scientific and technological progress has led to fast development and enrichment of knowledge, requiring the subdivision of mechanical engineering into more specific fields. Cauchy first introduced continuum mechanics, defined as the study of the mechanical behaviour of materials modelled as a continuum, approximating the atomistic scale to a continuum field described with partial differential equations. Solid mechanics, specifically studies the response of solid materials, especially their motion and deformation under the action of forces, temperature changes, phase changes, and other external or internal agents. The continuum description of material behaviour is a simplification of the real world, where the lower scale mechanisms originating from the atomistic scale are progressively homogenized to get a handful of models.

Three fundamental domains between which the information is propagated, have been identified:

- Process: involves the manufacturing stage where the matter is modified through temperature, force or electromagnetic fields that shape the constituents into a new material or part.
- Structure: the results of the manufacturing process in terms of size, shape, and arrangement of its constituents, such as grains, pores, and defects. It is commonly referred to as microstructure in material mechanics.
- Property: is the functional characteristic of the manufacturing product and is descriptive of the ability to fulfil a requirement. At the micro-level, properties can be stiffness, strength, fracture toughness and other material properties of the homogeneous matter. At a higher scale, the properties can be bearing load, energy absorption, buckling load, or other properties of the manufactured structure. These are sometimes referred to as “performance” in the Process-Structure-Property-Performance (PSPP) framework.

The relationship between process, structure, and property (or performance) can be understood as a hierarchical one, where the properties at each scale are determined by the properties at the smaller scales. This hierarchical relationship helps to explain the behaviour of materials and structures under different loading conditions and enables the design of advanced materials and structures with desired properties for specific applications. The purpose of this thesis is to implement MDS models to discover and/or predict this relationship over the different scales of advanced materials and structures.

Section 1.4 describes how ML models work and how they can be combined with physical knowledge to solve problems in the field of solid mechanics of advanced materials.

1.4 Machine learning methods

ML is a rapidly growing field of computational science that focuses on the development of algorithms that can learn from and make predictions about data. In recent years, ML has been increasingly applied in various scientific domains, including physics, biology, chemistry, and engineering, to name a few. In scientific contexts, ML models have proven to be effective tools for exploring complex phenomena, making predictions, and generating new insights.

ML models can be broadly classified into two categories: supervised and unsupervised. Supervised ML models are trained on labelled data, where the target variables are known, and the goal is to predict these variables based on the input data. In contrast, unsupervised ML models are trained on unlabelled data and aim to find patterns and relationships in the data without the need for predefined target variables.

In scientific applications, ML models can be trained on data generated from simulations, experiments, or real-world observations. The models can then be used to make predictions about the behaviour of the system, to identify patterns and relationships in the data, or to perform data analysis tasks such as clustering, dimensionality reduction, or anomaly detection.

1.4.1 Standard ML methods

1.4.1.1 Neural networks

The methodologies presented in this thesis mostly leverage a specific type of supervised ML model: neural networks (NN). An NN is a type of ML model that is inspired by the structure and function of the human brain. It consists of interconnected processing nodes, or "neurons," which process and transmit information through weighted connections.

Each neuron receives inputs from other neurons and applies a mathematical operation, such as a dot product or activation function, to produce an output signal. The output signal of one neuron can serve as input to multiple other neurons in the network, allowing for complex, multi-layer representations of the data (Figure 1.2).

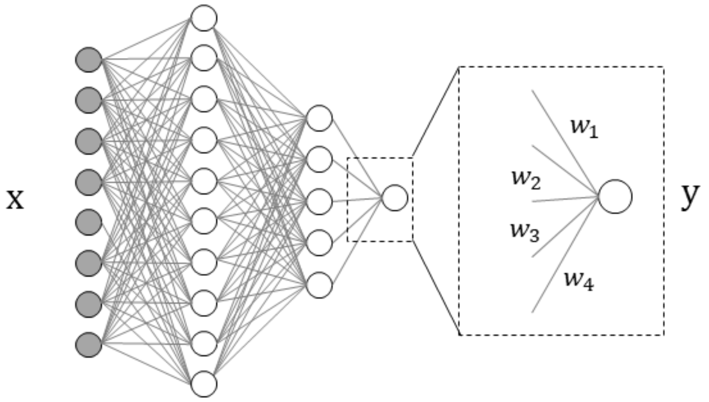

Figure 1.2 A layered structure of a neural network with one input layer, two hidden layers and an output layer. In the dashed box, the representation of the weighted inputs of the last layer.

The fundamental operation in each neuron is described by Equation 1.1:

$$y = \mathcal{A}(\boldsymbol{w}\,\boldsymbol{x} + b), \tag{1.1}$$

where w is the weights vector that multiplies the inputs x and b is the bias, a scalar added to the dot product. The weighted sum is passed to an activation function $\mathcal{A}$, which should satisfy the following requirements:

- Non-linearity: An activation function should introduce non-linearity into the neural network, allowing it to learn and model complex relationships in the data.
- Differentiability: The activation function should be differentiable, meaning its derivative can be calculated, which is necessary for backpropagation, the process used to adjust the weights of the network during training.
- Bounded Output: The activation function should have a bounded output, typically between 0 and 1 or -1 and 1, to ensure that the output of each neuron remains within a specific range and does not become unbounded during training.
- Monotonic Behaviour: The activation function should have a monotonic behaviour, meaning its output should either increase or decrease as its input increases, to ensure that the network can converge to a solution during training.
- Computational Efficiency: The activation function should be computationally efficient to compute, as it will be applied to each

neuron in the network during forward propagation and backpropagation.

In conclusion, an activation function in a neural network should be non-linear, differentiable, bounded, monotonic, and computationally efficient. These requirements are necessary for the neural network to learn complex relationships in the data and to converge to a solution during training. The most common activation functions are reported in Figure 1.3, with the corresponding formulation reported in Table 1.1.

Name	**Expression**	**Parameters**
Linear	$\mathcal{A}(x) = x$	-
Rectified Linear Unit (ReLU)[16]	$\mathcal{A}(x) = \begin{cases} 0 \; if \; x < 0 \\ x \; if \; x \geq 0 \end{cases}$	-
Leaky ReLU	$\mathcal{A}(x) = \begin{cases} \alpha x \; if \; x < 0 \\ x \; if \; x \geq 0 \end{cases}$	α
Scaled Exponential Linear Unit (SELU)[17]	$\mathcal{A}(x) = \lambda \begin{cases} \alpha(e^x - 1) \; if \; x < 0 \\ x \; if \; x \geq 0 \end{cases}$	α, λ
Hyperbolic Tangent	$\mathcal{A}(x) = \tanh(x)$	-
Sigmoid	$\mathcal{A}(x) = \frac{x}{1 + e^{-x}}$	-

Table 1.1 Neural network activation functions and their expression.

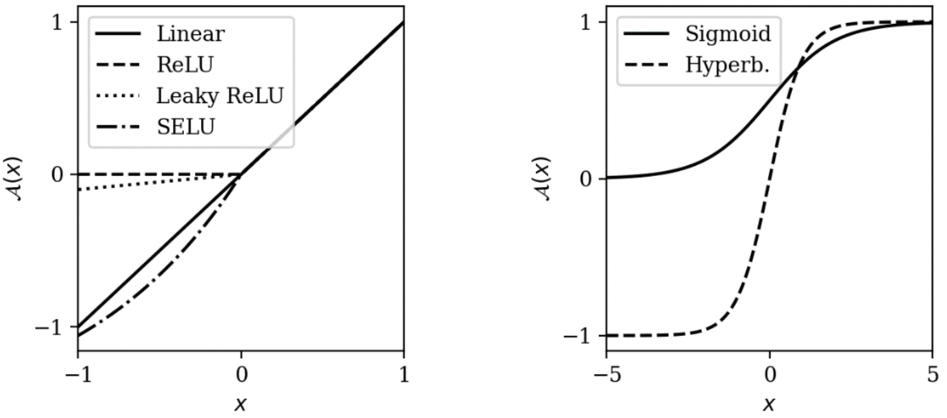

Figure 1.3. Linear or modified linear (a) and non-linear (b) activation functions.

The activation functions on the output layers of the NN constrain the output values. For example, a ReLU operating on the output layers will force the network to exclusively output positive values. The linear function is usually preferred on the output layers of a regression NN, while its usage in the hidden layers vanished the approximation capabilities of the method, transforming the network into a linear regressor.

The weights w of the connections between neurons and the bias are adjusted during the training process to minimize a predefined loss function $\mathcal{L}$, which measures the discrepancy between the model predictions and the actual target values. The set of inputs x which corresponds to the known output y is named dataset, typically arranged in an N-by-m matrix, being N the number of observations and m the number of variables of the observed system. The dataset is decomposed into two sub-sets, namely the training and testing data: the first is used in the training process to calibrate the parameters of the model, while the latter is used to evaluate the interpolation and extrapolation performance of the model outside the training dataset and adjust the hyperparameters of the ML model to avoid over-fitting and under-fitting problems. The common ratio between training and testing data is 0.8, an explanation of this has been given by [18]. The goal for the training phase is to find the optimal set of weights that allow the network to make accurate predictions on the training data. The training of an NN can then be formulated as the optimization problem described in Equation 1.2:

$$\min_{\boldsymbol{w},\boldsymbol{b}} \mathcal{L}\left(y_{target},\ \ NN(x; w, b)\right) \tag{1.2}$$

The weights in a neural network are updated during the training process using an optimization algorithm, such as gradient descent.

The gradient of the loss function with respect to the weights in the network is computed at each iteration using the back-propagation algorithm[19]. The gradient gives a hint about the direction in which the weights should be adjusted in order to minimize the loss.

Once the gradient is computed, the weights are updated by subtracting the gradient multiplied by a learning rate, which determines the step size of the update. The learning rate controls the speed at which the weights are updated and must be set carefully to avoid overshooting or oscillating around the optimal solution. The process of computing the gradient and updating the weights is repeated multiple times, with each iteration referred to as an epoch. The training continues until the loss function reaches a minimum or until a maximum number of epochs is reached.

Adam[20], Adagrad[21], and SGD (Stochastic Gradient Descent)[22] are optimization algorithms commonly used to train neural networks using backpropagation. Adam and Adagrad are both variants of gradient descent, which is the main algorithm used to train neural networks. They differ from standard gradient descent in that they adjust the learning rate during the training process to ensure faster convergence and improved performance. SGD is a more general optimization algorithm that can be used for various types of models, including neural networks. SGD is particularly well-suited for large-scale and highly complex datasets and is widely used due to its simplicity and efficiency.

1.4.2 Physically informed data science methods

The MDS methods can be classified based on how the known physics is incorporated into the ML algorithm. Three main strategies to combine scientific knowledge with the data driven method are presented in this section: 1 - physics included in the dataset, 2 - physics included in the ML model, and 3 - physics included in the training process.

1.4.2.1 Physics included in the dataset

The least intrusive way to integrate physics knowledge into an ML model is via the dataset, making use of standard ML techniques applied to data generated by physically based models. In the case of supervised learning, the dataset is generated through a known model Y_{Phy}, giving as output the target data according to Equation 1.3:

$$y = Y_{phy}(x) \tag{1.3}$$

In this case, the mapping $x \rightarrow y$ is deputed to an ML method that can learn the inherent relationship between the input and output of the system regardless of the governing physical equations. This application goes under the name of metamodel (i.e., "surrogate models"), whose goal is to replace standard simulation techniques with a much more computationally convenient model that allows for real-time estimations. Numerous applications of metamodels can be found in material modelling, where an Artificial Neural Network (ANN) is trained to learn the stress-strain relations of advanced materials [23–29] from detailed and computationally expensive micromechanical simulations. Applications of ML methods as surrogate models can be found in the field of material mechanical characterization where ANN are demanded to infer the fatigue models [30–33], damage parameters of composites [34,35] or nonlinear constitutive laws [36].

ML-guided reduced order method (ROM) falls in this category as well. A ROM is a model that reduces the computational cost of simulations, reducing the number of degrees of freedom while keeping its accuracy above an accepted value. Mathematically, considering the model $\mathcal{M}(x)$ mapping the solution μ from the domain S of the variable x with dimension D, the ROM $\mathcal{R}(x)$ is a mapping of reduced dimension d<<D such that:

$$||\mathcal{R}(x) - \mathcal{M}(x)|| < \epsilon \quad \forall x \in S, \tag{1.4}$$

being ϵ a small parameter and $||\cdot||$ a suitable norm.

ML methods can be used to define the reduced space where the input is projected before being processed by the ROM. The most common techniques in this area are Autoencoders, a neural network trained with the same input and output data, with a symmetric structure and a middle layer with the number of neurons reduced with respect to the number of features. The values at the middle layers, namely the latent variables, encode the data information that is subsequently decoded by the right hand of the structure. Alternatively, a clustering algorithm can be used to discover the space of latent variables, which is a simplified representation of the physical structure. In [37,38] k-means clustering is used to define sub-clusters of the heterogeneous domain from the elastic response by successive homogenisation and accelerate the solution using the Lippman-Schwinger equation by reducing the degrees of freedom.

1.4.2.2 Physics included in the ML model

One way to combine physical knowledge with ML methods is to shape the architecture of the algorithm in a way that follows the cause-effect relationship of the variables as described by the physical model in hand. This allows for the partial opening of the "black box" of ANNs by mimicking the known governing equations and producing latent variables that resemble the physical parameters of the known model. In the same way, the structure of the model can be shaped to preserve the mathematical features of the output that must be complied with to fulfil the physical constraints. Modified ANN architectures have been developed to predict positive definite constitutive relations[39], the homogenized response of heterogeneous materials[40,41], embed the geometrical description of the microstructure to predict plasticity laws [42,43] or homogenised response[44], translate a finite element mesh into an ANN structure to predict the optimal mesh refinement[15,45].

1.4.2.3 Physics included in the training process

When the physics knowledge can be quantified by a known equation that governs the observed phenomena and is expressed in terms of the variables of the dataset, the physics compliance can be induced by modifying the loss function. This approach leads to two advantages:

- Reducing the amount of data needed to build an accurate ML model.
- Obtaining more robust and stable solution schemes complying with the physics of the problem.
- Allow for the control of the balance between data-driven and scientific knowledge by weighting the loss terms.

This technique can be generally described by Equation 1.5:

$$\mathcal{L}' = \alpha\mathcal{L} + \beta\mathcal{L}_{phy}, \tag{1.5}$$

where the loss function of the ML method, $\mathcal{L}$, is combined with the regularization loss terms that incorporate the physics of the problem, $\mathcal{L}_{phy}$, to get the modified loss function $\mathcal{L}'$. If α=0, the model is trained only on the physics of the system, whereas if β=0 it recovers pure Data Science ML methods. From an MDS perspective, the weighting parameters α and β control the type of problem shifting from type 1 to 2. The weighting scalars serve two main scopes:

- Balancing the data-driven and physically based knowledge in the training process.
- Homogenizing the order of magnitude of the two terms could be drastically different, since the first depends on the magnitude of the data, while the seconds are an expression of the physical relationship and can yield quantities with different orders of magnitude.

This approach is commonly referred to as Theory Guided ML, a family of methods that contains the most popular MDS algorithm: Physic-Informed Neural Networks (PINNs)[46]. PINNs work as standard NNs with a regularization term enforcing the known physic, as described by Equation 5. The most popular application of the PINNs is solving Partial Differential Equations (PDE), where the input of the network is the spatial or temporal coordinates and the excitation quantity, while the output is the solution of the PDE. The loss term is then constructed by deriving the NNs, leveraging on the derivability required by the backpropagation, to compute the residual of the PDE.

PINNs have been adopted in the field of solid mechanics to predict the hyperelasticity models preserving the strain energy convexity[43], to predict the fatigue response of Additively Manufactured parts preserving the characteristic trend of the fatigue strength with the number of cycles at failure [47], to solve solid mechanic problems with arbitrary boundary conditions[48,49].

Physically based data science methods described in this dissertation span the fields of characterization, material modelling, surrogate modelling and fatigue prediction leveraging on the concepts introduced in this introduction. More specifically, each methodology presented in this thesis can be framed within the PIDS categories defined below and the resulting models can be used to define domain relations in the process-structure-properties framework previously introduced, as reported in Table 1.2.

Chapter	Title	From	To	Type	MDS approach
2	Data-driven material characterization	Property	Structure	2	Modified architecture + modified loss
3	Data-driven statistical multiscale characterization and modelling	Structure	Property	3	Modified loss
4	Prediction of an origami tube crashing	Structure	Property	2	Modified architecture + modified loss
5	Prediction of the effect of process parameter on the fatigue response of AM metals	Process	Property	2	Modified architecture

Table 1.2 Methodologies described in the dissertation with respective MSD problem types, MDS treatment strategy and modelled P-S-P domain relation.

Chapter 2 describes a PINN with a modified architecture that learns the constitutive equation of linear and non-linear orthotropic materials from the full-field displacements and applied loads measured during a tensile test. It is a type 2 problem, where the governing equations are known and there is enough data to use ML models for inferring the internal state equations.

Chapter 3 shows a data-driven statistical method that combines the full field displacements and applied loads with a 3D reconstruction of the material microstructure measured with Computer Tomography to calibrate the statistical multiscale parameters of a glass fibre composite. It is a type 3 problem where the data are used to define the model parameters and their uncertainty.

Chapter 4 discusses the development of an MDS model that harnesses the predictive capability of ML to get a surrogate model of an origami-shaped tube axial crushing predicting the force and energy response for different geometrical configurations.

Chapter 5 presents a PINN with an intrusively modified architecture mimicking the empirical formulations describing the relation between the defect size, material microstructure and fatigue response of metal. The model predicts the effect of process parameters on the fatigue strength of additively manufactured metals.

2 Data driven material characterization with Physics Informed Neural Networks

2.1 Introduction

In the last two decades, huge progress in the field of experimental mechanics has been made, leading to the development of new instruments capable of providing precise and distributed measurements of mechanical properties. Among others, the DIC technique, introduced in the early 1990s by a group of researchers led by Dr Donald K. Chang at the National Institute of Standards and Technology (NIST) in the United States, opened the door to full-field measurements of the superficial displacement and strains, moving away from localized strain information coming from the extensometer or strain gauge. The enormous advantage introduced by this technique has pushed its development and spreading among the scientific community, and it is nowadays considered a common technique in the mechanical engineering community. In the field of material characterization, the availability of full-field strain measurements can overcome the sparse nature of the common experimental exploration where high dimensional strain-stress space is explored along a few trajectories and elaborated models are used to extrapolate the constitutive equation outside the observed domain. DIC offers the opportunity to track the evolution of the strain in numerous points of the observed structure, bringing several advantages:

- Observable local phenomena: the full-field measurements enable the measurements of localised strains due to cracks, Luder’s bands, and other localized phenomena.
- Observable heterogeneity: the heterogeneous strain field in welded joints, composite materials or polycrystals can be observed and leveraged to understand the lower-scale mechanism of heterogeneous structures.

- Accelerated characterization: heterogeneous strain fields are influenced by a greater number of constitutive parameters than homogeneous ones. This opens a new route for material characterization since a greater number of constitutive parameters can be potentially identified at the same time [50]

Even if complex strain configurations are measurable, the material stress is an abstraction that cannot be experimentally measured, therefore the calibration of the material model based on full-field displacements (and strains) is not trivial and different evolving approaches can be found in the literature.

2.1.1 DIC for material model calibration

To leverage the DIC data for characterizing the constitutive relation of materials, researchers have developed different techniques minimizing a cost function defined over the measured displacements or strains. Algorithms such as constitutive equation gaps, reciprocity gaps or equilibrium gaps directly use the measure of full-field quantities to discover the constitutive parameters minimizing the cost function (for a review refer to [51]). Different approaches couple the full field measurements with numerical simulation, continuously updating the material parameters of the numerical model until the predicted strains match the DIC measurements (Finite Element Model Updating, FEMU)[52].

The model-based methods imply the choice of a material model beforehand, assuming that there is previous knowledge about the material behaviour and a parametric model to be fitted. On the other hand, the data-driven identification method gets rid of any assumption on the stress-strain relationship but limits the knowledge to the observed region of the space field. The method is indeed limited by the experiments, which should explore all the material states that will be simulated with a data-driven mechanic method. Here, an NN constitutive model is proposed, trained on the full field displacement measured with the DIC technique. NNs have been demonstrated to be global approximators if trained with enough data [53], therefore its flexible architecture can mimic any constitutive model and extrapolate results beyond the observed states. Recent applications of NN to model the material response are discussed in the following.

2.1.2 MDS method for material modelling

The application of NNs for modelling the mechanical response of materials has been intensively investigated in the last decade. Ghaboussi et al. [54–56] first explored the application of ANNs to material modelling, showing their promising capabilities. Since then, the interest towards these methods has been continuously increasing due to the computational efficiency and approximation capability that they can offer compared with phenomenological models.

The calibration of material models can generally follow two procedures:

1. Inferring the material response from explicit data, such as pairs of stress-strain, stress-strain energy, or stress-strain increments. This data is usually consisting of homogenized results from high-fidelity sub-scale models, or experimental measurements properly post-processed. NNs have been trained on stress-strain data to model the response of hyper-elastic materials [57], non-linear elastic composites [58], crystal elastic materials [59], viscoelastic materials [60], multiscale porous materials [26,61], composite with progressive damage [28,35], and plastic materials [25]. This strategy allows surrogating the material models but has the drawbacks of directly learning from the stress quantities, which are not directly measurable experimentally.
2. Deducting the material response from indirect measurable quantities, such as reaction forces of structures or full field displacements. Application of NN to the calibration of material models through indirect measurements are few due to the novelty of the research field. NNs have been trained on indirect data generated with sub-scale models to calibrate the elastic response of composite [39,62] and the nonlinear response and damage of composites [63,64]. These methods have the advantage of being directly trainable with measurable quantities, without requiring a data generation procedure (as for the cases where the stress is computed with micromechanical analysis) or post-processing. However, there is generally no closed-form solution to these problems that requires an optimal design of the optimization strategy.

Most of the NN proposed in the mentioned studies present common architecture and training strategies, without using any physical knowledge of the material response. Some applications of MDS have been recently proposed to get constitutive models complying with the strain energy convexity [39,65], to calibrate inclusion shape and material properties from homogenised response [66], to get the homogenized response of composite from the constituent properties [40,41].

In this work, an MDS model is developed to discover constitutive equations of the material from global force and DIC displacement observations, while complying with the governing equations. The idea is to learn the material response from the full-field strains and global force calibrating the parameters of a neural network with a custom architecture. The NN architecture:

1) preserves the strain convexity of the material model by predicting a positive definite and symmetric stiffness matrix;
2) conserves the decoupling of the axial and shear mechanisms.

The loss function is computed as the weighted sum of three terms:

1) the difference between the external energy and the external energy;
2) the difference between the boundary force, computed from the stress at the boundary, and the applied force;
3) the divergence of the stress field.

Following the taxonomy introduced in Chapter 1, the method falls within the second category of problems where the MDS model is built with modified loss functions and custom architecture. The applicability and the accuracy of the method are first analysed based on virtual tests of composite laminates with a linear orthotropic model. Then, the capability of learning nonlinear response is tested on additional virtual tests where shear damage is introduced with a linear and cubic formulation. Finally, the procedure is applied to experimental data of carbon fibre woven samples to learn the material response. The remainder of the Chapter is organized as follows. First, the finite element model used for the virtual tests and the experimental procedure used to test the CFRP is described in Section 2.2, including the material description. Then in Section 2.3 the general framework for learning the constitutive equations is presented, specifically the NN architecture and the training process are described. After that, the accuracy of the method and the results are discussed for the different cases in Section 2.4. In Section 2.5 the influence of the model parameters on the accuracy, computational time and extrapolation capabilities are analysed. Finally, the conclusions about the capabilities of the proposed methodology are drawn in Section 2.6.

2.2 Models and experiments

2.2.1 Virtual tensile test of orthotropic materials

2.2.1.1 Orthotropic elasticity

A Finite Element Model of a tensile test coupon of dimensions 25mm by 150 mm with a 2.5mm thickness has been created in the LsDyna environment. Given the thin shape of the structure, shell elements with 4 nodes and 8 integration points on the plane have been used, with an average mesh size of 1 mm. The displacements along the x, y and z axis of the fixed nodes have been constrained, while a displacement of 5mm in the y-direction has been applied to the loading edge, being the remaining degrees of freedom fixed. The specimen has been modelled with 4 layers of 0.66 mm thickness each with 3 integration points in the thickness per layer, yielding a total laminate thickness of 2.5 mm, with the PART_COMPOSITE keyword available in the LsDyna environment. The layer orientation with respect to the specimen main direction θ is kept constant through the layers.

The material model *MAT_058 LAMINATED_COMPOSITE_FABRIC has been used with the material parameter reported in Table

Table 2.1. Material parameters of the orthotropic elastic model.

E_1 [GPa]	**E_2 [GPa]**	**G_{12} [GPa]**	**ν_{12} (= ν_{12})**
48	48	2.5	0.14

The tests have been simulated at 6 different values of θ, ranging from 0 to 45°, given the symmetry of the material response.

2.2.1.2 Non-linear orthotropic elasticity

The same model has been used to simulate the response of a non-linear orthotropic elastic material with the shear stress following the nonlinear damage law[67] described in Equation 2.1:

$$G_{12} = \begin{cases} G_{12}^0 & if\ \gamma_{12} < \gamma_{12}^0 \\ G_{12}^0\left(1 - \left(\dfrac{\gamma_{12} - \gamma_{12}^0}{\gamma_{12}^f - \gamma_{12}^0}\right)^{\beta}\right) & if\ \gamma_{12} \geq \gamma_{12}^0 \end{cases}, \tag{2.1}$$

where γ_{12}^{0} and γ_{12}^{f} are the damage initiation and failure shear strain, respectively, and β is the damage exponential. The formulation yields a maximum shear stress τ_{max} given by Equation 2.2:

$$\tau_{max} = G_{12}^{0}\left(\frac{1+\beta}{\beta}\right)^{\beta}\left(\gamma_{12}^{f} - \left(\frac{1+\beta}{\beta}\right)\gamma_{12}^{f\left(\frac{1+\beta}{\beta}\right)}\right) \tag{2.2}$$

A representative curve of the shear model with β equal to 0.33 is given in Figure 2.1.

The model has been implemented in LsDyna through a defined curve in the material model MAT_58.

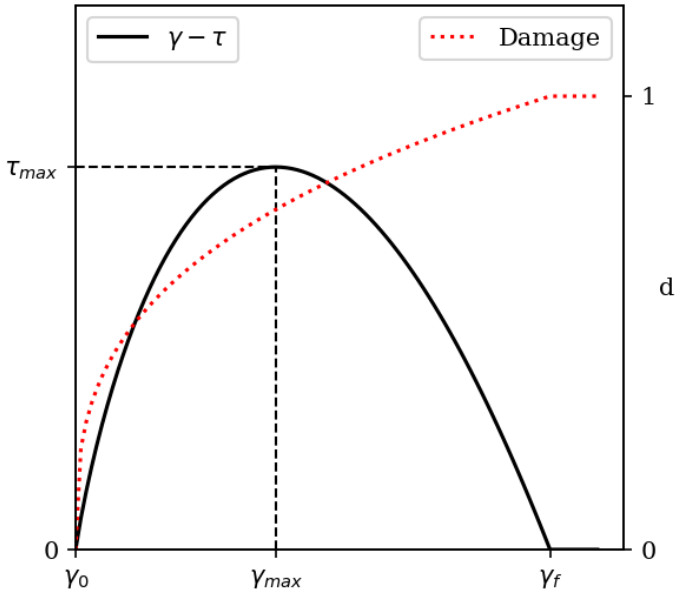

Figure 2.1. The shear damage law with a cubic trend of the damage variable with the applied engineering shear strain

2.2.2 Experimental test of CFRP

The specimen used for the experimental validation of the PINN are different in shape and stacking sequence from the one modelled with the FEM in the previous section. The composite materials studied are carbon fibre-reinforced epoxy prepreg from Microtex Composite (GG630 T125 12K, 37% resin). The matrix is an E3-150 resin, reinforced with a 2 × 2 twill carbon fiber fabric. A laminate with a [0/90/0] stacking sequence was manufactured by hand layup and autoclave curing, with an average thickness of 2 mm. Rectangular specimens measuring 250 (l) by 24 (w) mm were cut from the manufactured plate using a CNC machine. Tensile tests were conducted with an Instron 8001 hydraulic universal testing machine with a procedure adapted from the ASTM D3039 standard [68], at a quasi-static displacement rate of 2 mm/min. At least three specimens for each configuration were tested and mean values were considered. The free span of the specimen between the grips measured 145 mm. All tests were recorded with an 8.9 MP stereo camera system, imaging the entire specimen. To perform DIC, the specimens were airbrushed with a black-on-white speckle pattern (Figure 2.2b). The speckle images were processed using Correlated Solution's VIC 3D 9.1.6 DIC software, selecting an optimal subset size of 31 px and a step between the subsets of 6 px, which is less than 1/3 of the subset size following the indications in the literature [68]. The load was measured with a 100 kN load cell, while DIC was used to monitor displacement and strains on the specimen surface. Three samples were tested for each configuration.

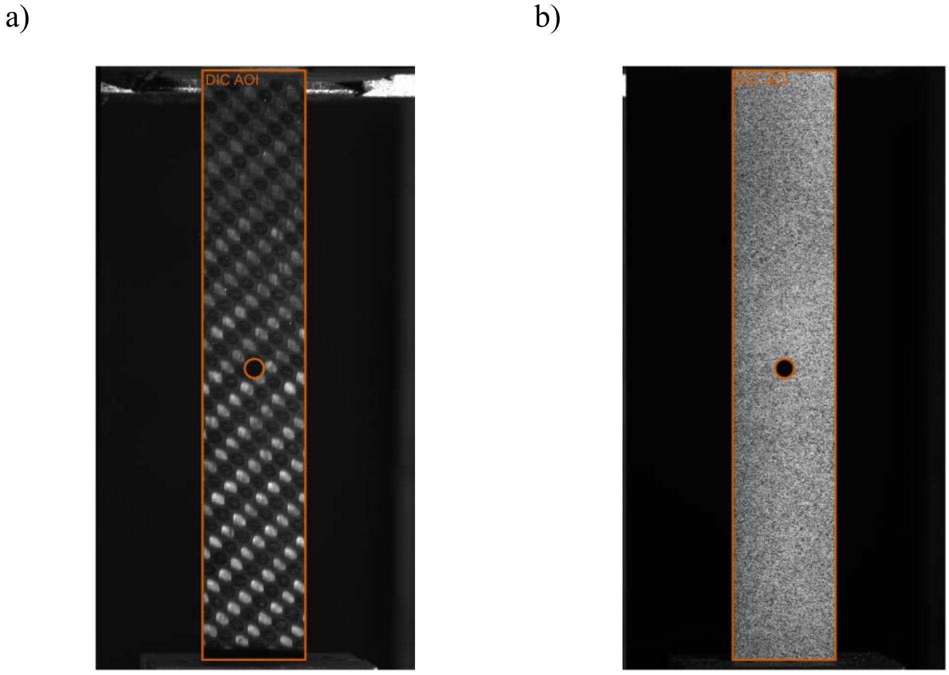

Figure 2.2. An example of a specimen on the test fixture, captured with one of the cameras used for DIC: (a) reference image used to build the model, (b) speckle image taken during testing. The DIC area of interest is overlayed on both images.

2.3 Data-driven models

The objective of the proposed method is to extract as much knowledge as possible from the experimental observation while complying with the physical constraints defined in solid mechanics. The balancing of these two sources of information translates into a progressive restriction of the solution space: in a purely data-driven method, any assumption is made on the stress-strain relation, that could lead to the violation of the physics laws; on the other hand, pre-defining a parametric constitutive model ensure the compliance of the trained model to the mechanical laws but cannot fully exploit the large dataset, translating into a parameter calibration procedure.

The identification of the constitutive relationship is an optimization problem, whose cost function is drawn from the energy balance and equilibrium equation, as will be described in the following. In this section, the data driven framework is first described and the governing equations are laid down. Following, the integration of the neural network in the framework is discussed and the integration of the continuum mechanic knowledge with the data-driven method is formulated introducing the PINN.

2.3.1 Data driven framework

The proposed framework for learning the constitutive relationship between stresses and strains from the full-field displacement measured with DIC is represented in Figure 2.3.

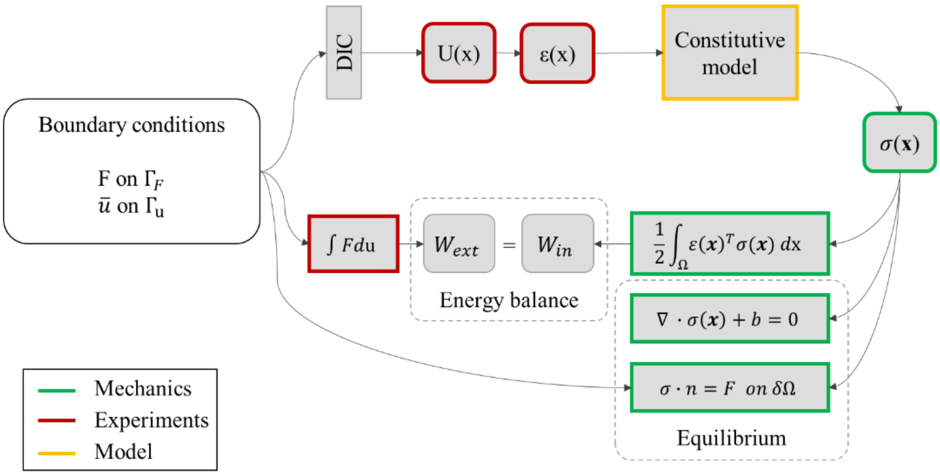

Figure 2.3. The proposed workflow to learn the constitutive model from the full field displacement measured with Digital Image Correlation

The testing configuration can be formulated as a constrained displacement at the fixed end of the specimen and an applied displacement (or load) on the moving head. Using the DIC method, the displacement field of the specimen surface is computed in the Lagrangian frame, being the reference system fixed with the testing machine. Using a stereo camera system, the 3D DIC can be applied, and the displacement $\mathbf{U}(\mathbf{x})$ is defined by its components (u_x, u_y, u_z) in the discrete points of the grid. Introducing an interpolation of the displacement on the mesh, the strains can be computed as explained in Section 2.1.2, recalling the compatibility formula expressed with Equation 2.3:

$$\boldsymbol{\varepsilon} = \frac{1}{2}(\nabla \boldsymbol{u} \cdot \nabla^T \boldsymbol{u})\,. \tag{2.3}$$

Introducing the constitutive relationship between the strains and the stresses, we can define the constitutive model $\mathcal{C}$ as a mapping from the strain to the stress space with Equation 2.4:

$$\boldsymbol{\sigma}(\boldsymbol{x}) = \mathcal{C}(\boldsymbol{\varepsilon}(\boldsymbol{x}), \lambda) : \mathbb{R}^3 \rightarrow \mathbb{R}^3 \tag{2.4}$$

In the case of history-dependent materials (e.g., damage, plasticity) the constitutive relations depend on the state variables λ, accounting for the irreversible material transformation at the microstructural level. From the computed stress, the material strain energy can be formulated with Equation 2.5:

$$W_{int} = \frac{1}{2}\int_{\Omega} \boldsymbol{\varepsilon}(\boldsymbol{x}) : \mathcal{C}(\boldsymbol{\varepsilon}(\boldsymbol{x}), \lambda) d\boldsymbol{x}\,. \tag{2.5}$$

According to the first principle of thermodynamics, the change in the internal energy must be equal to the sum of the work done on the system, W_{ext}, and the heat exchanged with the environment, Q, which, in the case of quasi-static loads, can be neglected. The work done on the system is computed from the applied load with Equation 2.6:

$$W_{ext} = \int_{t_0}^{T} F(t) d(t) dt\,, \tag{2.6}$$

where $F(t)$ and $d(t)$ are the imposed force and displacement at the boundary, respectively. The external work can be decomposed into surface and volume terms with Equation 2.7:

$$W_{ext} = \int_{\partial\Omega} \bar{t}(x) \cdot u(x) d\partial\Omega + \int_{\Omega} b(x) \cdot u(x) d\Omega, \tag{2.7}$$

being $\bar{t}$ and b the traction and body force terms, respectively, and $\partial\Omega$ the boundary surface where the traction is applied.

Combining Equations 2.5 and 2.6, Equation 2.8 relating the measurable quantities F, u, ε with the constitutive model $\mathcal{C}$ is obtained:

$$\int_{t_0}^{T} F(t) d(t) dt = \frac{1}{2} \int_{\Omega} \boldsymbol{\varepsilon}(\boldsymbol{x}) \colon \mathcal{C}(\boldsymbol{\varepsilon}(\boldsymbol{x}), \lambda) d\boldsymbol{x}. \tag{2.8}$$

The calibration procedure based on the full-field displacement can be interpreted as an optimization scheme defining the mapping function $\mathcal{C}$ that minimizes the difference between the internal and external energy.

Alongside the energetic balance, the equilibrium of the internal and external forces must be valid. Introducing the balance of linear momentum under a static and stationary condition, the continuum equilibrium can be formulated with Equation 2.9:

$$\begin{gathered} \nabla \cdot \sigma(x) + \rho(x) b(x) = 0, x \in \Omega \\ \sigma(x) \cdot n = \bar{t}\; x \in \Gamma_N \, , \end{gathered} \tag{2.9}$$

being ρ the local density of the continuum.

To comply with the equilibrium of angular momentum, the stress should be symmetric (Equation 2.10):

$$\sigma = \sigma^T \, . \tag{2.10}$$

The strain energy convexity requires the strain energy to be positive, implying that the constitutive mapping $\mathcal{C}$ is positive definite, either it is in the matrix or functional forms.

Material models are required to be frame indifferent, meaning that the constitutive relationship between the applied strain and resultant stresses must be independent of the observer frame. While this is always confirmed for isotropic materials, being its response independent of the directions, in the case of non-isotropic materials it should be guaranteed by properly projecting the strain states into the material reference. Isotropic constitutive models can be represented by isotropic manifold, it can be easily understood by recalling the isotropic elasticity theory with Equation 2.11:

$$\sigma = \lambda Tr(\boldsymbol{\varepsilon}) + \mu\boldsymbol{\varepsilon}\,, \tag{2.11}$$

where $Tr(\cdot)$ denotes the trace operator, and λ and μ are the Lame coefficients directly related to the Young modulus E and the Poisson coefficient ν. Being the stress related to strain invariants, it is independent of any rotation of the strain to a new reference system, making it frame indifferent.

In the case of anisotropic materials, this is not true because the material response is different along the different material directions and a rotation of the strain tensor would lead to a different material response. Therefore, it is needed to map the strain into the principal material direction before computing the stress response, otherwise, the material would exhibit a different constitutive law by varying the observer frame. Generally, the response of anisotropic materials can be expressed with Equation 2.12:

$$\sigma = T_\sigma^{-1} C T_\varepsilon \varepsilon \tag{2.12}$$

Where T_σ and T_ε are the rotation matrix mapping the stress and the strain, respectively, from the observer frame to the principal material reference system. C is the constitutive matrix that is frame indifferent, while $T_\sigma^{-1} C T_\varepsilon$ is the stiffness matrix in the observer frame and changes its direction with respect to the material ones.

2.3.2 Neural Network

In the proposed network, the loss function $\mathcal{L}$ is defined with Equation 2.13:

$$\boldsymbol{\mathcal{L}}(\boldsymbol{\varepsilon_T};\boldsymbol{\theta}) = \int_{t_0}^{T} F(t)d(t)dt - \frac{1}{2}\int_{\Omega} \boldsymbol{\varepsilon_T}(\boldsymbol{x}) : \boldsymbol{\mathcal{N}}(\boldsymbol{\varepsilon_T}(\boldsymbol{x});\boldsymbol{\theta})d\boldsymbol{x} \tag{2.13}$$

The integral formulation of $\mathcal{L}$ does not allow for the computation of the error at each material point, since the full-field strain values are integrated over the domain Ω and compared with the external energy. To allow for the computation of $\mathcal{L}$, the material states have been grouped into batches, each containing the material states of the entire structure at time T. A cumulative batch loss is defined to perform the integral of Equation 2.13 to get the loss value. The training of the neural network is an optimization problem in the form of Equation 2.14:

$$\bar{\boldsymbol{\theta}} = \min_{\theta} \boldsymbol{\mathcal{L}}(\boldsymbol{\varepsilon_T}, \boldsymbol{\theta}), \tag{2.14}$$

being $\bar{\theta}$ the trained parameters and $\mathbf{\theta}$ the hyperparameters.

The training algorithm of the NN is described with Algorithm 2.1, where at each iteration of the training process the loss is computed at each load step and back propagated to the NN neurons to update the weights and biases.

Algorithm 2.1

```
Neural Network Pseudo code
Initialize random $\theta = \{\boldsymbol{w}, \boldsymbol{b}\}$
while i<n_epochs
   for each load step N
      Compute $\boldsymbol{\sigma_N} = \boldsymbol{\mathcal{N}}(\boldsymbol{\varepsilon_N}; \boldsymbol{\theta})$
      Compute the internal energy
      Compute $\boldsymbol{\mathcal{L}}(\boldsymbol{\varepsilon_N}, \boldsymbol{\theta_i})$
      Back propagate the error and compute the gradient
      Update $\boldsymbol{\theta}$ with gradient descent
   end for
end while
```

2.3.3 Physic-Informed Neural Network (PINN)

The neural network presented in Subsection 2.3.2 is trained on the full-field strain values to comply with the energy balance but does not account for the local equilibrium of the continuum. At each load step of the test, only one scalar equation can be written from the energy balance. If the load steps are less than the material parameters, the problem has no solution, while if the load steps exceed the number of variables the system will be overdetermined. Overdetermined systems are almost always inconsistent; therefore, the approximate solution is found through an optimization strategy.

To get a better approximation of the constitutive relation through a neural network, the optimization problem can be reformulated to penalise the solutions violating the physics, i.e., the equilibrium equations. The proposed method uses a PINN trained with a modified loss function that penalises the physics violation;

furthermore, a modified architecture which constrains a positive definite constitutive model is proposed.

The PINN receives as input the strain vector projected on the material direction, whose components feed three different sub-networks respectively predicting the stiffness along the principal directions, C_{11} and C_{22}, the deviator stiffness component, C_{12}, and the shear term of the constitutive matrix, C_{66}. The predicted stiffness constants at the given strain are rearranged internally to the PINN and used to compute the stress state by multiplying the stiffness matrix with the strain vector. The shear-axial coupling terms are set to zero, complying with the mechanical decoupling of the axial and shear mechanism.

A schematic representation of the model is shown in Figure 2.4, where the number of layers and neurons represented are indicative.

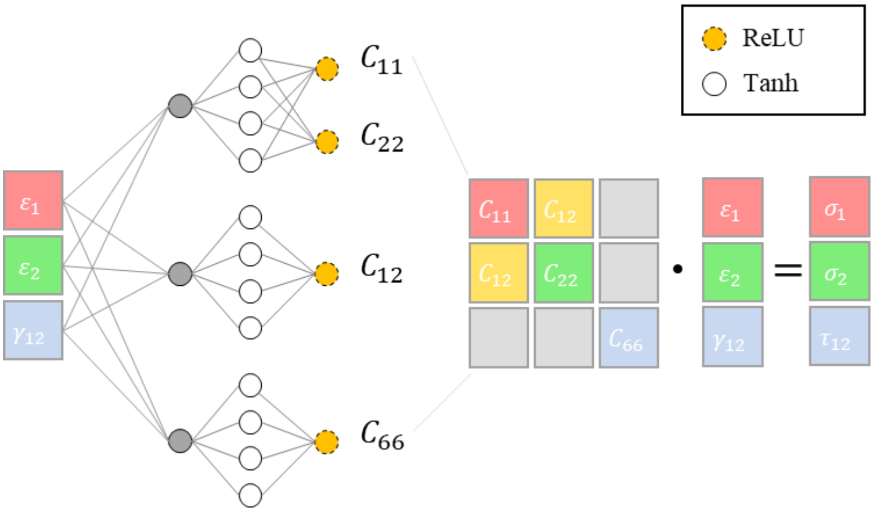

Figure 2.4 Scheme of the core network predicting the stress in the material direction.

The core network is then composed of three sub-networks that can be described with Equations 2.15-17:

$$\begin{bmatrix} C_{11} \\ C_{22} \end{bmatrix} = \mathcal{N}_1(\boldsymbol{\varepsilon}) \,, \tag{2.15}$$

$$C_{12} = \mathcal{N}_2(\boldsymbol{\varepsilon}) \,, \tag{2.16}$$

$$C_{66} = \mathcal{N}_3(\boldsymbol{\varepsilon})\,. \tag{2.17}$$

The PINN sub-networks have hyperbolic tangent (tanh) activation functions on the internal neurons and ReLU activation functions on the output neurons to constrain a positive value of the stiffness constants. The reconstruction of the 3-by-3 stiffness matrix and the tensors product within each batch are computed using the Keras Backend library's functions for the tensorial product.

The PINN, operating on all the elements of the DIC mesh, predicts the full field stress state of the component. The predicted stress is used to compute the loss functions defined with Equation 2.13, modified with two additional terms entangling the physics of the problem. Following the notation introduced in Equation 2.15-17, the internal energy at the element *i* is described in Equation 2.18:

$$2U_i^k = A_i\, t_i\, \boldsymbol{\varepsilon}_i^k : \boldsymbol{\sigma}_i^k, \tag{2.18}$$

where the apex *k* indicates the load step, while A_i and t_i are the element area and thickness, respectively.

The internal energy at the load step k is then computed as the sum of the element's internal energy, $W_{int}^k = \sum_{i\in I_k} W_{int}{}_{,i}^{k}$, from which the loss term on the energy balance is computed with Equation 2.19:

$$\mathcal{L}_{en} = \left|W_{int}^k - W_{ext}^k\right|. \tag{2.19}$$

Recalling Equation 2.9, the predicted stress must comply with the equilibrium equation. The divergence of the stress field is then computed over the defined domain to estimate the equilibrium error associated with the network prediction. The computation of the stress gradient is computationally expensive, therefor n_i co-location points and n_k co-location load steps are defined, at which the divergence error is computed at each iteration with Equation 2.20:

$$\mathcal{L}_{div} = \sum_{k\in K_{col}} \sum_{i\in I_{col}} \left|\nabla \cdot \boldsymbol{\sigma}_i^k\right|, \tag{2.20}$$

with the co-location points and frames defined in I_{col} and K_{col}, respectively.

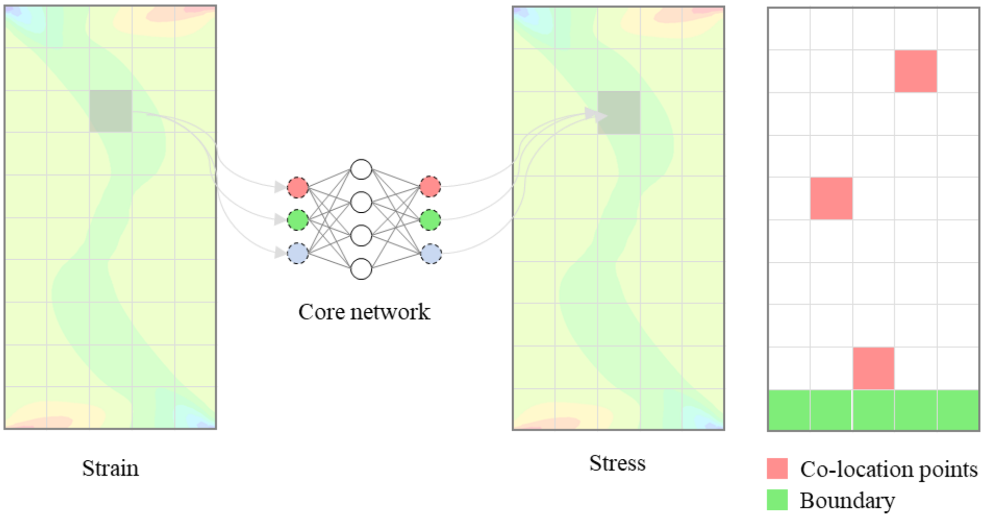

Figure 2.5 Scheme of the full field stress prediction and computation of the loss in the co-location points.

Recalling Equation 2.9, the boundary error is computed at the co-location frames with Equation 2.21:

$$\mathcal{L}_{bc} = \sum_{i \in I_{bc}} \sum_{k \in K_{col}} \left| \boldsymbol{\sigma}_i^k \cdot \boldsymbol{n} - F^k \right|. \tag{2.21}$$

The total loss function is computed as the scaled summation of the three different terms with Equation 2.22:

$$\mathcal{L}_{tot} = \alpha \mathcal{L}_{en} + \beta \mathcal{L}_{bc} + \delta \mathcal{L}_{div}, \tag{2.22}$$

Where the loss terms $\mathcal{L}_{en}$, $\mathcal{L}_{bc}$, and $\mathcal{L}_{div}$ refer to the energy, boundary conditions and divergence error, respectively.

The hyperparameters of the proposed method are resumed in Table 2.2.

$\boldsymbol{n}$	Number of neurons per layer
$\boldsymbol{n_l}$	Number of layers per network
$\boldsymbol{n_i}$	Number of co-location points

$\boldsymbol{n_k}$	Number of co-location frames
$\boldsymbol{\alpha}$	Energy loss scaling factor
$\boldsymbol{\beta}$	Boundary loss scaling factor
$\boldsymbol{\delta}$	Divergence loss scaling factor

Table 2.2 Hyperparameters of the model

The effect of the hyperparameters on the model accuracy and computational time is discussed in Section 2.5.

2.4 Results

The results are presented in two subsections where the network performance trained on artificial and experimental data is discussed, respectively. Since the material laws used in the virtual test simulated with the FEM are known, these are used as a reference to directly compare them with the material response identified with the MDS method. In the following, the material model calibrated from tensile tests on un-notched and notched CFRP specimens are discussed and data-processing techniques are introduced to properly filter the experimental results from noise.

2.4.1 Virtual test of orthotropic materials

2.4.1.1 Orthotropic elasticity

The force-displacement curves resulting from the virtual experiments with a linearly elastic orthotropic material law are presented in Figure 2.6a.

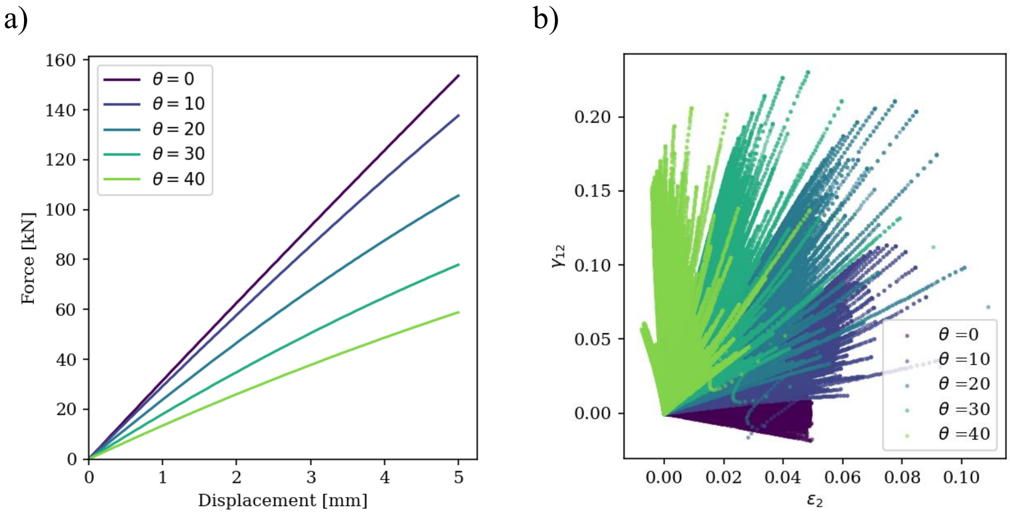

Figure 2.6 Results of the virtual test of linearly orthotropic materials at different orientations with respect to the loading direction: a) force-displacement curves; b) strain states of the material points.

Varying the orientation of the material main direction with respect to the loading axis, the strain states of the material points vary accordingly. In particular, the axial-to-shear strain ratio changes from a purely tensile test at 0° to a pure shear test at 45°, as can be observed in Figure 2.6b, where the strain states of all the elements are reported for all the loading frames. The points obtained from the tensile test at 0° have a principal value on the principal material direction (ε_2), while the states of the off-axis tests progressively shift their main component toward the shear strain (γ_{12})

The material angle affects the strain energy and its shear and axial components. Indeed, by separating the shear and axial terms of the strain energy and analyzing their variation with respect to the angle θ, it can be observed that the two terms are equivalent at an angle θ approximatively equal to 30° (Figure 2.7).

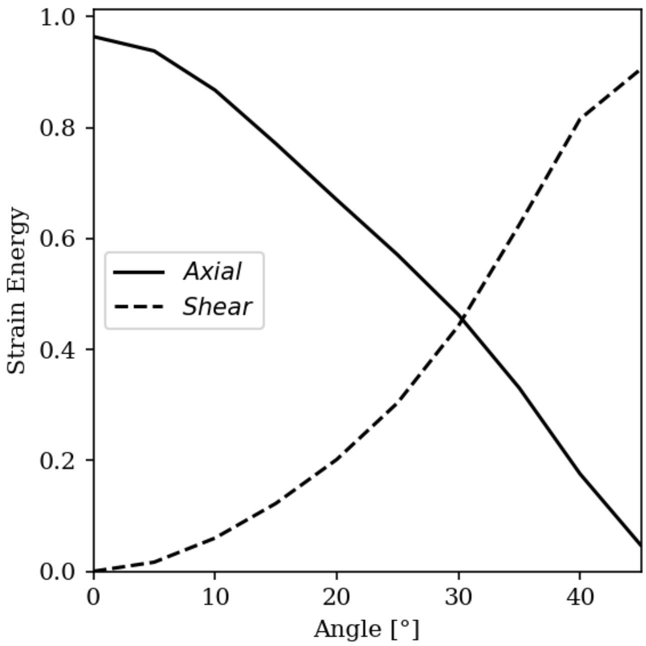

Figure 2.7 Variation of the strain energy content with the material angle

This trend is governed by the material properties, more specifically by the ratio between the axial and shear moduli. Considering a pure tensile test with an applied strain along the y-direction $\bar{\varepsilon_y}$, the transverse deformation is controlled by the in-plane ν_{xy} Poisson's ratio computed with Equation 2.23:

$$\varepsilon_x = -\nu_{xy}\varepsilon_y = -\frac{C'_{12}}{C'_{11}}\varepsilon_y \,, \tag{2.23}$$

being C' the stiffness matrix in the laminate direction, computed from the stiffness matrix in the principal direction C_0 defined with Equation 2.24:

$$C_0 = \frac{1}{1-\nu_{12}^2}\begin{bmatrix} E_1 & \nu_{12}E_1 & 0 \\ \nu_{12}E_1 & E_2 & 0 \\ 0 & 0 & (1-\nu_{12}^2)G_{12} \end{bmatrix}, \tag{2.24}$$

with the rotation matrices R_σ and R_ε:

$$C' = R_\sigma^{-1} C_0 R_\varepsilon \tag{2.25}$$

Using Equation 2.25, the axial and shear components of the strain energy are computed to define the material angle yielding an equivalence of two terms (Figure 2.8).

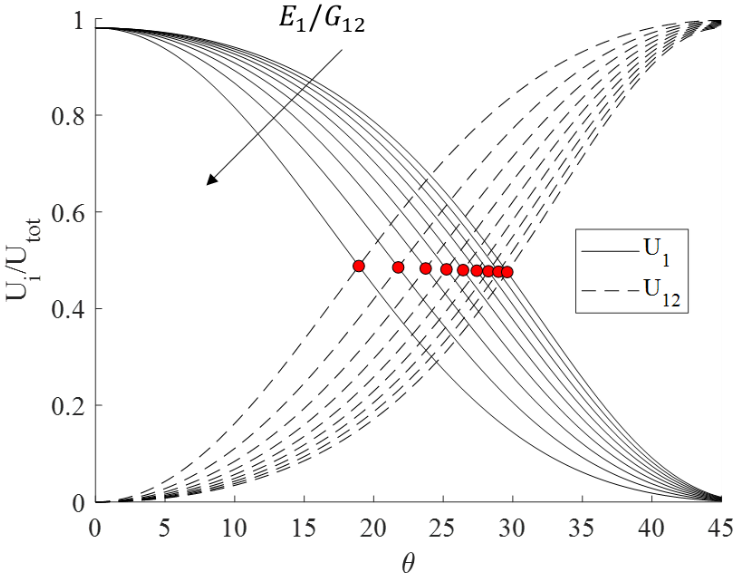

Figure 2.8. The variation of the axial and shear components of the strain energy with material angle θ. The red dots indicate the equivalence point for different E_1/G_{12} ratios.

The angle at which the axial and shear strain energies are equivalent is determined by E_1/G_{12}: the higher it is larger the angle needed to meet the state of equivalent energies.

Table 2.3. The hyperparameters of the model

$\boldsymbol{n}$	$\boldsymbol{n_l}$	$\boldsymbol{n_i}$	$\boldsymbol{n_k}$	$\boldsymbol{\alpha}$	$\boldsymbol{\beta}$	$\boldsymbol{\delta}$
15	3	10	10	0.3	0.7	1000

The model has been separately trained three times for each angle, with the main hyperparameters reported in Table 2.3. The scale factors α and β have been selected to sum up to one, while a divergence factor of 1000 has been selected to get a similar order of magnitude of the three terms in order to comply with all the governing equations described with each loss term. The activation function is a SELU for the hidden layers and a linear function for the output layers. The learning rate has been set to 10^{-5} to avoid exploding gradients phenomena and the models have been trained for 500 epochs with an early stopping algorithm that interrupts the process when a decrease of the loss function lower than 10^{-2} is observed for more than 10 consecutive epochs. The final weights are restored from the epoch where the lowest value of the loss function has been observed.

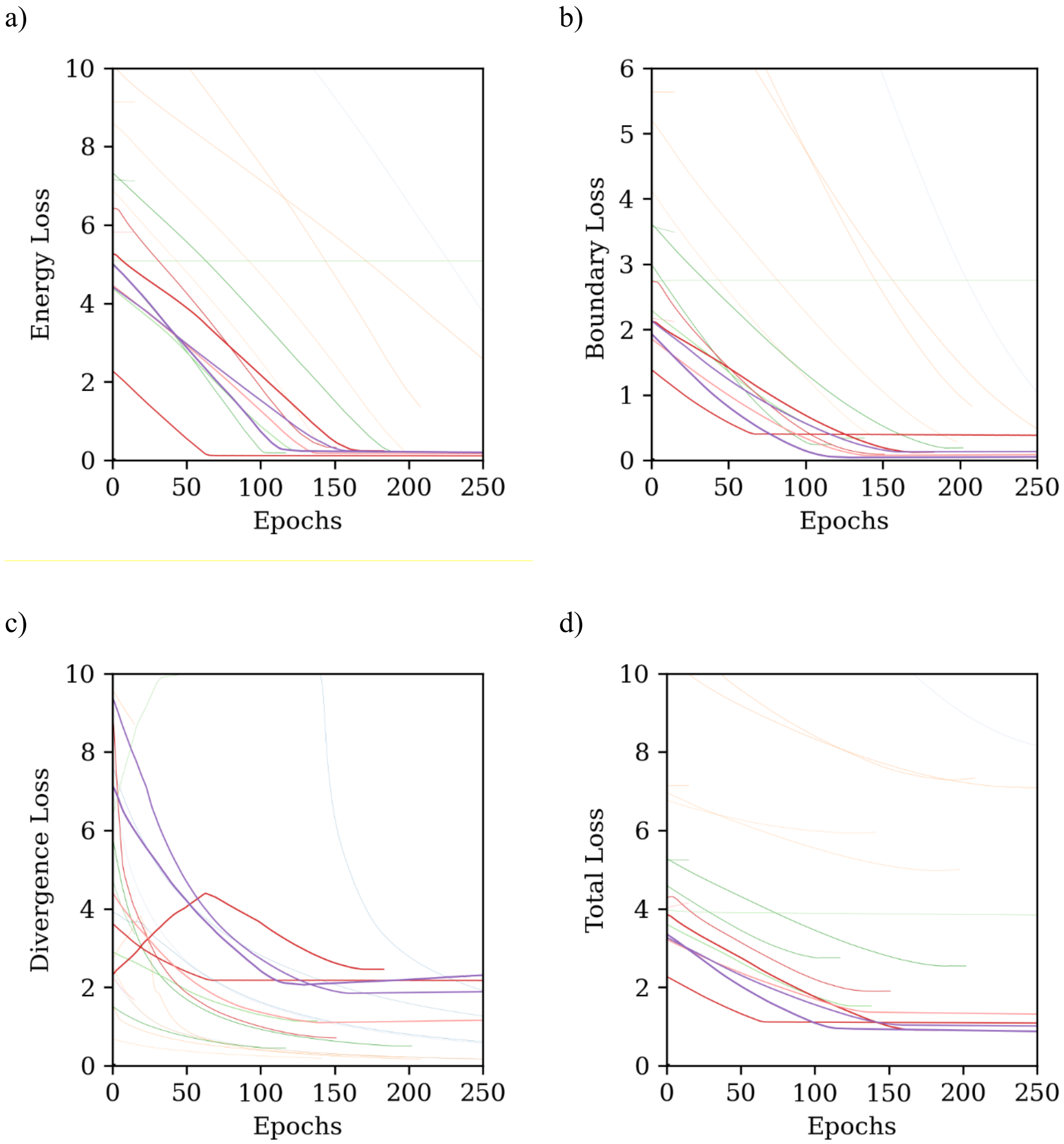

Figure 2.9. The loss function during the training process: a) Energy, b) Boundary, c) Divergence, d) Total. The curves refer to all 24 models trained on artificial data (3 repetitions for each angle).

The value of the total loss function during the training epochs for all the different material angles is reported in Figure 2.9d, with the different terms reported in Figure 2.9a-c.

The three terms of the loss function (i.e., energy, boundary, and divergence) and its total value monotonously decrease with the training iterations. The boundary and energy terms eventually converge to small values, while the divergence loss reaches a higher minimum that could be affected by the vanishing of the equilibrium in the last frames due to specimen failure. Results show sporadic cases where an exploding gradient phenomenon can be observed, yielding a divergence of the loss function. To overcome this potential issue, it is recommended to train the network multiple times (at least three) and inspect the training loss to discard the invalid results. Alternatively, the learning rate could be further reduced below 10^{-5}, stopping the gradient-based algorithm from diverging far from the domain of the function minimum. It should be noted that lower values of the learning rates reflect longer training times. Nevertheless, the accuracy of the model is also affected by the weights initialization that is randomly defined at the beginning of each training using the Glorot [69] initializer with a random distribution. To discern the results from the influence of the initial parameters, each model is trained three times and the best learning curve is presented in the following.

The loss values for the different virtual tests with varying θ are reported in Figure 2.10, where it can be observed that the model performs better when trained on off-axis laminates with an angle greater than 20°. The boundary and energy terms of the loss (Figure 2.10a) follow a similar trend that is governed by the strain energy composition: at a lower angle, the strain energy component associated with the shear is significantly lower than the axial components, making it challenging for the network to converge towards an exact solution of the elastic constants. Comparing the predicted constants G_{12} and E_1 with the exact values used in the FEM model, it can be observed that the predicted shear modulus is incorrect at lower angles, while values closer to the reference solution are predicted when the shear strain energy approaches the axial strain energy (Figure 2.10b).

a) b)

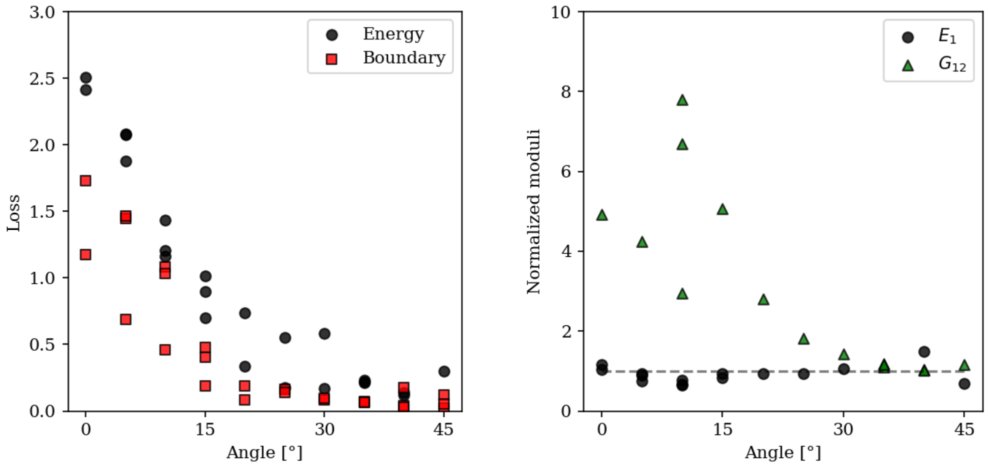

Figure 2.10. a) The values of the loss function terms related to the boundary and energy terms; b) The predicted moduli normalized over the exact values used in the FEM model.

In other words, testing a material along its principal direction will induce a strain energy that is almost completely dependent on the material properties in that direction, making it consequently impracticable to determine the properties along the second direction. However, the right testing configuration which equally balances the strain energy contributions would allow for the simultaneous determination of the material properties along different directions [70].

Finally, the stiffness matrix computed with the PINN on a 30° specimen is compared with the reference values and the stress-strain curves are reported in Figure 2.11. Obtained results look very accurate.

$$\bar{C} = \begin{bmatrix} 64.98 & 9.07 & 0 \\ 9.07 & 64.98 & 0 \\ 0 & 0 & 2.5 \end{bmatrix}, \qquad C_{pred} = \begin{bmatrix} 63.8 & 9.4 & 0 \\ 9.4 & 62.8 & 0 \\ 0 & 0 & 2.45 \end{bmatrix},$$

a)

b)

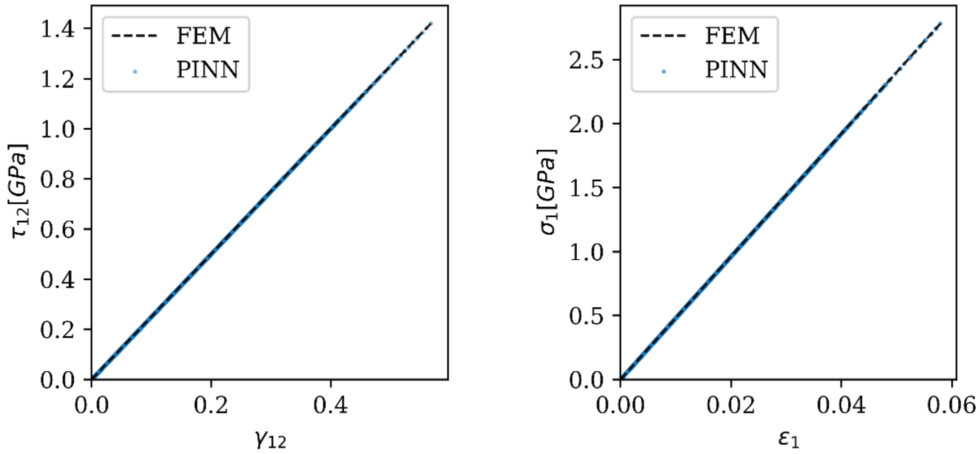

Figure 2.11 The shear (a) and axial (b) elastic response characterized by the PINN is compared with the reference elastic response.

2.4.1.2 Orthotropic elasticity with shear damage

The main advantage introduced by the implementation of the NN is its ability to replicate any function without predefining any parametric model. Therefore, the PINN performance is investigated for two different nonlinear constitutive relations in the following.

A linear elastic material with shear damage has been virtually tested using the material models described in section 2.2.1. The elastic properties are described in Table 2.1, while the damage parameters are reported in Table 2.4.

Table 2.4. Parameters of the damage model for the Linear Damage (LD) and Cubic Damage (CD) cases.

Parameters	γ_0	γ_f	β
LD	0.1	0.7	1
CD	0.0	0.4	1/3

To validate the accuracy of the method and its generality, two different materials have been tested with linear damage (LD) and cubic damage (CD) behaviour. The predicted model is compared with the LD one in Figure 2.12a, where it can be observed that the response characterized by the PINN accurately replicates the material model defined in the FEM. It can be observed that the damage initiation mechanics (that produce the deviation of the curve from the linearity) are accurately captured by the neural network, as the damage propagation and its linear trend. As previously observed in the elastic response case, the linear response is also captured by the PINN with a maximum error of 5%.

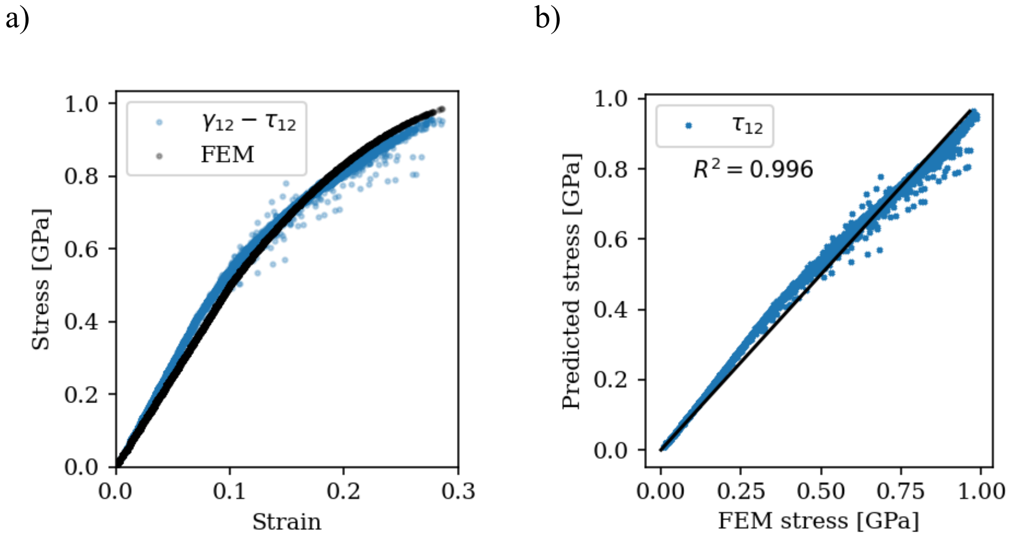

Figure 2.12. a) The stress vs strain curve of the LD model characterized with the MDS method compared with the FEM material model; b) the accuracy plot comparing the prediction with the values of the material model.

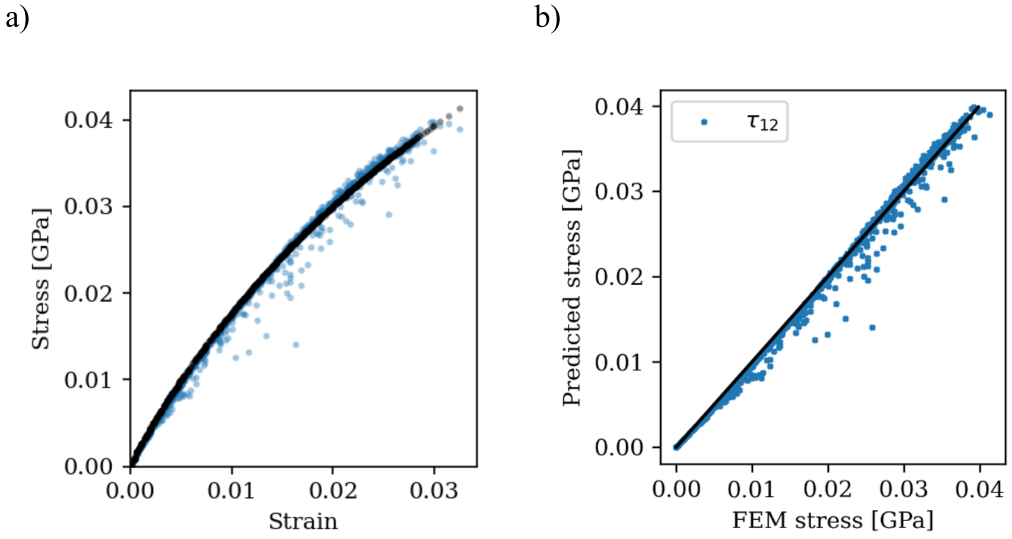

Figure 2.13. a) The stress vs strain curve of the CD model characterized by the MDS method compared with the FEM material model; b) the accuracy plot comparing the prediction with the values of the material model.

The predicted stress is in good agreement with the values computed with the FEM, showing a coefficient of determination of 0.996 (see Figure 2.12b). The accuracy of the PINN results for a cubic damage law is shown in Figure 2.13, where the good accuracy of the model is confirmed by the coefficient of determination equal to 0.998 between the predicted stress and the one computed with the FEM. The CD law gives slightly better results than the LD law.

The predicted strain energy and boundary forces are reported in Figure 2.14 and compared with the target value used for the computation of the loss function. In Figure 2.14b, the boundary force values are compared with the values of the load applied to the specimen and the co-location frames are indicated with red markers.

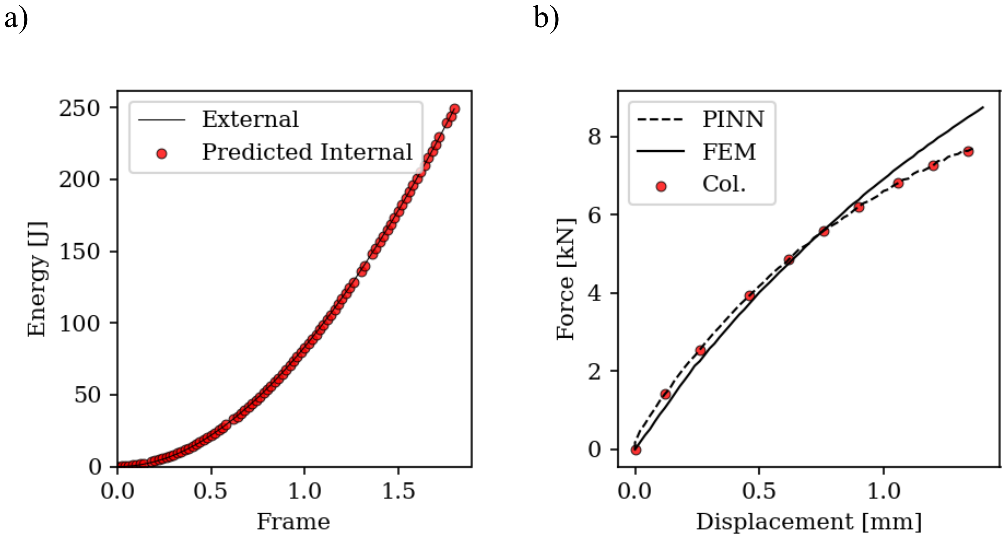

Figure 2.14. a) The internal energy computed with the predicted stress compared with the external energy used to train the PINN; b) the boundary force compared with the stress normal at the traction boundary.

The predicted internal energy is in good agreement with the external energy at every frame of the test. The boundary force computed from the normal stresses does not perfectly match the external load, with an average error of 8% and a maximum error of 12.5% in the last frame that is considered acceptable given the fact that the boundary terms is only one of the three loss terms governing the training of the model. Given that the predicted boundary force follows a continuous trend in between the co-location, it can be concluded that there is no need to increase the number of points, which would reflect in higher computational cost.

2.4.2 Experimental tensile test of CFRP

2.4.2.1 Data filtering and reduction

The strain data are stored in three third-order tensors $\mathbf{E_x}$, $\mathbf{E_y}$, $\mathbf{E_{xy}}$, where $E_{\alpha,ijk}$ is the component α of the strain in the element with position (X_{ij}, Y_{ij}) at the kth load step. The dimension of each tensor is defined by the number of subsets along the *x* and *y* directions (n_x and n_y) and the number of load steps *N*.

Since neural network performance can be negatively affected by noisy data, it is fundamental to pre-process the experimental measurements to cut out the noise both in space and time dimensions. The experiments presented here have been conducted under a quasi-static regime, therefore a gradual and smooth variation of the strain over time is expected. To cut out the noisy oscillations, a moving average filter is used along the third dimension of the E tensor, as described in Eq.2.26:

$$\bar{E}_{ijk} = \frac{1}{N}\sum_{k-\frac{N}{2}}^{k+\frac{N}{2}} E_{ijk} \tag{2.26}$$

Similarly, the force and displacement vectors, **F** and **d**, containing the values of applied displacement d_k and measured force F_k at load step *k*, are filtered with the same window size.

Each snapshot E_{ij} representing the element strain at a given load step can be decomposed into signal and noise:

$$E_{ij} = \bar{E}_{ij} + N_{ij} \tag{2.27}$$

Moreover, given the heterogeneous nature of the composite material, the strain can be further decomposed as an average strain μ_{ij} and a fluctuation term σ_{ij}:

$$\bar{E}_{ij} = \bar{\mu}_{ij} + \sigma_{ij} \tag{2.28}$$

The data-driven method presented in this work wants to establish a homogenized constitutive relationship in the stress-strain space and requires filtering out the oscillations in the space domain. Combining Eq.2.27 and Eq.2.28, the strain tensors can be decomposed

$$E_{ij} = \bar{E}_{ij} + \sigma_{ij} + N_{ij} = \bar{E}_{ij} + \Sigma_{ij} \tag{2.29}$$

A convolution filter is applied in the space domain to cut off the noise and the strain perturbation induced by the material heterogeneity.

$$\bar{E}_{ij} = E_{ij} * \mathcal{A} \tag{2.30}$$

Being $\mathcal{A}$ the filter matrix with shape m by m, containing all *1/m* values. The filter is applied with symmetric padding, meaning that the $(m-1)/2$ rows and columns are added with values symmetrically equal in the filter window.

a)

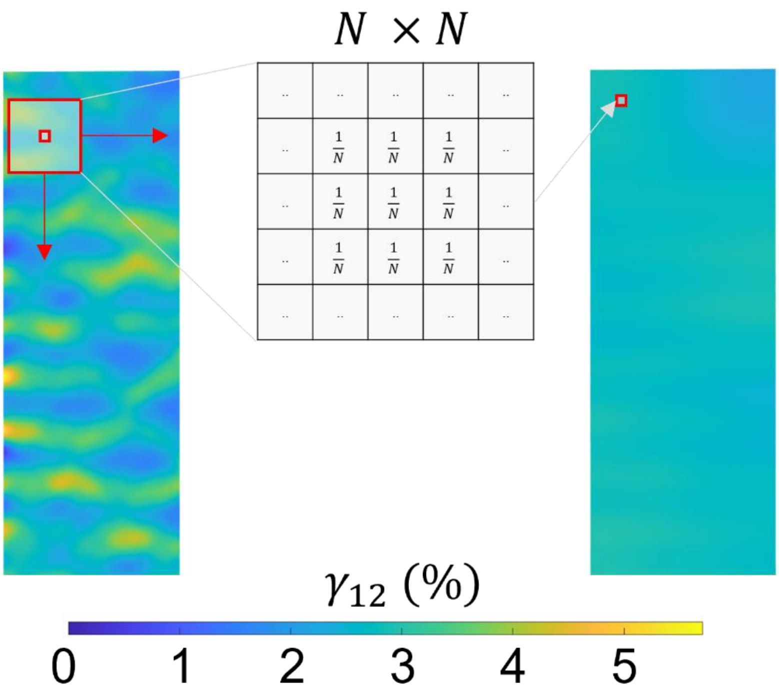

b)

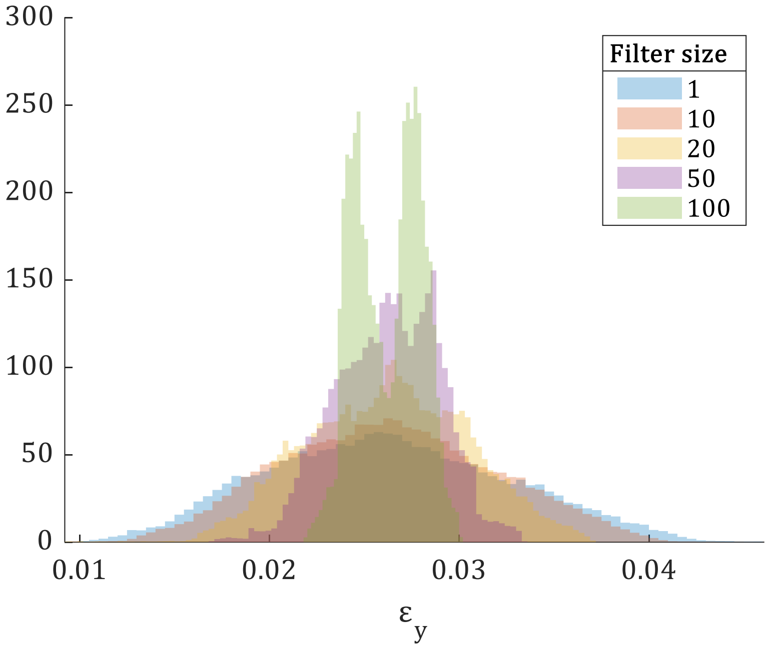

Figure 2.15 a) The convolution filter applied to the experimental strain measured with the DIC on the left and the resultant homogenized field on the right; b) The histograms of the strain values of the filtered fields with different window sizes.

Under the assumption of a zero-mean normally distributed noise, it is assumed that, if a filter window is selected large enough to cover an area of the strain that is representative of the homogenised material, the result of the convolution is the homogenised strain.

The filtered strain tensors have a size $n_x \times n_y \times N$ (same as the original tensors), which may result in excessively dense data that could compromise the efficiency of the method. To reduce the number of states in the stress-strain space, the data are clustered with a k-means clustering algorithm (Appendix) into n_c clusters.

The clustering operates in a three-dimensional space $(\varepsilon_x, \varepsilon_y, \gamma_{xy})$, assigning the $n_x \cdot n_y \cdot N$ strain states to n_c clusters each with a centroid $\left(\varepsilon_{x,C}, \varepsilon_{y,C}, \gamma_{xy,C}\right)_i$. Successively, the strain states belonging to the i^{th} cluster are substituted with their centroid value. Figure 2.16 depicts the initial strain states in the $\varepsilon_y - \gamma_{xy}$ domain, where each point represents a state before the clustering and its colour refers to the cluster it has been assigned to.

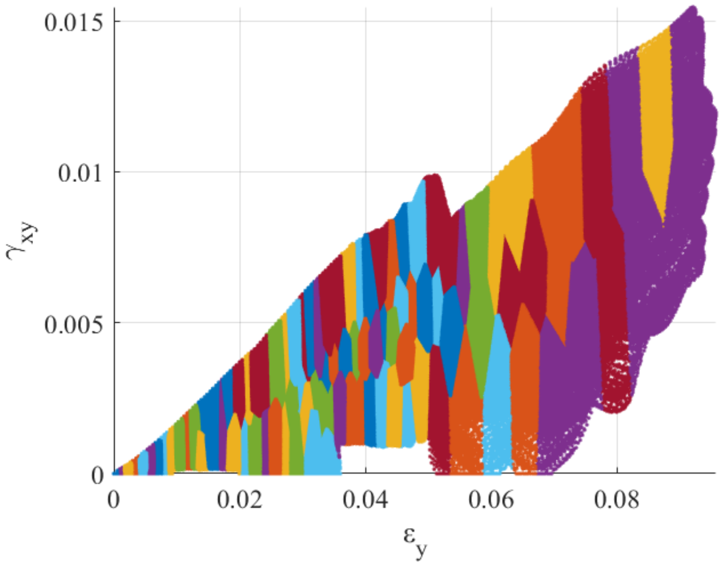

Figure 2.16. Strain states clustered into 100 clusters with a k-means algorithm.

The clustered data $\bar{E}'$ contains n_c unique strain states, that will be used to train the network to learn the constitutive relation. The effect of the clustering on the strain maps is shown in Figure 2.17, where it can be observed that the clustering smooths the strain maps preserving a good resolution in the high-load frames where the strain gradient is higher while reducing the accuracy in the low-load frames where the strains appear to be more homogeneous over the domain. In the last frame, corresponding to the specimen failure, it can be observed that the clustering does not affect the concentration of the damage because the transformation is done in the strain domain and not in the space domain. The clustering procedure took about 70 seconds to cluster 6528000 points into 200 clusters, and 60, 40, 25 and 13 seconds for the clustering with 150, 100, 50 and 25 clusters, respectively. For the case under study, the clustering does not affect the accuracy of the results.

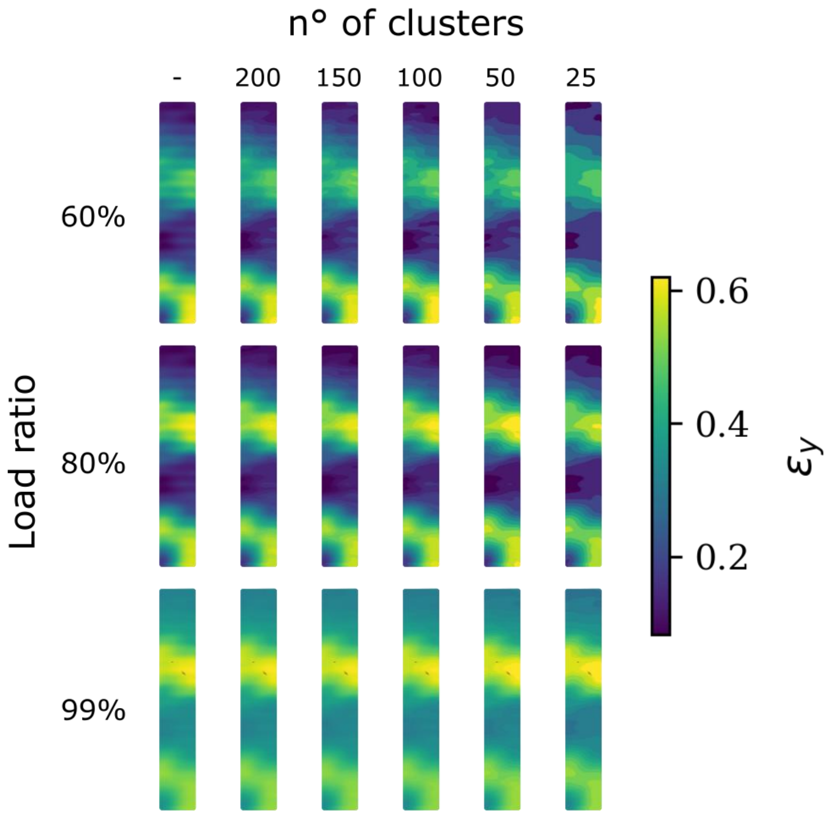

Figure 2.17. The effect of the clustering on the DIC strain maps of a 45° off-axis carbon fibre reinforced specimen.

After having filtered the strain data in the space and strain domains, the support grid of the strain data has been coarsened to reduce the dimensionality of the dataset. To reduce the grid of a factor λ, each sub-domain of dimensionality [λ, λ] is averaged and assigned to a point of the new grid with a dimension reduced of λ (as shown in Figure 2.18. The clustering technique is applied to the measured strains in the laminate direction and successively rotated in the material coordinate system.

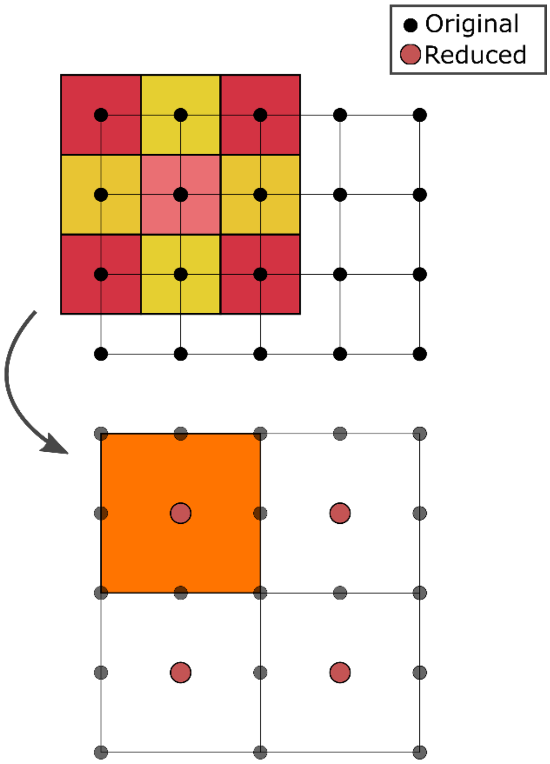

Figure 2.18. An example of a data reduction with a reduction factor λ equal to 3.

2.4.2.2 Results: material models and damage law

The method has been applied to the unnotched specimen with an off-axis angle of 45°. The strain data have been filtered with the procedure described above, using a size of the convolutional filter of 100x100 pixels and 100 clusters. The adopted PINN has 3 hidden layers with 15 neurons each, with a SELU activation function for all the hidden neurons. The weights have been initialized with the Glorot procedure and the model has been trained for a maximum of 200 epochs with a learning rate of 5e-5, with the loss weight β, δ and α equal to 0.5, 0.5 and 100, respectively. The values of α and β have a limited influence on the results, as discussed in the following. The data have been sampled at 54 load steps, of which 49 have been used as training data and 5 have been left as validation, while only 10 evenly spaced co-location frames have been used for the evaluation of the boundary and divergence loss during the training. The displacement fields are described over a support grid of dimension 68-by-10, yielding an element area of 3.86mm^2. The training and validation losses are reported in Figure 2.19, showing a monotonous decrease of the error with a solution converging towards a total loss of 10.6 and 9.3 for the training and the validation data, respectively.

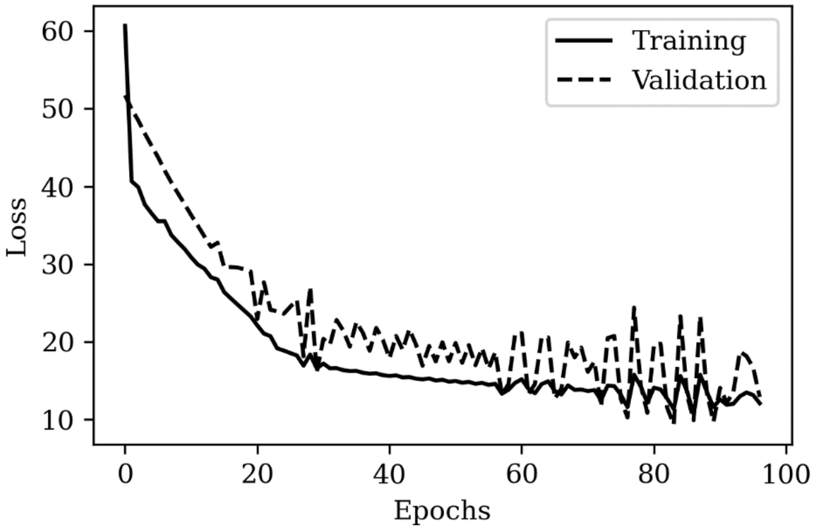

Figure 2.19. The total loss during the training epochs was computed over the validation and training frames.

A physical interpretation of the loss is given in Figure 2.20a, where the internal energy computed from the predicted stress is compared with the external energy. The mean relative error on the balance energy is 5%, with a maximum error at low displacements where the clustering algorithm tended to cluster the low-strain material points together and smoothed the variation in the initial elastic steps.

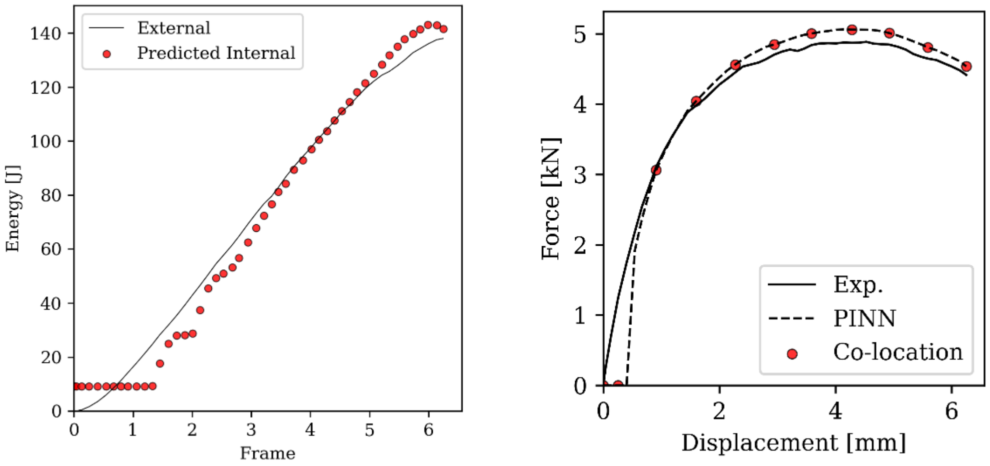

Figure 2.20. a) The energetic balance of the internal energy related to the predicted stress with the external energy; b) the traction force compared to the normal stress at the boundary.

The extracted stress-strain curve is presented in Figure 2.21a where the band of curves represents the results interval containing all the material curves obtained by three runs of the PINN.

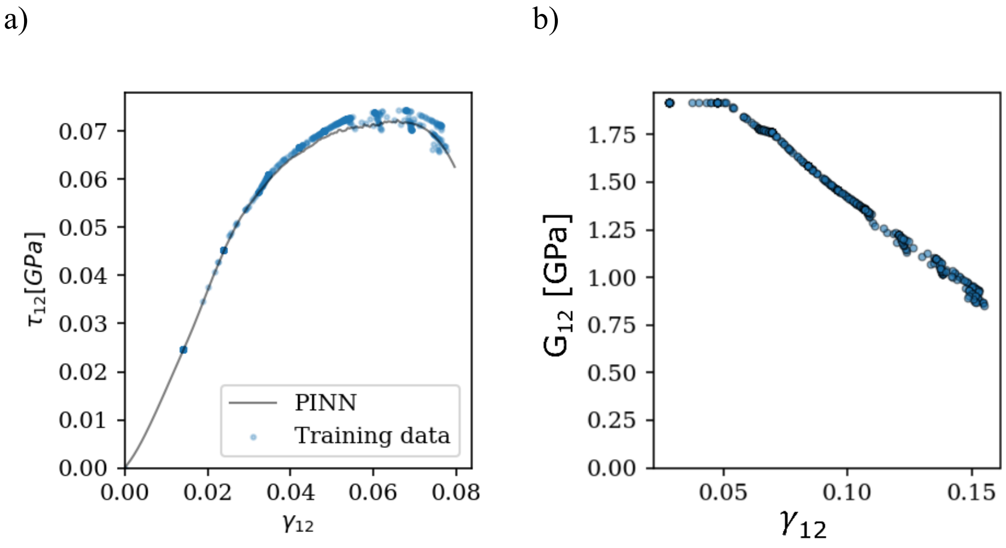

Figure 2.21. a) The stress-strain curve obtained with the PINN and b) the corresponding damage law.

In Figure 2.21a the stress states predicted by PINN on the training frames are represented with blue dots, while the grey line shows the material model computed in the range between 0 and 0.08 mm/mm of shear strain. Figure 2.21b shows the shear stiffness computed at each stage of the training frames. The damage index of Equation 2.1 can be computed from the predicted stiffness with the equation $d = 1 - G/G_0$, being the initial stiffness G_0 equal to the stiffness in the elastic region. The damage can be thus calculated at each material point from the strain state using the PINN, and the damage propagation and localization can be observed in Figure 2.22b. It is worth stressing the concept that the damage in the specimen corresponds to a decrease in the material properties, whose variation has been learned from the full field strains by complying with the governing equations of solid mechanics. In the nominally uniform material, the model can learn the material model at different strain levels from the non-uniform strain maps acquired with the DIC.

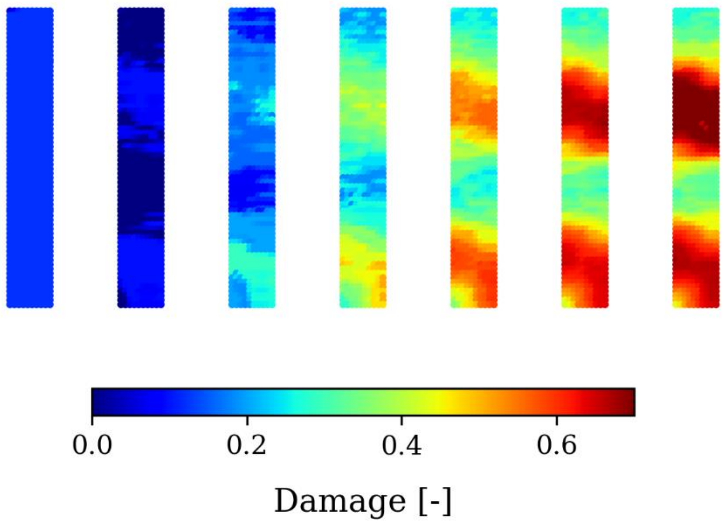

Figure 2.22. Damage propagation in the specimen computed with the PINN at different stages of the test, at 7 equally spaced frames from the beginning of the test until the failure.

The influence of the loss weights over the predicted curve has been investigated by varying the α from 0.25 to 0.75 while keeping $\beta = 1 - \alpha$. The results reported in Figure 2.23 show that the model computed with the PINN is not sensitive to the weights of the loss function in the explored range.

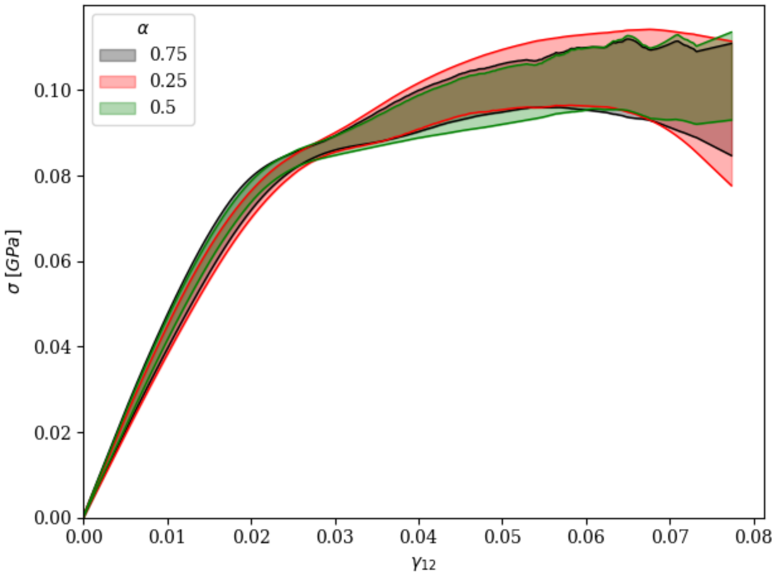

Figure 2.23. Predicted material response with different values of the energy loss weight (α).

2.5 Discussion

The accuracy and efficiency of the proposed methodology are affected by the hyperparameters of the model described in Table 2.2.

2.5.1.1 Accuracy

A sensitivity analysis of the hyperparameters of the architecture on a test case revealed that an increasing number of neurons has a stronger influence on the accuracy than the depth of the network. A number of neurons per layer equal to 15 appears to be the optimum choice to maximize the accuracy of the network. Architectures with more than 3 hidden layers perform better for almost any width of the layers, as shown in Figure 2.24.

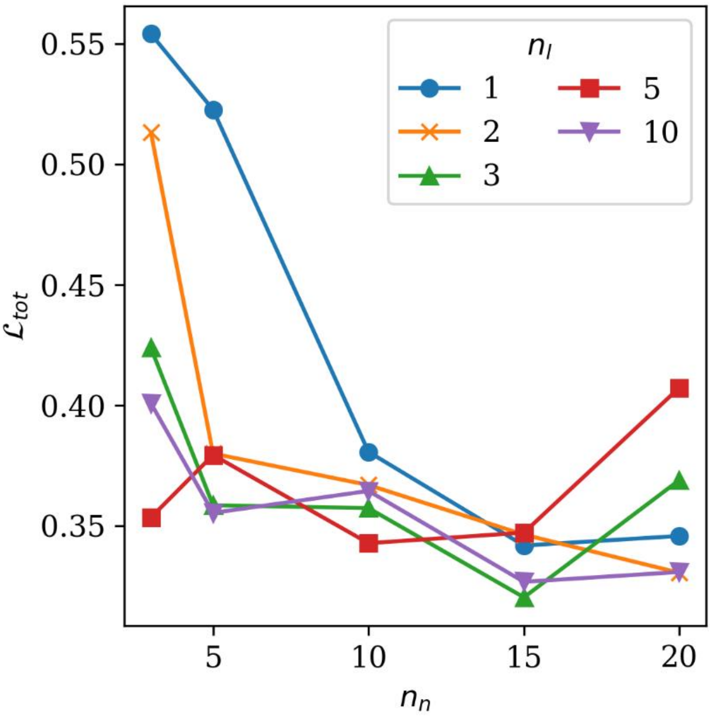

Figure 2.24. Accuracy of the PINN on a test case with varying width and depth of the architecture.

Therefore, a minimum of 3 hidden layers has always been used in this work, with a width of 15 neurons.

2.5.1.2 Computational cost

The material identification algorithm here proposed is meant to be executed only at the characterization stage and it can output the material model in the form of a trained neural network with a single execution. For this reason, the computational cost of the model training is not a critical aspect, but it is discussed for the sake of completeness.

The computational cost of the model training can be divided into the following terms: forward prediction, loss computation, and back-propagation. The forward and back-propagation are affected by the network complexity, thus relatable to the number of trainable parameters defined with Equation 2.31:

$$n_p = 13n_n + 3(n_l - 1) * n_n^2 + 3n_n n_l \tag{2.31}$$

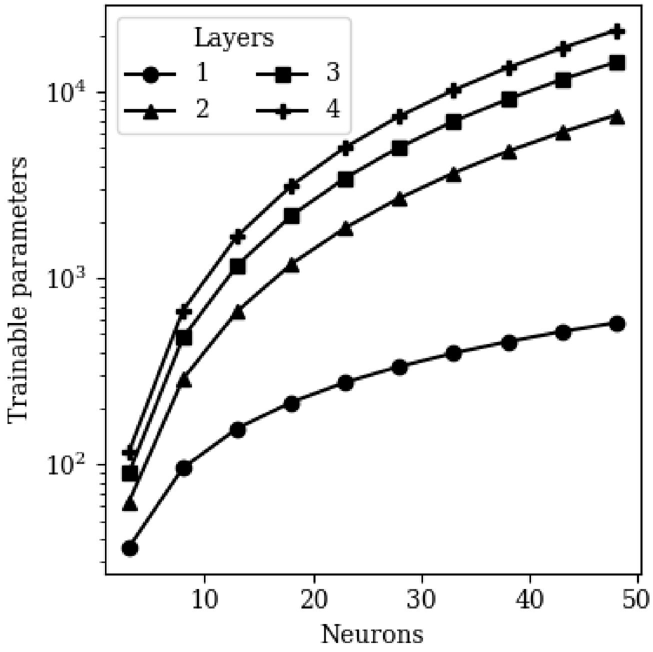

Figure 2.25. The variation of the number of trainable parameters with the number of neurons per layer.

The back-propagation algorithm complexity linearly scales with the number of connections, following the trend represented in Figure 2.25.

The loss computation is instead affected by the computation of the three distinct terms accounting for the energy, divergence, and boundary force error. These are independent of the network complexity, and they are only relatable to the number of material points in each frame (i.e., batch dimension), the number of co-location frames, and the number of co-location points.

Following the above analysis, an architecture with 3 hidden layers with 15 neurons each has been identified as an acceptable trade-off between the computational time and the model accuracy.

2.5.1.3 Extrapolation

The proposed methodology efficiently learns a stress-strain relation from the full-field displacements measured on the surface of the specimen. The trained PINN acts as a material model that maps the strain state into the stress space for any given input. However, the model is only trained with the strain states observed in the experiments and its accuracy outside the training domain could be critically compromised. Figure 2.26 shows that the prediction of the material response in the compression domain deviates from the prescribed model due to the paucity of data.

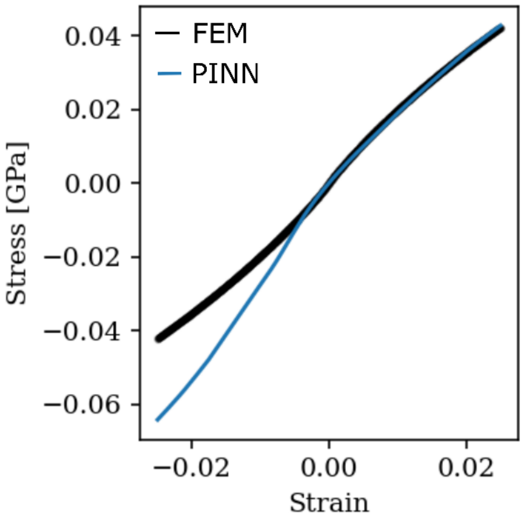

Figure 2.26. Prediction of the compressive response of the PINN trained on the CD tensile test (blue) compared with the material model (black).

This suggests that the PINN should be trained with data that explores the domain that is intended to be analysed.

2.6 Conclusions

In this Chapter, an MDS method that learns the constitutive equations of materials from the displacement field and the boundary force has been introduced. The method combines the fundamental concepts of PINN with MDS architectures to characterize the mechanical response of materials leveraging on the local data about the surface displacement obtained with the DIC and preserving the governing equation of continuum mechanics, such as the forces equilibrium and the energy balance. First, the formulations of the method have been introduced to provide a theoretical background and a mathematical description of the algorithm, and then the algorithm itself and its implementation have been presented. The proposed method, implemented in a Python environment, using Google's TensorFlow libraries, has been tested against virtual experiments simulated with the FEA software LsDyna, replicating a tensile test of a fibre-reinforced specimen with a varying off-axis angle. The linear elastic orthotropic model used in the FEM has been compared with the constitutive equation learned with the proposed method from the different virtual tests at varying angles. The results showed that an orthotropic constitutive equation could be accurately characterized with a single test if the axial and shear components of the strain energy are sufficiently similar, yielding the convergence of the model toward a solution with an average error below 10% under the most favourable conditions. It has been observed that such a balance of the energy terms can be achieved with a 30° off-axis specimen, where the elastic terms are equivalent. Damage models with a linear and cubic trend of the shear damage variable have been modelled in the FE environment to assess the performance of the method against nonlinear material response and the results showed an overall good accuracy of the PINN with a 5% maximum error and a correlation coefficient above 0.99 between the predicted and the prescribed stress.

The methodology offers a powerful tool to automate the calibration of material models that usually follows an iterative process where two main steps are repeated until convergence: the selection of the parametric expression of the material model and the following calibration of the model parameters. This procedure, usually conducted with a FEM model replicating the experimental set-up, is extremely time-consuming, due to the tremendous number of models available to the users and the computational burden of the FE models. The presented PINN can directly learn the stress-strain relation from the experimental test, satisfying the equilibrium and conservation equations commonly imposed in FEM, overcoming the shortcoming of the model identification, and directly establishing a stress-strain relation that can be used in a FE Solver. In this regard, future developments will be done to implement the NN in the FE solver to fully exploit the potentiality of the method. Behind that, the method makes the best out of the full-field experimental techniques by inferring the material response of the tested specimen from all the available data, enabling the concurrent identification of the orthotropic material response under different directions with a reduced number of tests, as demonstrated on the virtual test in section 2.4.1.

However, the material models learned with the PINN are intrinsically limited by the observed strain states. The extrapolation of the material response outside the training domain could lead to inaccurate results compromising the usage of such models. The presented method can indeed learn from the observed states and establish a stress-strain relationship that holds in the proximity of the training dataset, which is defined by the available experiments. The extrapolation capability of the model could be enhanced by properly designing the experiments to cover a wide range of the strain domains, or at least the region where the material is expected to work in the final application. The reliability of the method could be intrinsically modelled by adopting the Bayesian formulation of the NN that uses stochastic weights described by probability distributions. These models could learn the epistemic and aleatoric uncertainty of the material model calibrating the probabilistic formulation of the weights. Future developments will focus on the implementation of such methods in the PINN to estimate the reliability of the model and guide the user toward an uncertainty-driven increase of the available data.

3 Data driven statistical method for multiscale characterization and modelling of as-built fibre-reinforced composites

3.1 Introduction

In Chapter 2, an MDS characterization methodology has been introduced to learn the constitutive equations from the full field displacements and the applied boundary conditions of standard experiments. It has been shown that by using PINNs combined with the governing laws of solid mechanics, the material response can be accurately characterized without introducing any parametric formulation. Although the method has shown remarkable precision, it is intrinsically limited by the available experimental data; the extrapolation outside the observed strain domain may indeed result in inaccurate predictions due to the absence of any phenomenological knowledge used to extrapolate the material response outside that domain. In principle, specifically designed experiments can be performed to learn the material response over a larger domain. However, certain strain configurations are typically left unexplored by experiments due to the high complexity of the experimental setup needed to induce them. For example, the bi-axial strain state requires a testing machine with two independent actuators, which is rarely available in the material testing labs. When modelling orthotropic materials, especially fibre-reinforced composite, this paucity of data can lead to inaccurate prediction since combined strain states can activate different damage and failure modes that can be hardly predicted if not experimentally observed and properly characterized.

In recent years multiscale models have opened the door to virtual experiments: modelling the material microstructure at its lower scale, at which the damage mechanism initiates and propagates (e.g., individually modelling the matrix and fibres of the fibre-reinforced polymer (FRP) composite) the material response can be predicted for any given strain configuration [71–77]. Following, an overview of the multiscale models developed in the last decades is given and the proposed data-driven approach is introduced.

3.1.1 Multiscale modelling

Multiscale models compute the local response of composite introducing a Representative Volume Element (RVE)[78], a lower scale inhomogeneous representation of the composite material, whose response is homogenized and transferred to the higher scale model. RVEs are defined as the smallest volume over which a measurement can be made that yields a value representative of the whole.

Besides virtual experiments, multiscale models allow modelling of the FRP microstructure at its lower scale where the presence of defects may occur and their effect on the material response can be predicted. For this reason, multiscale modelling coupled with microstructure reconstructions of as-built material can enhance the predictive capability in the presence of defects such as voids, fibre misalignment, or undesired inclusions.

Multiscale modelling techniques have been developed in recent years implementing different approaches, among them two mains can be identified:

- Hierarchical: the RVE analysis and the subsequent homogenization are carried out at specific sampled strain states at which the homogenized stress response is computed. Then, a material law is extrapolated using parametric formulations. Once the material response has been identified, it is passed to a part-scale model in the form of constitutive equations.
- Concurrent: the RVE analysis is computed concurrently with the part scale analysis. The strain state at any material point of the part scale model is applied to the RVE (i.e., localization) and the homogenised response is computed and propagated back to the higher scale (i.e., homogenisation).

The first approach has the advantage of being compatible with any FE solver being the solution scheme is not altered since the RVE is only used beforehand to calibrate a material model. On the other hand, this approach requires a material model to be selected, whose parameters are calibrated with the RVE results, while the concurrent strategy gets rid of any assumption on the homogenized response and directly relies on the lower-scale representation of the material. The latter implies a tremendous increase in computational time that is, at present, unsustainable for most industrial applications.

The most common methods to compute the mechanical response of the RVE are the Finite Element Method and the Fast Fourier Transform method. While the first is well established in the engineering community, the latter has been mainly introduced to deal with signal frequency analysis and decomposition, but in the presently studied application is used to solve the RVE problem where periodic boundary conditions are applied. A summary of the FFT theory and its application to the computation of the homogenized response of RVEs is given in Annex A.

Conventional multiscale approaches usually assume a deterministic description of the micromechanical properties (e.g., microstructure, matrix properties, fibre properties), but there is an inevitable need to establish multiscale statistical microstructure-constitutive property relations in materials design. Researchers have proposed effective methods to account for the stochastic nature of the composite microstructure, by defining statistical descriptors of random microstructures [79–81] that could be experimentally characterized with microstructural images or CT reconstructions [82–86]. In [86] the concept of Stochastic Volume Element (SVE) is introduced, a statistically equivalent volume element that accounts for the randomness of material microstructure on the composite constitutive properties. Published papers [87–89] proposed a statistical multiscale method to propagate the microstructural uncertainty to the structural level by introducing a statistical representation of the RVE. Recently, [90] proposed a probabilistic micromechanical-based approach to account for the effect of scattering sources in composite materials, focusing on voids, material inhomogeneity, fibre morphology, and other manufacturing-induced defects. The above-mentioned works confirm an increasing interest of the scientific community toward a probabilistic prediction of the material response that can account for manufacturing-induced variation and intrinsic material randomness.

The mentioned studies assume that the scatter in the mechanical response of composite materials is only imputable to the microstructure variation. However, [91–93] provided evidence that the in-situ elastic modulus of the epoxy matrix within the composite spatially varies within the material, contributing to the scatter of the homogenized response. The microscale mechanism governing the variation of the elastic response of thermoset polymers has been experimentally investigated with atomic force microscopy (AFM) analysis [94] which revealed a 30% variation of the modulus with the curing state of the polymer. Furthermore, to the author’s best knowledge, only a few studies in the literature describe an experimental procedure to determine the optimal size of the RVE [95,96] and its statistical description from mechanical tests.

The scope of this chapter is:

- To extend the current methodologies by introducing a statistical representation of the in-situ matrix properties in the representative volume at the mesoscale level.
- To introduce a novel approach to calibrate the SVE size (extending the study in [95]) from Digital Image Correlation data of tensile tests.
- To present a novel procedure to calibrate stochastic properties of the extended SVE with experimental results from the tensile test and micro-CT reconstruction.

The developed work introduces a general probabilistic framework for the multiscale modelling of composite structures, calibrated on experimental data (Figure 3.1).

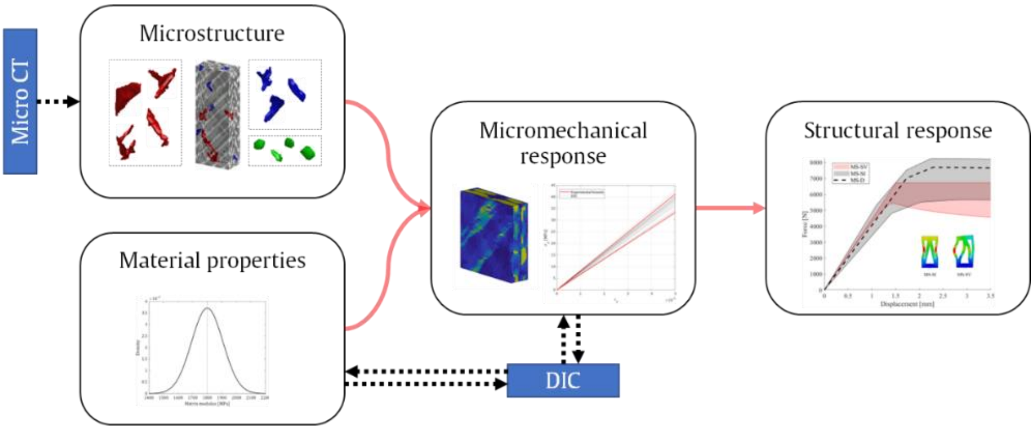

Figure 3.1. Multiscale framework calibrated on experimental data to model the uncertainty in composite structures.

The novelty of the proposed methodology relies on the combination of multiscale modelling and experimental characterization methods to capture the variation in the elastic response of the composite at the mesoscale[97].

3.2 Material characterization

3.2.1 Materials

The material under study is a glass fibre-reinforced epoxy matrix manufactured by hand lay-up. The matrix is the low viscosity (70 mPas) epoxy resin AXSON EPOLAM 2015 with a glass temperature of 90°, mixed with the EPOLAM hardener at 32% of weight fraction. The unidirectional E-glass fabric UNIE600 (ResinTex) has a surface weight of 661 g/m^2 and a total tex of 2400. The fibre diameter spans from 14 to 17 μm with a density of 2.60 ± 0.2 g/cm^3 and a nominal elastic modulus of 73 GPa. Laminates are produced in the shape of 300x300 mm plates and successively shaped to get rectangular specimens with a Wazer waterjet cutting machine. The laminates have a $[\pm 45]_6$ stacking sequence, with 12 layers in total, each with a nominal thickness of 0.7 mm, yielding a total laminate thickness of 8.55 ± 0.10 mm. Rectangular specimens are cut with a 25mm width and a length of 250 mm each and visually inspected to ensure that the cutting process has not induced any damage or delamination to the specimen.

3.2.2 Tensile tests

Tensile specimens where fixed with a total length between the grips of 150mm, as suggested by the ASTM standards D3039. The tests have been performed with the servo-hydraulic testing machine 8801 by Instron, equipped with a load cell with a 100 kN capacity and a displacement transducer. Specimens have been clamped with a hydraulic system, setting a closure pressure low enough to minimize the stress concentration at the interface. The test has been performed at a fixed displacement rate of the lower crosshead of 2mm/min, with an acquisition frequency of 20Hz for both load and displacement signals. The tensile tests were recorded with a high-resolution stereo camera system by Isi Systems, with a 4096 by 2160 pixels resolution and a frame acquisition frequency of 5 Hz. The experimental setup is shown in Figure 3.2. The cameras are controlled and calibrated with the VIC-3D software by Correlated Solutions, later used to compute surface displacements and strains on the specimen using the Digital Image Correlation (DIC) method.

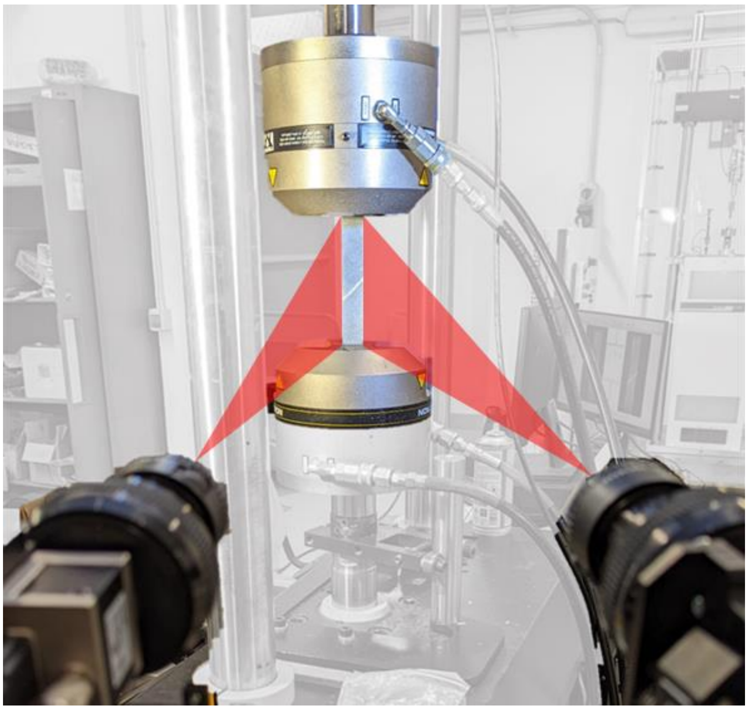

Figure 3.2. Experimental setup of the tensile test recorded with a stereo camera system for 3D Digital Image Correlation

3.2.3 Tomography scan

Specimens have been scanned with the Fraunhofer IKTS Computer Tomography scan available in Politecnico Labs with an open microfocus x-ray tube operating at a maximum voltage of 300 kV. The X-Ray detector has a size of 400 x 400 mm with 2048x2048 pixels (200 µm resolution). The X-ray image resolution was 5 µm under the most favourable conditions (i.e., sample size, scanning speed, sample shape). The object-to-detector distance and source-to-detector distance were set to 50 mm and 545 mm, respectively, yielding a voxel-edge resolution of 16 µm. The specimen has been placed with its main direction aligned to the rotation axis and scanned four times in each of the 1600 projection positions. The tube voltage and filament current have been set to 100 kV and 60 µA, respectively. To increase the accuracy of the X-ray images, an aluminium filter of thickness 0.2 mm has been used to cut out low-intensity rays.

3.3 Microstructure reconstruction

An inverse statistical methodology is proposed to calibrate an SVE for multiscale analysis from a macroscale tensile test and micro-CT scan. From the micro-CT data, the mesoscale structure of the laminate has been subdivided through a segmentation of the volume voxels into matrix, void, and tows (as described in the following). From the segmented voxel volume, the extracted laminate sub-regions (i.e., candidate RVEs) are converted to voxel mesh and transferred to a Fast Fourier Transform (Appendix A) solver developed in MATLAB. Similarly, as for the voxel mesh, surface sub-regions of the Digital Image Correlation maps with the same size have been extracted and an average stiffness has been computed from synchronous strain and load data (as will be described in Section 3.4). It is assumed that DIC measurements are descriptive of all the uncertain variables defining the material mechanical response, while the reconstructed CT-scan mesh is a deterministic description of the mesoscale geometry. On the base of these assumptions, the statistical distributions of the microscale material parameters have been optimized to best match the empirical distributions of the elastic modulus measured through DIC. To achieve these results, the cumulative distribution function (CDF) of the FFT results obtained by varying the material random variable will be compared with the experimental CDF extracted from the DIC. The loss function of the optimization scheme is defined as the p-value of the Kolmogorov-Smirnov[98] test, weighted on the test results (as it will be described in Section 3.5).

The X-ray image of the 1600 projections around the scanning axis has been imported into VGMax software to reconstruct a 3D volume of the specimen. The volume voxel-edge resolution is $16\mu m$, each voxel has a grey scale value between 0 and 255 that represents the absorbed power of the material in each position. Using a threshold algorithm on the greyscale distribution curve, materials have been differentiated from voids, assigning each voxel to one of these classes. Voids have been then processed with the VGDefX algorithm that clusters the void voxels and estimates the probability (p_p) that a cluster is a porosity (i.e., a defect), rather than an artefact. The probability has been weighted on the geometrical features of the clusters.

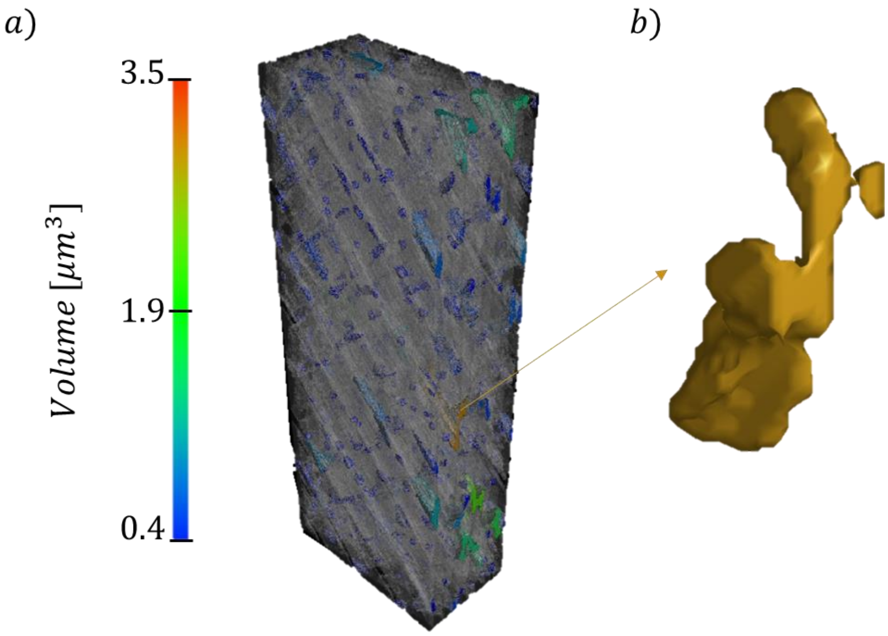

Figure 3.3. a) VGDefX results of a porosity analysis on a composite specimen b) an example of a pore identified in the composite material

Voxels labelled as “composite” are processed with the Fibre Composite tool by VGMax, which interpolates the grey values of the voxels and converts them to a volume fraction (v_f). The volume fraction of each voxel can be used to differentiate between matrix ($v_f = 0$) and fibre tows ($v_f \cong 1$). Since the resolution of the scan was twice the fibre diameter, the algorithm could not distinguish fibre and matrix within the tows, therefore the volume fraction computed with VGMax must be carefully treated, being limited by the CT resolution. To overcome this issue, a microscopic image of the tow has been taken to properly assess the fibre volume fraction within it.

The voxel discretized volume is exported into a MATLAB environment in the form of vectors containing voxel class labels, porosity probability, volume fraction, and spatial coordinates.

The continuous variables v_f and p_p have been converted into discrete values by defining the threshold values:

- t_p: probability threshold, voxel with a porosity probability above t_p have been labelled as pores, and the remaining voxels have been labelled as matrix.
- t_v: volume fraction threshold, voxels with a computed volume fraction above t_v have been labelled as tows, and the remaining voxels have been labelled as matrix.

The resultant mesh has been later divided into different layers by manually defining the layer interface positions along the thickness.

The reconstructed mesh is used as the seed to generate Volume Elements (VEs) by extracting a sub-volume of the mesh with a random position in the plane and a fixed number of layers. The size of the in-plane square and the number of layers then define the size and aspect ratio of the extracted VE.

3.3.1 Results

The parameters of the VGDefX algorithm [99] used to detect porosity in the scanned region are reported in Table 3.1.

Parameter	**Value**
Min. Volume [vox.]	1000
Max. Diameter [vox]	3000
Voxel count	0.3
Compactness	0.5
Scaled deviation	0.5
Ignore small defect	0.7
Sphericity	0.3

Table 3.1. VGDefX algorithm parameters for void segmentation

The result is a pore probability map with voxel values ranging from 0 to 100 as shown in Figure 3.4. Each map is characterized by the threshold t_p used to binarize the map itself and identify the void inside the specimen that affects the porosity volume fraction. The diagram at the bottom of the figure reports the variation of the resulting porosity with the threshold value.

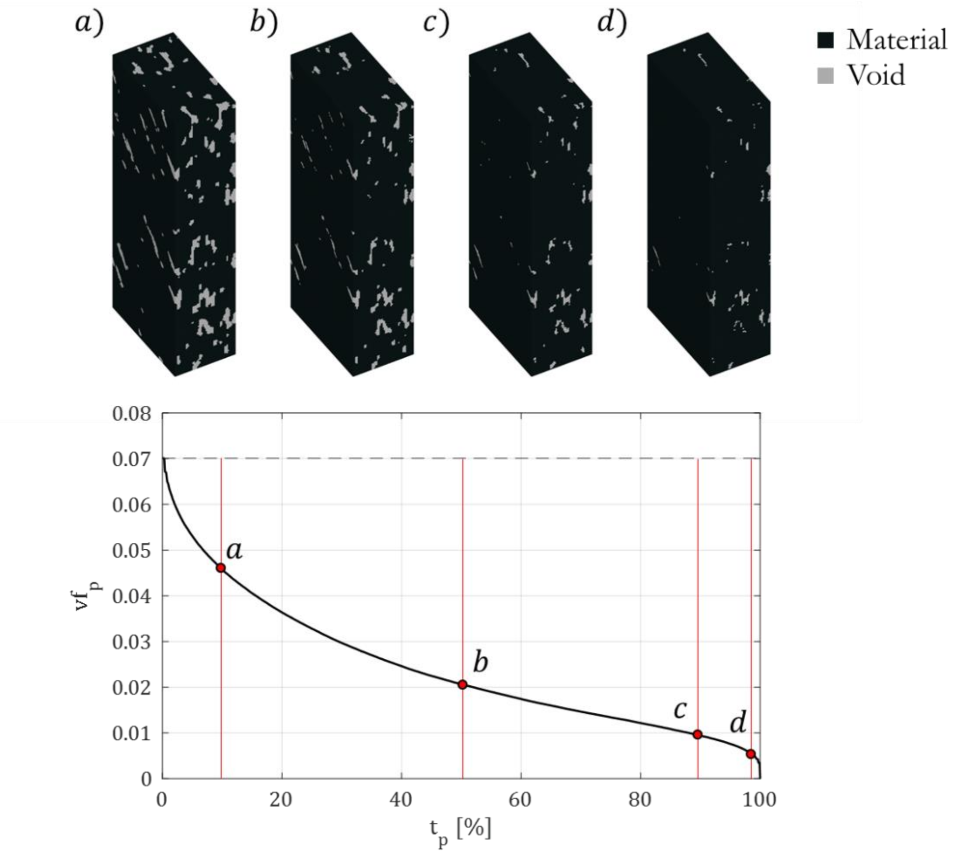

Figure 3.4. On the top the binarized porosity maps with a threshold of a) 10%, b) 50%, c) 90%, d) 99%. On the bottom, the variation of the porosity with the threshold value is expressed as a volume fraction.

After having analysed the morphology of the voids at different t_p, a threshold value of 10% (see the vertical red line in Figure 3.4), yielding a 4.6% porosity volume fraction, has been selected since the resultant shape and orientation correspond to what was observed with optical analysis. The voxels labelled as pores have been clustered with a density-based algorithm with a scanning distance of 190 µm and a minimum of 10 voxels per cluster, yielding approximately 370 clusters representing the material defects. For each defect, a sphericity index Φ has been computed, being Φ the ratio between the surface area of an equal-volume sphere and the defect surface area (A) in Equation 3.1:

$$\Phi = \pi^{\frac{1}{3}} \frac{(6V)^{\frac{2}{3}}}{A} \tag{3.1}$$

Figure 3.5 reports the sphericity index value and the main diameter of the segmented defects, revealing the presence of three distinguishable categories:

- Small spherical voids, characterized by the highest value of the sphericity index Φ, whose typical shapes are sketched at the top left of Fig. 3.5: most probably due to trapped air in the manufacturing stage. These are corresponding to what are typically named pores dispersed into the matrix.
- Fibre-oriented defects with elliptical shapes, characterized by the intermediate value of the sphericity index Φ, whose typical shapes are sketched at the top centre of Figure 3.5: defects are aligned to the fibre direction and contiguous to the tows, probably originating from a pure fibre to matrix adhesion.
- Interacting defects, characterized by the lowest value of the sphericity index Φ, whose typical shapes are sketched at the top right of Fig. 3.5: defects made of two distinguishable defects that merged into a larger one with a distorted shape.

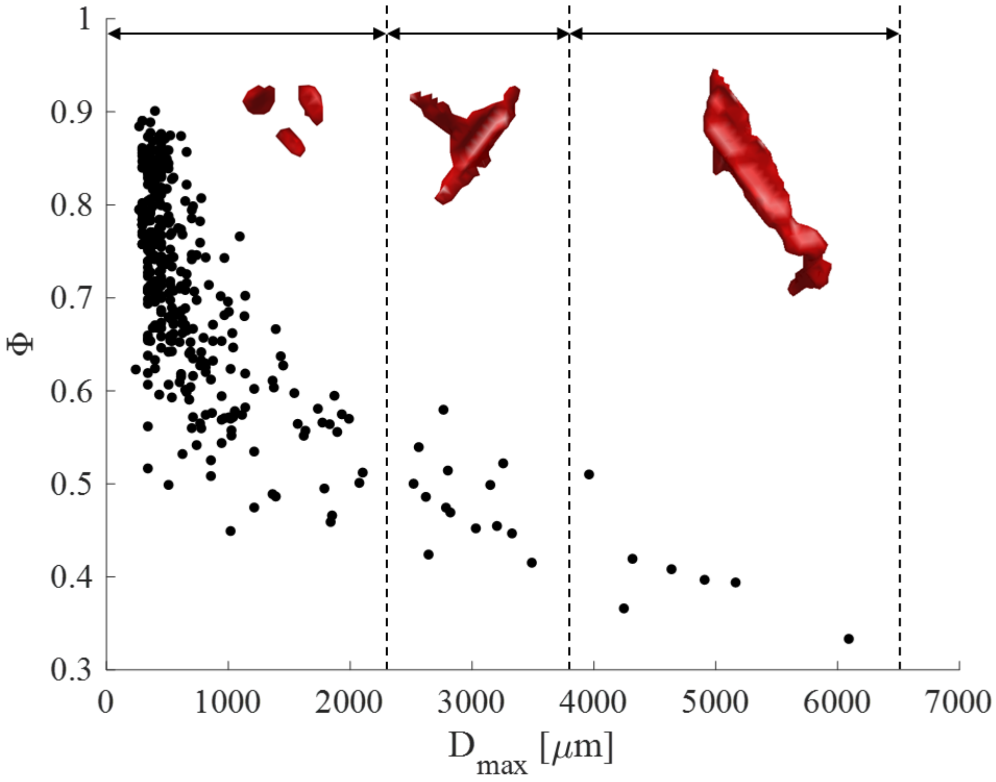

Figure 3.5. Sphericity computer for all the clustered defects against its main diameter. Representative defects of each interval are reported.

The categorized defects are reported in Figure 3.6 and their position inside the specimen is highlighted to show the alignment of the defects to the fiber direction.

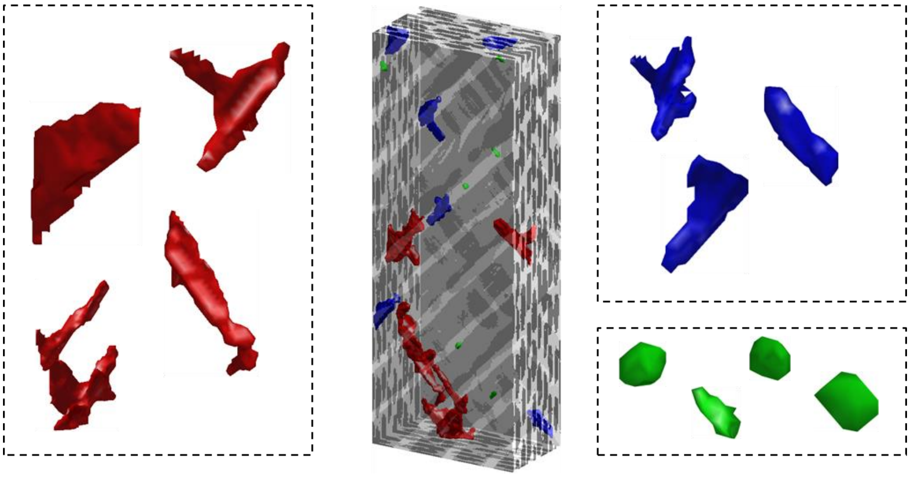

Figure 3.6. Reconstructed mesh with main defects grouped by sphericity and dimensions

The irregular shape of the tows has been analysed following the same approach used for the void segmentation, applying the density-based spatial clustering technique on the voxels labelled as fibre bundles. The reconstructed fibre bundles present geometrical irregularities both in terms of alignment and size. Figure 3.7a shows a slice of the reconstructed volume where the waviness of the fibre bundles can be observed. The variation of the fibre tows main diameter is reported for two different tows, 1.8 mm, and 2.2 mm respectively.

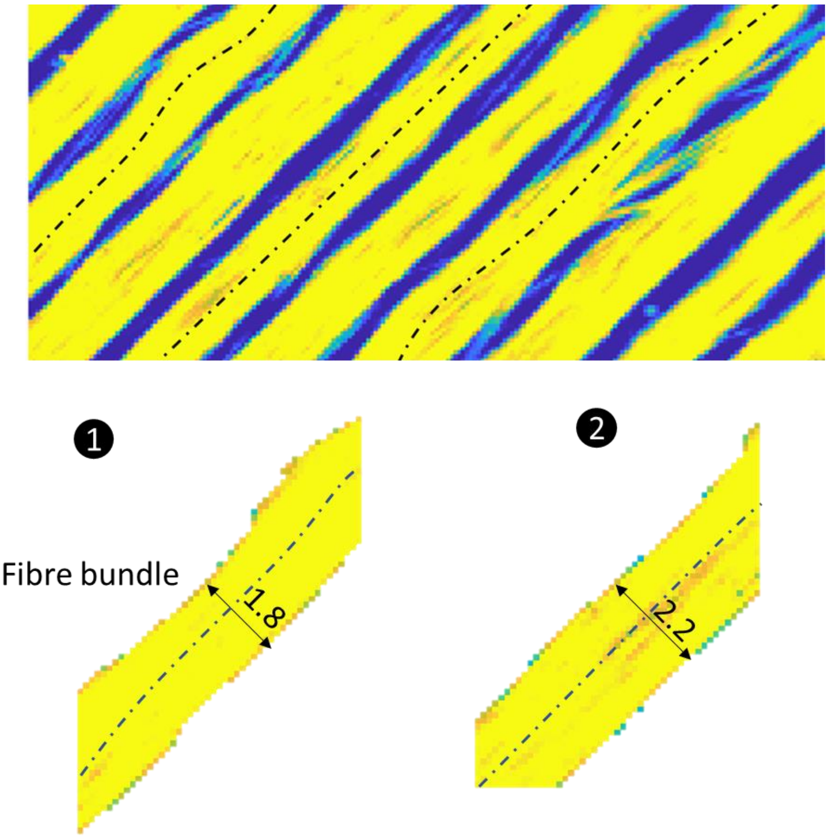

Figure 3.7. A slice of the reconstructed mesoscale structure of the composite where the waviness of the bundles is indicated with a dot-dashed line. In the bottom, two segmented sections of the two tows with different diameters and waviness. In yellow, the fibre tows, in blue the matrix/defects. Measurements are expressed in mm.

In the proposed approach, the variation of the fibre bundle geometry is accounted for by directly extracting the mesh of the RVE from the reconstructed structure of the composite at the mesoscale level. The effect of the bundle waviness and its size on the composite stiffness is thus obtained from the experimental reconstruction, following a data-driven fashion rather than modelling its variability into an artificially generated RVE.

3.4 Multiscale parameters estimation

3.4.1 RVE size estimation from FFT on CT reconstruction

RVE is the smallest volume over which a measurement can be made that yields a value representative of the whole. The RVE size is commonly identified by computing the homogenized mechanical response (e.g., tensile stiffness) of the VEs with increasing size until the quantity of interest remains unchanged and its standard deviation is below a defined threshold [100]. Therefore, multiple VE with increasing size have been extracted and the homogenized in-plane shear modulus G_{12} has been computed with FFT simulations, until it converged to a stationary value.

3.4.2 RVE size estimation from DIC measurements

The DIC strain map resolution of 0.3 mm is approximately one-sixth the fibre tow width, yielding an inhomogeneous distribution of the surface strain. It is then possible to compute a homogenized strain value over a surface sub-region with Equation 3.2:

$$\bar{\varepsilon} = \frac{1}{\mathrm{A}} \int_{\Omega} \varepsilon(x, y) dS \tag{3.2}$$

where Ω is the surface sub-region with area A, and $\varepsilon(x, y)$ is the strain field computed with the DIC. Let's assume that the stress $\bar{\sigma}_y$ in every point is equal to the applied stress that can be measured by dividing the measured force over the cross-sectional area. On the specimen surface, the out-of-plane stress is assumed to be negligible, thus a plane stress condition is defined, which yields Equation 3.3:

$$E_y = \frac{(1 - \nu_{12})\bar{\sigma}_y}{\bar{\varepsilon}_x + \nu \bar{\varepsilon}_y} \tag{3.3}$$

The homogenized longitudinal modulus has been computed for sub-regions with increasing size, i.e., Surface Representative Volume Element (S-RVE). Similarly, the in-plane shear modulus G_{12} can be computed from Equation 3.4

$$G_{12} = \frac{\bar{\sigma}_y}{2\left(\bar{\varepsilon}_y - \bar{\varepsilon}_x\right)} \tag{3.4}$$

The RVE size has been defined by analysing the convergence of the homogenized moduli with the increasing area.

The proposed methodology underlies the fundamental assumption that the in-plane strain measured on the specimen surface is representative of the average strain through the thickness. Previous works [101,102] have investigated the stress concentration on the surface of the textile composites induced by the material microstructure. It has been assessed that an increase of the stress (or strain) in the woven composite is induced by the local unbalancing of the laminate determined by the woven architecture. The induced momentum can be computed as

$$\frac{\Delta F}{F} = \left(\frac{1}{2} - \frac{t}{h}\right)\left(\frac{N}{N-1}\right) \tag{3.5}$$

where h is the ply thickness, and t is the distance from the unit cell surface and the yarn midline. In the case of the bundled unidirectional composite under study, *t* is half of the cell thickness, yielding a null induced momentum on the outer surface. It can be then concluded that in the case of the unidirectional composite under study, the surface stress is not altered by the material structure.

3.4.3 Results

3.4.3.1 RVE size estimation from FFT analysis on CT reconstructed mesh

The RVE size estimation with FFT analysis of the reconstructed mesh has been conducted by investigating the variation of the laminate elastic modulus along the y direction. The glass fibre has been modelled as isotropic with Young’s modulus of 72 GPa and a Poisson’s ratio of 0.2, while the initial guesses for the epoxy matrix Young’s Modulus were 2 GPa with a Poisson’s ratio of 0.35, as reported in the literature [103].

The initial RVE size has been set to 3.6 mm, and successively increased approximately by 0.5 mm up to 11.0 mm (see Figure 3.8). Selection for the representative value is done when the standard deviation of the homogenized modulus converges to an asymptote (a little bit larger than 4% in Figure 3.9), whose value depends on the randomness of the microstructure extracted from the CT data. To get a statistic of the homogenized moduli, five FFT simulations have been performed for each candidate RVE, by sampling a sub-volume of the reconstructed mesh (Figure 3.8).

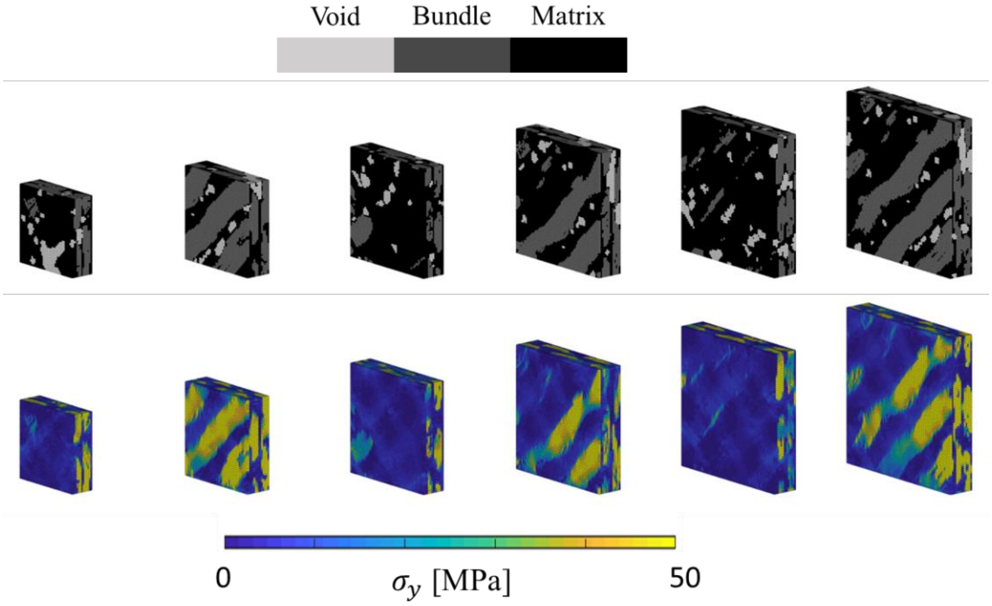

Figure 3.8. a) Six examples of the microstructure of heterogeneous volume elements reconstructed from the CT images. b) Longitudinal stress on the volume element when a uniaxial strain of 0.01 mm/mm is applied along the y direction. The RVE size is 4.5, 5.5, 7.5, 8.5, 10, and 11 mm, from left to right.

Figure 3.9 shows the results of the RVE size analysis, where it is visible the convergence of the E_{22} at a mean value of 7.2 GPa for 7 mm RVE size, where the standard deviation is approximately 5% of the mean value.

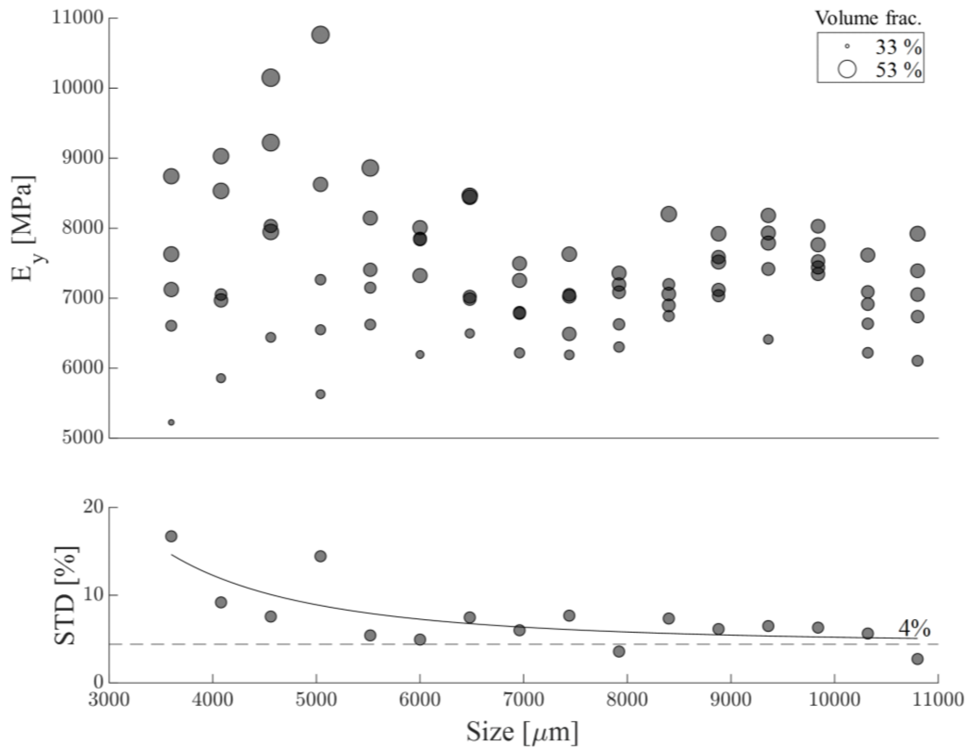

Figure 3.9. Convergence study of the RVE size estimated from FFT analysis on CT reconstructed mesh

The effect of defects on the RVE response has been studied by computing the response of reconstructed microstructures where voids have not been considered, and matrix material has replaced them. The results reported in Figure 3.10 show that defects induce a larger scatter in the material response since the randomness of the material microstructure not only depends on the fibre arrangement (bundles shape, bundles alignment, matrix-rich zones) but also on the presence of defects that significantly affect the mechanical response. More specifically, results in Figure 3.10 show that the homogenized modulus of the defect-free material converges to a 10% higher mean value, as expected.

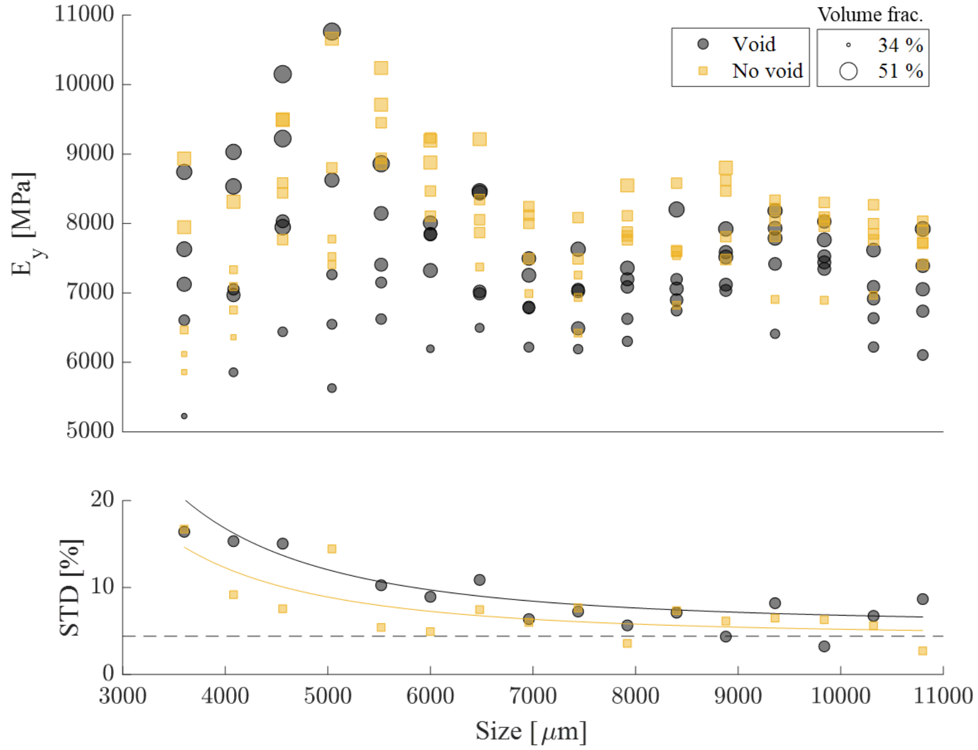

Figure 3.10. On top, the homogenized modulus computed with FFT simulations of reconstructed microstructures, on the bottom, the standard deviation normalized to the mean.

Since the proposed analysis investigates the elastic response of the composite at different scales, the absence of any plasticity at the mesoscale (i.e., micro-plasticity) has been verified by analysing the equivalent Von Mises stress values computed at the matrix voxels with the FFT calculations. Figure 3.6 shows the equivalent stress of the matrix voxel values of each FFT simulation computed over different RVEs. The histograms contain all the computed values, whose distribution has been fitted with a logarithmic normal probability density function (pdf), with a mean value of 1.03 ln(MPa) and a deviation value of 0.47 log(MPa).

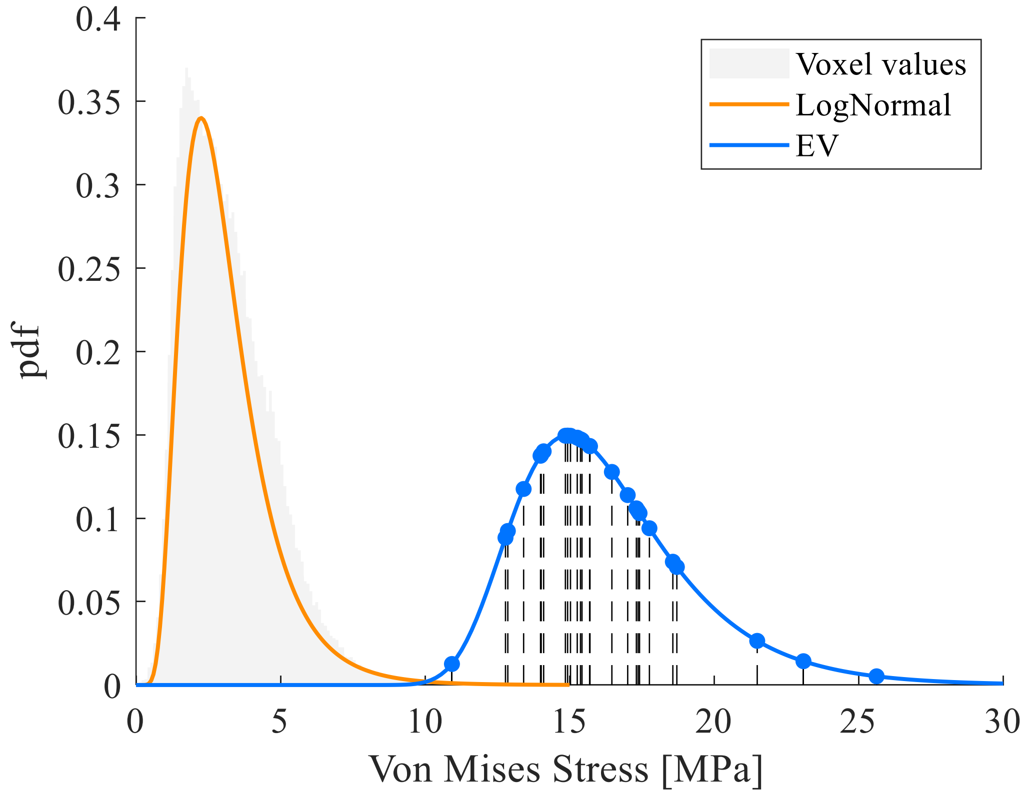

Figure 3.11. The equivalent Von Mises stress computed at each matrix voxels of the FFT calculations computed over different RVEs. The histogram reports all the voxels' values, while the orange line represents the logarithmic normal distribution fitted on the data. The dashed black lines and filled blue dots indicate the maximum Von Mises stress at each simulation, while the blue line shows the extreme values distribution fitted on the maximum stresses.

The distribution of the equivalent stress in the matrix has been compared with the yield stress values of the epoxy matrix, which is between 30 MPa and 50MPa as reported in the literature [103]. It can be concluded that the average matrix response in the analysed model is within the elastic regime. The maximum values of the equivalent stress of the matrix within each RVE are reported in Figure 3.11. The probability of having micro-plasticity in the extracted RVE can be described with the extreme value (EV) distribution with a mean value of 15 MPa and deviation value of 2.5 MPa, confirming that it is very unlikely to have plastic deformation in the analysed RVE at the defined strain level.

3.4.3.2 RVE size estimation from DIC measurements

The adopted procedure for the estimation of the RVE size from the synchronized strain map and the load-displacement curve is presented in this Section. At each candidate size, 10 subdomains of the specimen surface have been extracted by randomly selecting the centre. Figure 3.12b shows the stress-strain curve of all the extracted subdomains with distinct sizes, while the colourmap of Figure 3.12a shows the strain along the y direction measured with DIC. The red dots on the specimen represent the centroids of candidate S-RVEs. One can note the higher density of these dots near the centreline due to the progressive reduction of the sampling subdomain with the RVE increasing size. The red curves are related to different S-RVEs.

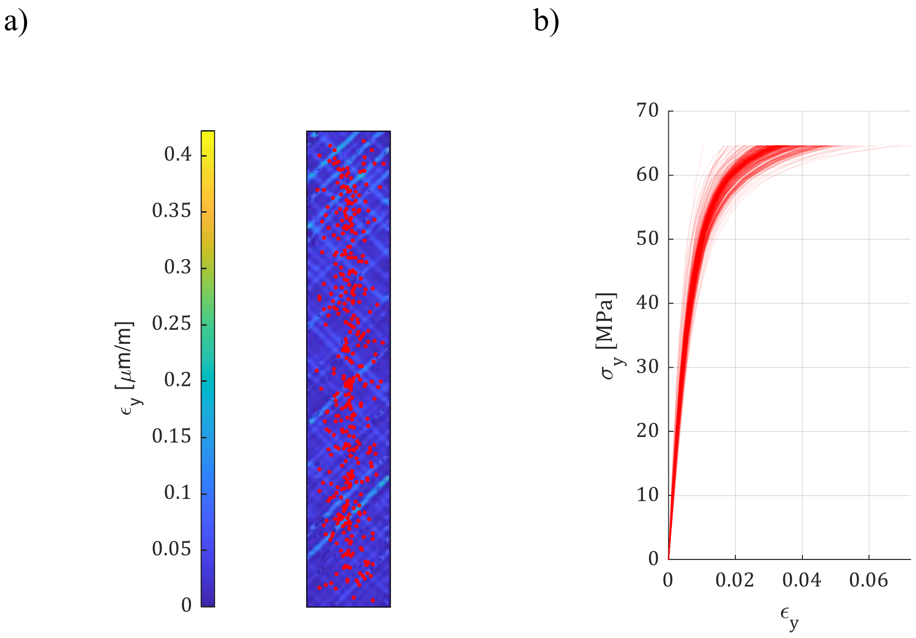

Figure 3.12. a) Centroid of the RVE displayed on the strain maps at a nominal stress of 20MPa. b) The homogenized stress-strain response of different RVE with different sizes extracted from the DIC map.

Applying Equations 3.2 and 3.3 to the extracted sub-volumes, the mean and standard deviation of the transverse Young's modulus E_2 at each size have been computed (see Figure 3.13).

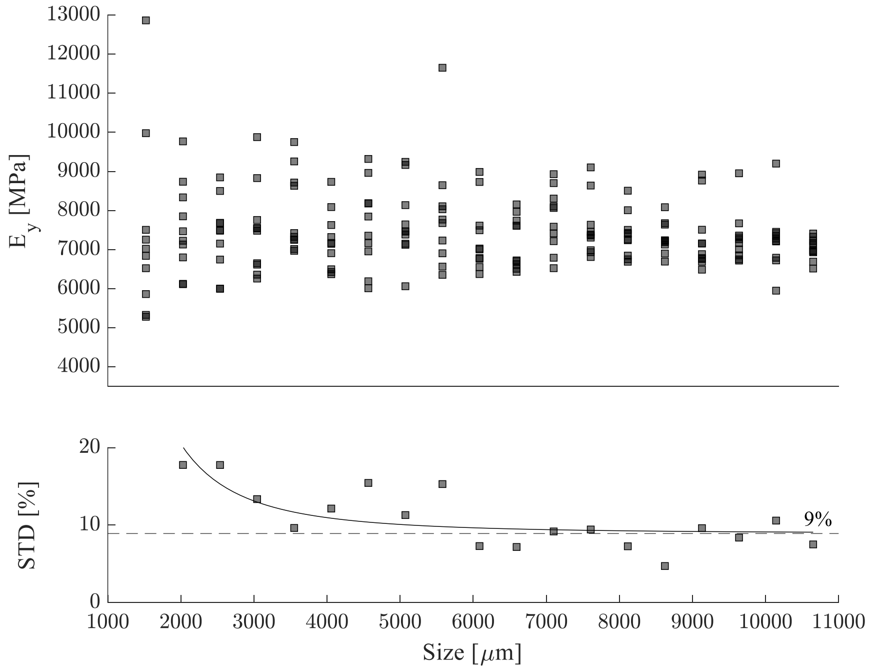

Figure 3.13. Analysis of the results for the transverse Young's modulus from the DIC measurements during the tensile test as a function of the RVE size.

Results show a fast convergence of the transverse Young's modulus E_{22} to the mean value of 7.2 GPa. The standard deviation for the 10 samples extracted from the strain maps converges to a value of 9% of the mean value, for an RVE size of 7 mm approximately. As it can be noticed in the upper diagram of Figure 3.13, even with a larger area, the computed transverse Young's modulus has a quite large scatter arising from the DIC measures, suggesting the presence of spatially inhomogeneous properties of the material.

3.4.3.3 Comparison

In the diagram of Figure 3.14, the results from the two presented methods are reported for values of size ranging from 1.5 mm up to 11 mm. It is relevant to observe that the mean value of the transverse Young's modulus E_{22} computed with FFT on the reconstructed mesh converges to the homogenized value computed from the DIC maps equal to 7.2 GPa (Figure 3.14a), while the in-plane shear modulus G_{12} converges to an average value of 2.5 GPa (Figure 3.14b). The RVE size extracted from the DIC analysis is between 7 and 8 mm, accordingly to what was computed with the FFT simulations. The standard deviation of the homogenized elastic modulus computed with FFT approached the asymptotic deviations of 4%, while the results from the DIC maps show a larger scatter with an STD that oscillates around 9%.

a)

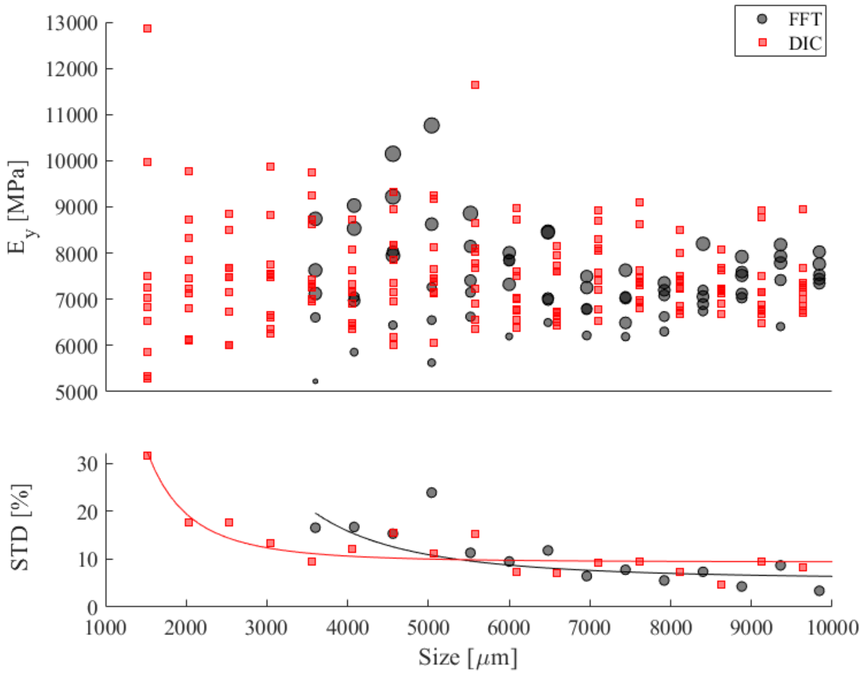

b)

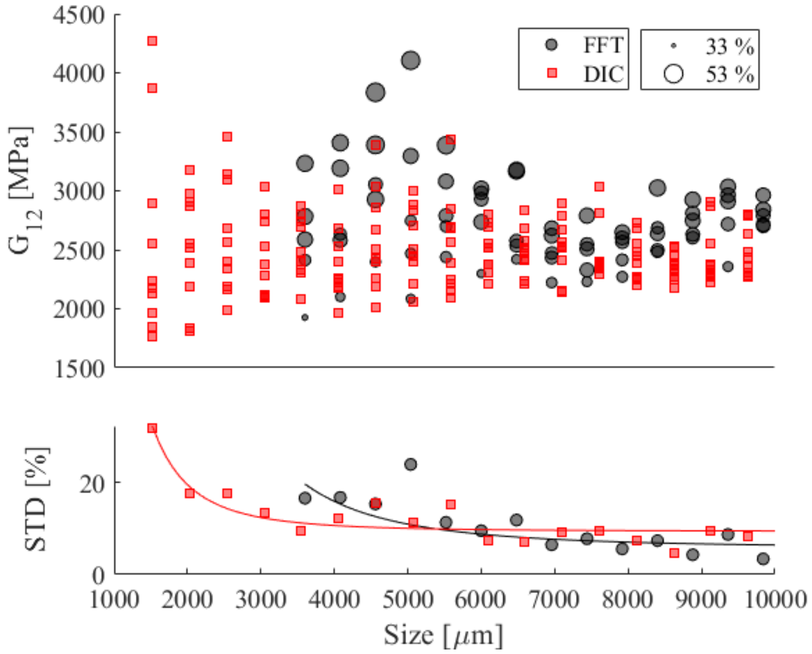

Figure 3.14. Comparison of the mean value and standard deviation of the transverse Young's modulus E_{22} (a) and in-plane shear modulus G_{12} computed from FFT on CT reconstruction and DIC.

The results show that the FFT model predicts a distribution of Ey with a standard deviation of 0.5 GPa, i.e., a smaller value compared to the 0.75 GPa obtained from the analysis of the experimental DIC measurements (Figure 3.15). This 0.25 GPa difference in the standard deviation suggests that the model does not account for all the stochastic phenomena that govern the elastic response of the material and raises the need for further investigation into the sources of uncertainty.

a)

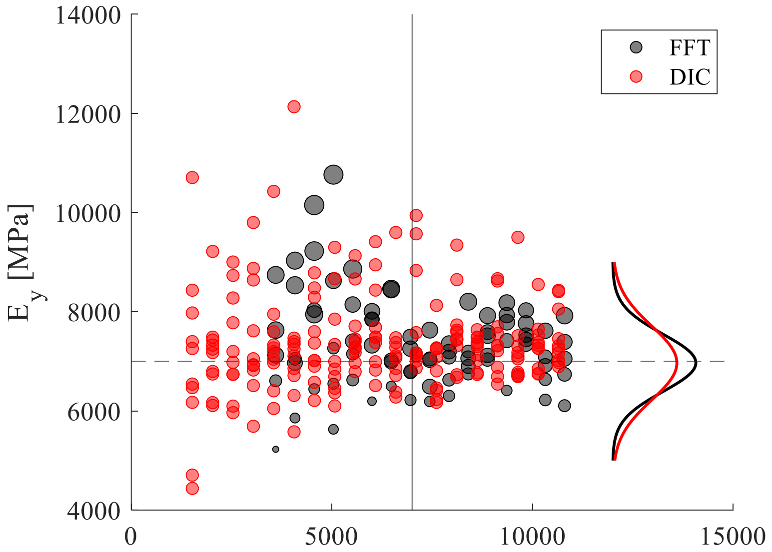
14000
12000
10000
8000
6000
4000
0
5000
10000
15000
E_y [MPa]
FFT
DIC

b)

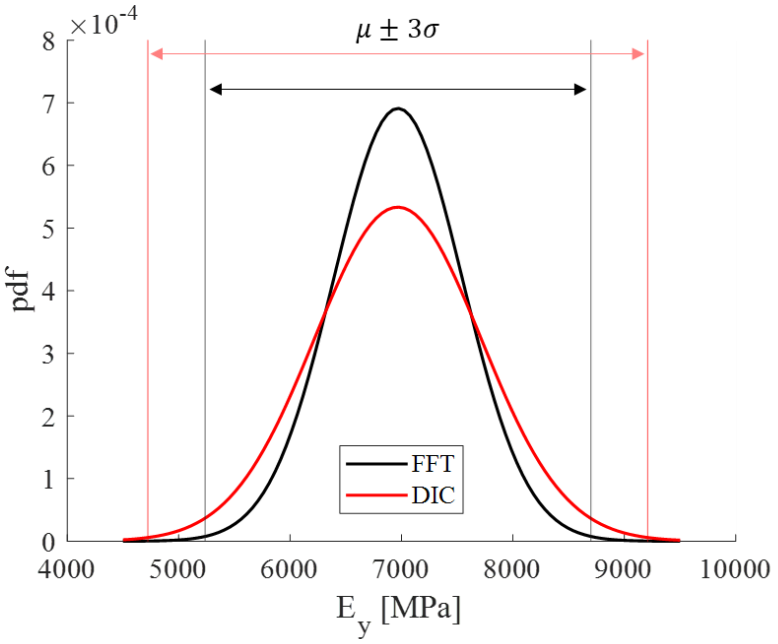
×10^-4
8
7
6
5
4
3
2
1
0
pdf
μ ± 3σ
FFT
DIC
4000
5000
6000
7000
8000
9000
10000
E_y [MPa]

Figure 3.15. a) The homogenised composite modulus extracted from the DIC data is compared with the one computed with the FFT model on the experimental microstructures. The fitted distributions of the modulus computed on volumes with size equal or higher to 7mm (i.e., the RVE size) are indicatively reported on the right side of the graph, while b) shows a magnification of the two normal distributions where the ±3σ interval is reported.

The FFT model combined with the experimental microstructure reconstruction only accounts for the defects-induced spatial variability. Indeed, the material properties have been considered spatially invariant, while recent findings demonstrated[76] the variability of the matrix properties within composites.

Therefore, both the adopted approaches are not completely satisfactory. To overcome the evidenced limitation a novel procedure has been devised. First, it is needed to assess this properties variability in the composite material, to this scope, an inverse calibration method has been applied to quantify the uncertainty imputable to the properties variability and efficiently capture it in an SVE.

3.5 Stochastic Volume Element (SVE) calibration

The mechanical response measured with tensile test and DIC is representative of the glass fibre material and intrinsically contains all the variance associated with porosities, variable local volume fraction, and variable matrix properties over the specimen volume. While the geometrical irregularities can be measured with the CT scans, the statistical distribution of the constituent properties is unknown and a punctual measurement, e.g., with a nano-indenter, would require an extensive characterization campaign with additional characterization experiments. The objective of the proposed method is therefore to estimate the variation of the elastic response at the mesoscale, that is an average response of the nanoscale variations related to the crosslinking of the polymers governed by the curing kinematics[94]. The proposed is an inverse method to calibrate the statistical distribution of the constituent properties by minimizing the difference between the CDFs of the homogenized properties drawn from the FFT simulations with variable matrix modulus and from the DIC measurements. The empirical CDF is inferred from the tensile test fitting the homogenized stiffness distribution obtained by repeating the procedure described in Section 2.3.4 with the computed RVE size. The CDF of the

FFT model, F_E^{FFT}, can be estimated from the conditioned probability $F_{E|E_m}$using Equation 3.6:

$$F_E^{FFT} = \int F_{E|E_m} f_{E_m} dE_m \tag{3.6}$$

where $F_{E|E_m}$ is the conditional CDF of the homogenized modulus at a fixed Young's modulus of the matrix, E_m, and f_{E_m} is the probability function of E_m. $F_{E|E_m}$ is computed from the homogenized modulus of 10 RVE simulations, with different randomly selected locations in the scanned volume, with a fixed E_m. The conditional CDF has been computed at different E_m, sampled within the range from 1 GPa to 4 GPa.

The distribution of the matrix modulus has been assumed to be Normal, with mean μ and standard deviation σ obtained with an optimization procedure. The adopted optimizer finds the μ and σ values that minimize the loss function in Eq. 3.7:

$$\mathcal{L} = 1 - pp(1 - hh) \tag{3.7}$$

where pp and hh are the p-values of the Kolmogorov-Smirnov test, and the test results at a significance level of 10%, respectively.

The test statistic is the maximum absolute value between the empirical cdf calculated from the DIC data and the hypothesized conditional CDF:

$$D^* = \max\left(\left|F_E^{DIC} - \int F_{E|E_m} f_{E_m}\left(\mu_{Em}, \sigma_{E_m}\right) dE_m\right|\right) \tag{3.8}$$

The critical value for text acceptance is computed with the empirical formula described in [104].

The gradient-based optimization algorithm used for the calibration of the distribution of the matrix modulus is based on the interior-point approach to constrained minimization, able to solve optimization problems with inequality constraints. More details on the algorithm are given in [105].

3.5.1 Results

The inverse calibration method introduced in Section 3.4, requires the CDF of the homogeneous modulus probability conditioned on the matrix Young's modulus (Eq. 3.6). To get this statistic, twenty values of E_m have been sampled around the expected value of 1.9 GPa, and the conditional homogenized modulus has been computed at each value with an FFT analysis. Using Eq. 3.8, the best Normal distribution parameters have been found for E_m that can capture the variability of the homogeneous modulus observed in the DIC data. It is worthy of note that the distribution of the local composite modulus, as it is well visible in the diagram of Figure 3.16b, is well described by a normal distribution.

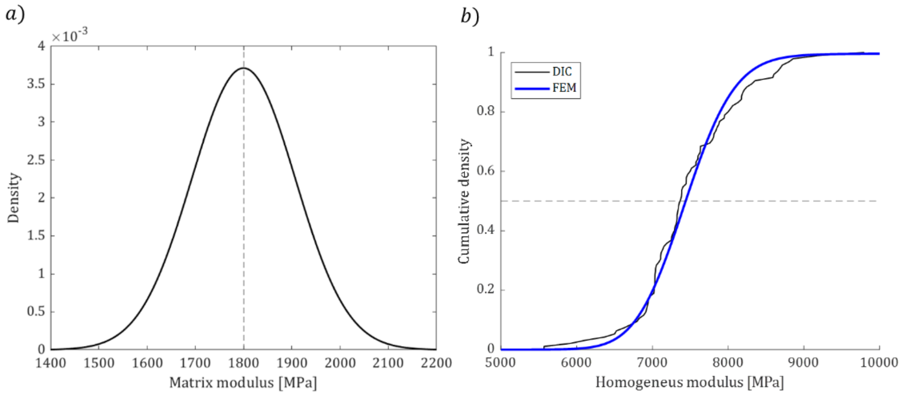

Figure 3.16. a) Calibrated probability density function distribution of the matrix Young's modulus. b) Cdf of empirical composite modulus measurements from DIC and of SVE compared

The optimization process converged to a mean value of matrix Young’s modulus equal to 1800 MPa with a standard deviation of 105 MPa (Figure 3.16a) after 15 iterations. The loss function is defined with Eq. 3.7 and had a value of 0.29, yielding a p-value of 0.7. Figure 3.16b compares the cumulative distribution function of the SVE with the one computed from the DIC, revealing a good agreement between the experimental and numerical curves.

Finally, the composite response has been calibrated using the calibrated SVE and the results have been compared with the curve extracted from the tensile test (Figure 3.17).

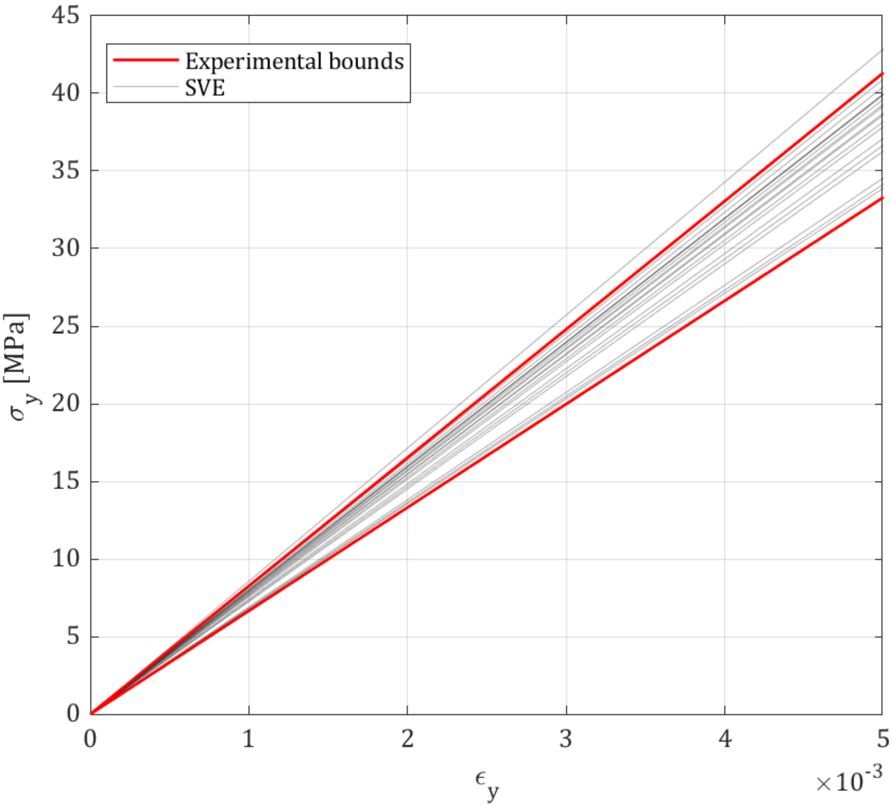

Figure 3.17. Comparison between experimental curves computed from DIC maps (only upper and lower bounds are shown) and SVE results with calibrated parameters.

3.6 Probabilistic multiscale model

The proposed methodology wants to establish a multilength scale statistical microstructure–constitutive property relation for the design of composite parts. To demonstrate the relevance of the method, a hierarchical statistical multiscale finite element model based on the generated SVE has been developed to predict the buckling critical load of a GFRP structure. The proposed test has been virtually simulated to give a demonstration of the method's capabilities and underline the main features of the proposed work. The analysis has been performed on a structure with 2 mm thickness, whose shape is described in Figure 3.18

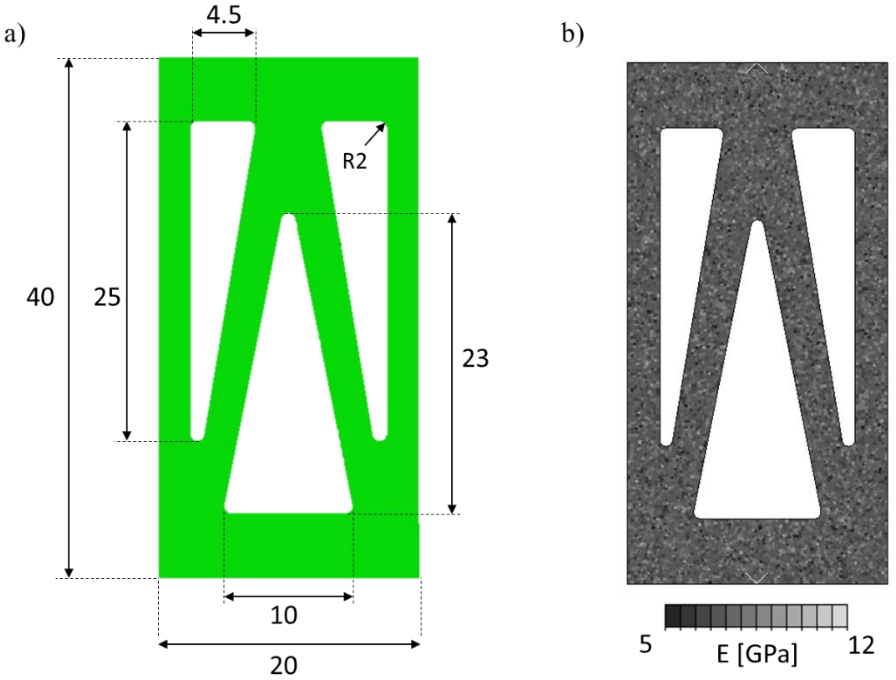

Figure 3.18. a) The geometry of the virtually tested structure. B) The elastic modulus map assigned to the part with the SV-MS approach.

In the following, the results of three different models are presented:

1. Deterministic multiscale (D-MS): the homogenized properties of the material are extracted from an RVE with average properties.
2. Spatially invariant statistical multiscale (SI-MS): the homogenized properties are extracted from the SVE and applied uniformly over the domain.
3. Spatially variable statistical multiscale (SV-MS): the homogenized properties of each material point in the model are extracted from the SVE and differ over the domain.

To estimate the uncertainty of the statistical models, SI-MS and SV-MS have been run twenty times each. The SI-MS adopts the same SVE for every material point in the structure, with the matrix Young's Modulus drawn from the calibrated distribution and the microstructure randomly extracted from the scanned volume. The SV-MS model is built by sampling twenty SVE, with E_m randomly extracted from the estimated Normal distribution and the microstructure randomly sampled from the scanned volume.

The SV-MS procedure is reported in the following.

```
SV-MS algorithm
-----------------------------------------------
Build the FE mesh of the part
Divide the elements into N groups
for each group i
    Sample a value of Em
    Sample an SVE from the reconstructed volume
    Run the FFT homogenization
    Generate the ith material card
    Assign the material card to the ith group elements
end for
```

Algorithm 3.1. SV-MS algorithm

The homogenization step consists of three simulations, needed to assess the homogenized elastic constants of the orthotropic stiffness matrix of the shell elements. Young's moduli along the x and y direction, together with the shear modulus and Poisson's coefficient in the *xy* plane are estimated. Figure 3.18b shows the map of the assigned moduli to the elements of the structure.

The diagrams in Figure 3.19 report the force-displacement curves from the stochastic simulations. It can be observed that the stiffness of the structure is more variable in the SI-MS simulations, where the random value of the matrix modulus is globally assigned to every material point in the structure, leading to a larger scatter in the global response. The SV model predicts a variable global stiffness with a smaller deviation from the global stiffness computed with the D-MS. Indeed, the spatially variable method preserves the statistical distribution of the material properties over the structure domain, yielding an average result close to the mean predicted with the deterministic model.

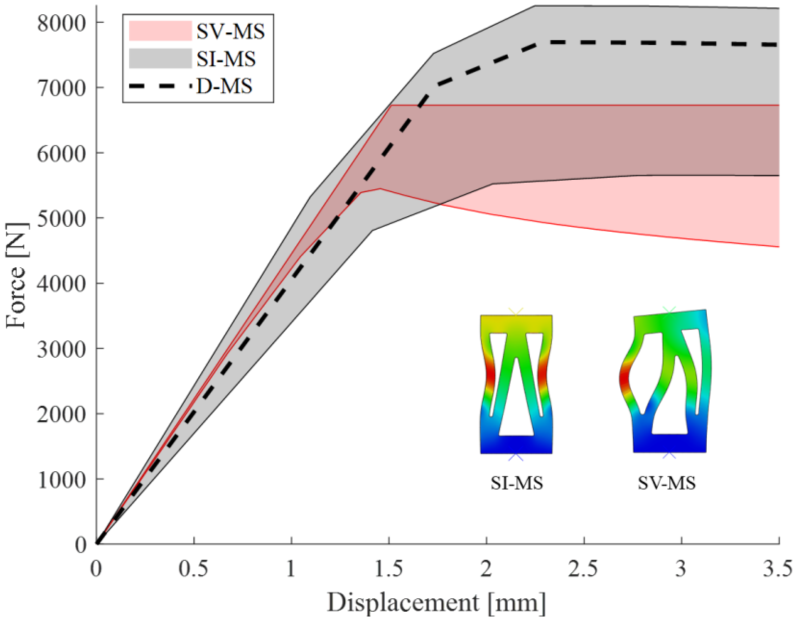

Figure 3.19. Results of SV-MS and SI-MS models of skin buckling

In Figure 3.20, the critical load and global stiffness of each simulation are reported in a box plot. The critical load predicted with the SV-MS is always lower than the one predicted with the D-MS. In effect, it can be observed that asymmetric modes are triggered in the spatially variable model. The buckling response is indeed governed by local phenomena and more compliant SVEs concentrated in the slender regions of the structure lead to local buckling instabilities (as reported in Figure 3.19). The lower critical loads are attributable to asymmetric buckling modes, that, in the case of this symmetric structure, neither the D-MS nor the SI-MS can predict.

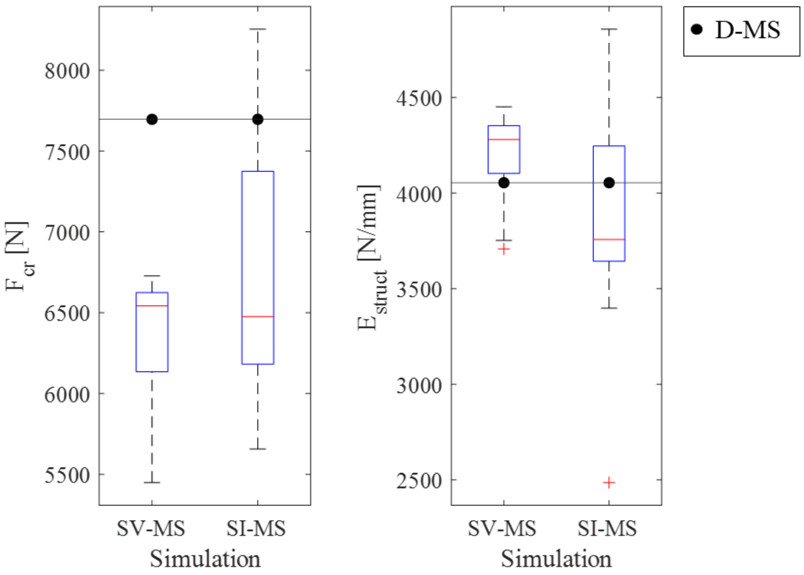

Figure 3.20. Critical buckling load and structure global stiffness computed with SI-MS and SV-MS statistical models

It can be concluded that the SV-MS model, by streaming the uncertainty from the microstructural to the macroscopic scale, allows for the prediction of structural behaviour triggered by the intrinsic variability of the composite material.

3.7 Conclusions

In this Chapter, a novel methodology has been introduced to complement the experimental observation about the mechanical response of the heterogeneous materials, as the full-field strain data measured with DIC, with the microscopic description of the material, obtained with CT scans. Leveraging the multiscale modelling theory, the microstructural response and the lower scale representation of the material structure are bridged to fully harness the experimental data and assess the mechanical performance of the parts in a data-driven and probabilistic fashion.

With the presented method, the link between the microstructural variability and its intrinsic defectiveness with the uncertainty of the mechanical response is modelled and calibrated with an inverse procedure, avoiding the shortcomings of micromechanical testing. The estimated uncertainty is then propagated from the lower to the higher scale by introducing a probabilistic multiscale model based on the SVE.

Summarising, the proposed method:

- Defines the RVE (or SVE) size from the experimentally measured strain maps of DIC, showing consistency with the numerical procedure based on full field homogenization (e.g., FFT),
- Estimates the uncertainty of the material model parameters used in the microscale representation of the heterogeneous material from the CT reconstructions of the microstructure and strain map from DIC,
- Defines an SVE used in a statistical multiscale model propagating the uncertainty from the microscale to the structural level.

To assess the method potentials, the multiscale model has been used to predict the buckling response of a GFRP structure, showing that it can predict mechanical responses originating from the statistical variability of the material properties over the spatial domain. Results confirm the importance of propagating the measured microstructural uncertainties, to the structure level and predicting its effect on the mechanical response. The presented method is, at this stage, limited to the elastic analysis of heterogeneous materials, while future developments will extend the applicability to the plastic and damage models to assess the multiscale uncertainty relation beyond the elastic regime.

4 Physics-informed machine learning for the design of the axial crashworthiness of crash tubes

4.1 Introduction

The previous Chapters introduced data-driven techniques to model the mechanical response of materials from the experimental observation, bridging the data available at different material scales with a multiscale approach driven by the MDS method. Although the challenge of defining the material response is of crucial importance in the design process, most of the effort is spent on the design of the structure (or part) that follows an iterative optimization process based on numerical simulations (e.g., the FEM). In the last decade, continuous improvements in data science have opened the door for the development of fast and yet accurate models that can surrogate structural simulations, accelerating the overall design of the parts.

The application of such methods could enhance the productivity of any design process, especially where the computational models are extremely expensive and the optimization procedure could go through numerous iterations, as in the case of automotive passive safety components.

The safety requirements for vehicle crashes are escalating due to several factors. Firstly, there is a growing emphasis on reducing the risk of occupant injury and fatalities in accidents. Additionally, stricter regulations are being implemented to ensure vehicles meet higher safety standards. The latest regulations from the NCAP have set higher safety requirements for the vehicles, increasing the speed in most of the critical tests and introducing additional crash tests for the assessment of overall vehicle safety. From the engineering perspective, the effective enhancement of the body's structural performance in crash scenarios necessitates the integration of multiple factors, and conventional optimization methods reach their limitations when tackling this issue. Furthermore, due to the profoundly non-linear nature of crashes, discovering a crash structure configuration that achieves optimal behaviour (efficiently absorbing substantial energy, minimizing weight, and adhering to manufacturing limitations) is exceptionally intricate. Consequently, the design procedure remains predominantly manually driven, relying heavily on the expertise and accumulated knowledge of engineers developed over time. Novel methodologies that can leverage the engineering knowledge of the crash mechanism, while reducing the design time, are then necessary to foster the design of these structures and efficiently target the safety requirements.

Crash boxes play a crucial role in energy absorption during vehicle impact. Crash boxes are sacrificial components which aim at absorbing the kinetic energy during low-velocity impact events through mechanical deformation, thus limiting injuries to the occupants, and preserving the structural integrity of the rest of the front car body, of the components in the engine compartment and the vehicle suspension system. To reach the goal of low-weight yet safe structures, composite materials are increasingly adopted in the design of crash absorbers, given their superior specific mechanical performances compared to metals. Several studies and applications of composite materials in crash tubes are reported in the literature, showing the good mechanical performances in crash absorbers [106–108].

Among the different design solutions, pre-folded origami tubes have shown a consistent reduction of the peak force and comparable energy absorption capabilities [109] if compared with conventional geometries, which results in reduced acceleration to vehicle passengers and improved safety. Zhao et al. [110] proposed a geometrical optimization of cylindrical origami tubes to enhance the energy absorption capability. Similar works [111–114] on different origami pattern tubes have demonstrated the benefits and the wide domain of solutions achievable with these structures. More recently, Wu et al. [115] have proposed a design strategy to avoid unstable global bending in the axial crash. They showed that the crush response of specifically designed origami tubes followed the deformation of the crease, thus avoiding global bending. Ye et al. [116] have shown that the brittle failure of hybrid tubes made of carbon fibre and Kevlar fibre-reinforced plastics, which is difficult to predict and can lead to inefficient use of the material, can be prevented through origami patterns. For a comprehensive and recent review of the topic, the reader can refer to the work published by Ma et al. [117].

The main advantage of origami patterns is that different from the standard square, tapered or cylindrical geometries, a change in the geometrical parameters of such structure does not affect the mass of the component. Thus, the geometrical parameters can be tuned to maximize the crushing performance of the structure while keeping a target mass. Further, pre-folded tubes can be designed to achieve stable and progressive crushing mode.

Structural optimization indeed assists in designing crash-worthy and lightweight structures. However, given the high influence of the shape on the collapsing mode and the absorbed energy, especially in the case of composite materials, the identification of the optimal configuration is challenging in crashworthiness design problems, which are generally ill-posed [118,119]. A large amount of data, both experimental and numerical, is required to assess the influence of the tube shape on its crushing response. To reduce the computational time, while gaining information on the whole design domain, previous research has increasingly adopted surrogate modelling techniques, especially in crashworthiness problems [120–123]. Modified approaches have been also proposed, which aim at reducing the design domain at each iteration of the optimization problem or at increasing the accuracy by sampling in the proximity of an optimal configuration [120,124]. Even though the design domain can be widely investigated through surrogate models, limitations are still present, as the accuracy of the interpolation strongly depends on the amount of available data.

Recent works have proposed machine learning-based techniques to model the effect of the geometry of crash structures on their response: Sakaridis at al. [125] developed a machine learning passed model to predict the crash response of tubular structures using a standard NN, while Zhang et al. [126] used a clustering algorithm to identify three characteristic collapsing mode of the origami structures to correlate these with the tube geometry.

In this chapter, a PINN developed to optimize the crushing performance of an origami tube is proposed.

The origami structure here retained consists of two axially stacked basic structures, called modules, each presenting a lower and upper square section and an octagonal section in the middle and is made of two carbon fibre woven fabric plies. The PINN aims to correlate the crushing response of the single modules to that of the whole origami tube. A shape parameter of the octagonal cross section and the height of the module are varied through a morphing strategy and following a Latin Hypercube (LH) DoE scheme. Finite Element (FE) analyses of the single modules and the corresponding whole tubes are performed in the LS-Dyna environment to train the network. The FE model was at first validated by comparing numerical simulation results with the experimental results of the crushing tests on a single

module structure. The proposed scheme allows for the investigation of a large design domain with consistently reduced computational effort. The PINN is then used to optimize the crashing performance of the structure. Two optimal configurations are identified by the PINN with similar performance. The predicted absorbed energy and its trend with the proceeding of the collapse displacement are compared with FE analyses. Results show a good agreement, thus proving the effectiveness of the devised methodology. Finally, the comparison of the results obtained with a standard FFNN shows that the PINN scheme leads to more accurate results.

4.2 Materials and Finite Element Model

Firstly, the carbon fibre woven fabric used in the crash tubes is presented. Then the considered origami geometry and the adopted FE model are described. The FE model was previously validated by comparison with the experimental characterization of the crash response of the single module. Then, the shape morphing methodology adopted to generate the numerical Design of Experiments (DoE) according to a Latin Hypercube sampling scheme is presented. FE analyses are performed to train both the PINN and the FFNN. The loss functions of the two networks are finally detailed at the end of the section.

4.2.1 Materials

Carbon fibre woven fabric pre-impregnated with epoxy resin, named XPREG XC130, is considered for the origami tube. Tensile, compressive and shear properties have been assessed in a previously published work [127] through a servo-hydraulic material testing machine Instron 8801 and in accordance with the specifications of the Standards ASTM D3039, ASTM D3410 and ASTM D5379 [128–130]. Table 1 reports the mean values and the standard deviations at the lamina level resulting from three repetitions of each test.

Table 4.1. Material properties of the XPREG XC110 measured with experimental tests.

Property	**Mean Value**	**STD**
Density [kg/m^3]	1450	
In-plane Poisson’s ratio	0.12	
Longitudinal modulus [MPa]	58000	340
Transverse modulus [MPa]	58000	340
Longitudinal tensile strength [MPa]	440	16
Longitudinal tensile ultimate strain mm/mm]	0.0072	
Longitudinal compressive strength [MPa]	453	36

Longitudinal compressive ultimate strain	0.096	
Transverse tensile strength [MPa]	440	16
Transverse compressive strength [MPa]	453	36
In-plane shear modulus [MPa]	3900	
In-plane shear strength [MPa]	72	

Table 4.1 also reports the ultimate stresses and ultimate strains, necessary for the complete characterization of the material card. The lamina thickness is equal to 0.45 mm.

4.2.2 Geometry Description

The basic principle of an origami structure is to fold a flat rectangular sheet and transform it into a three-dimensional shape. Figure 4.1 shows the origami geometry considered in this study in its unfolded and folded configurations. The image reports a single module of the full crash box, i.e., the basic structure that is then axially stacked to create the full crash tube. In the unfolded configuration, the sheet presents a rectangular shape with a major edge of $8e$ in length and a height equal to l. In its folded configuration, the origami tube presents an upper and lower square perimeter with a length equal to 8e, and an octagonal central perimeter with a total length of 8b+4c. The unfolded configuration must have a rectangular shape; therefore, it holds that:

$$8b + 4c = 8e \tag{4.1}$$

The c value is the width of the rhomboidal lobe. The normal distance between the upper and the bottom rectangular perimeter (or the normal distance between the two vertexes of the rhomboidal lobe) is the height of the single module (h distance). Note that h is different from l, as in the folded configuration the origami faces are bent at an angle ϑ with respect to the plane orthogonal to the tube axis.

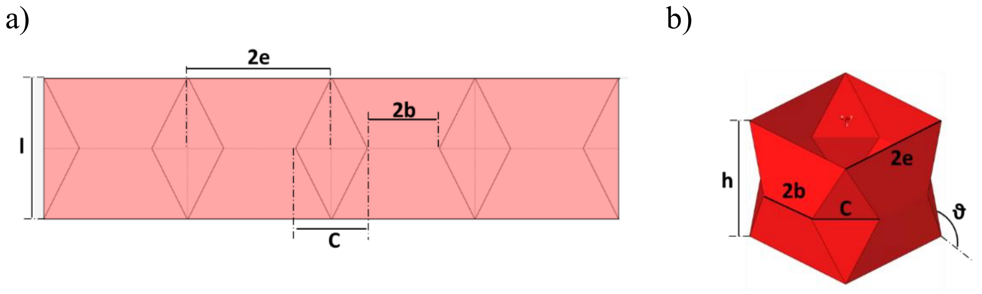

Figure 4.1. Description of the origami single module geometry: a) unfolded sheet; b) folded single module origami structure.

4.2.3 Finite Element model and experimental validation

The crushing response of the origami structure is assessed through transient nonlinear FE analyses in the LS-Dyna environment. The origami tube is modelled through Belytschko-Tsay 4-node shell elements with six degrees of freedom per node. After the convergence study [23], a mesh size of 5 mm is considered. The structure is composed of two layers of the carbon fibre woven fabric described in Section 4.2.1 and has a uniform thickness of 0.9 mm. The stacking sequence is specified through the *PART_COMPOSITE keyword, which assumes one integration point for each layer though the thickness of the laminate. The anchorage of the crash-box structure to the vehicle frame is simulated by fully constraining the bottom nodes, while a rigid wall impacts the structure with an initial kinetic energy of 1.2 kJ with an impact speed of 2.5 m/s. This energy level guarantees the complete crush of the tube. The same conditions apply to the single module and full origami structure. The material under study presents a low sensitivity to the strain rate, thus its effect has not been modelled in the FEM.

The material is modelled with the material card *MAT_ENHANCED_COMPOSITE_DAMAGE (*MAT54/55), according to the properties reported in Table 4.1. The adopted material model includes some non-physical parameters, properly conceived to improve its crash simulation capability. The non-physical SOFT parameter was identified in the previous work [127] by comparison with the compressive test of a single module. This parameter reduces the stiffness of the crush-front elements, thus simulating damage propagation and reducing the load oscillations. Figure 4.2a and b show the tested module and the corresponding FE model.

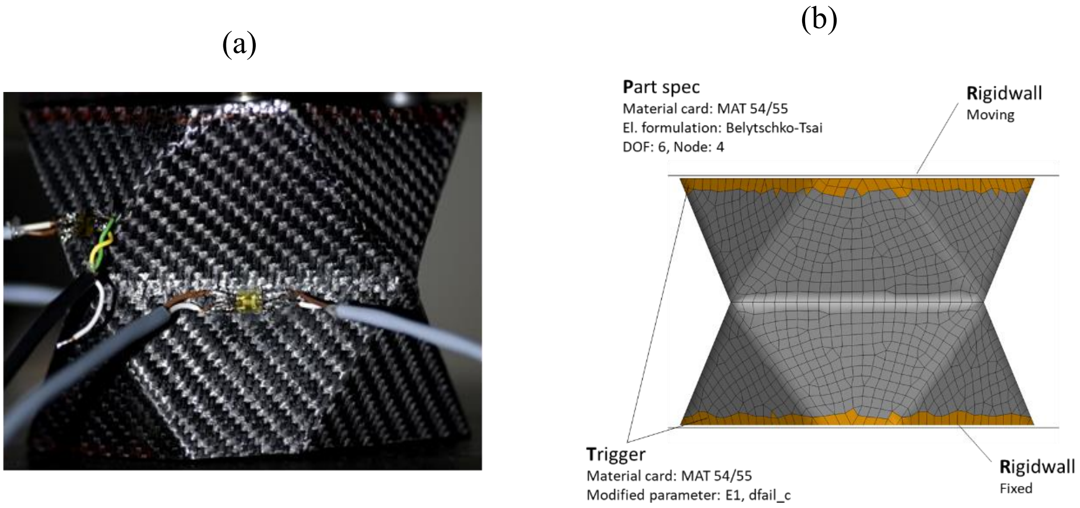

Figure 4.2. Crushing test of a single module: a) experimental setup; b) numerical model.

For further details, the reader is referred to [127].

4.3 Machine learning methods

The machine learning framework presented in this chapter aims to correlate the axial crushing response of the individual modules with the global response of the origami crash tube, obtained by vertically stacking the individual modules. This method assumes that the response of the single submodules is related to the response of the crash tube and finds a relation between those using a neural network. The framework is visually described in Figure 4.3.

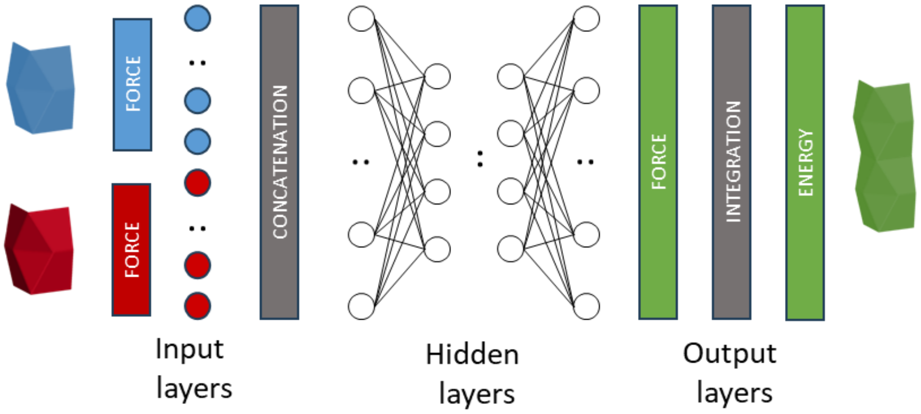

Figure 4.3. Machine learning framework for the prediction of the crash tube response from the individual crash of the sub-modules

The dataset generation, feature extraction, data preparation and the neural network used in this work are described in the following subsections.

4.3.1 Design of experiments (DoE)

A set of numerical simulations of axial crashing of a single module structure with different lobe widths and heights (respectively named c and h, Figure 4.1) is performed. The absorbed energy and force response are stored in a database and used to train the machine learning algorithms. The design space of the single modulus geometry is described by the two variables, i.e., c and h, sampled within a range from 35 to 55 mm and 78 to 98 mm, respectively. A Latin Hypercube (LH) algorithm is used to sample 40 points in the defined design space, yielding 40 different single-module geometries.

The DoE exploration is carried out by interfacing the geometric pre-processor Hypermorph with the software LS-Opt. The parameterization of the shape variables c and h is carried out through the Hypermorph software.

The parameters are passed to a morphing script that modifies the single modulus mesh by preserving:

- Planarity of the crash tube edges,

- The total area of the mid-surface, complying with the definition of an origami-inspired thin-walled structure,
- The total number of mesh elements.

As the origami crash tube presents two cross-sectional symmetry planes, only a quarter of the module is modelled (Figure 4.4a).

The different geometry shapes are generated without a remeshing algorithm: the morphing of the structure deforms and stretches the mesh elements to an acceptable extent and without worsening the mesh quality indices. The generation of the morphed shapes is divided into two steps: morphing of the module height *h* and morphing of the lobe width *c*.

The *x, y,* and *z* degrees of freedom (DOF) of the nodes belonging to the edge *e* are constrained to node 1 (Figure 4.4).

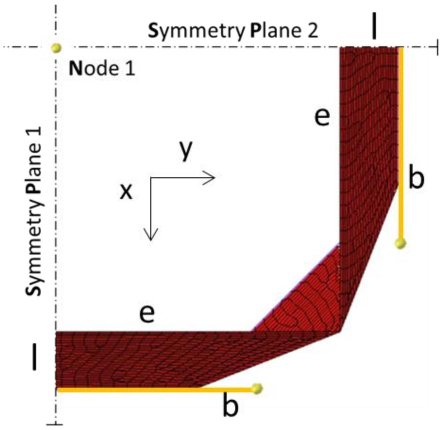

a)

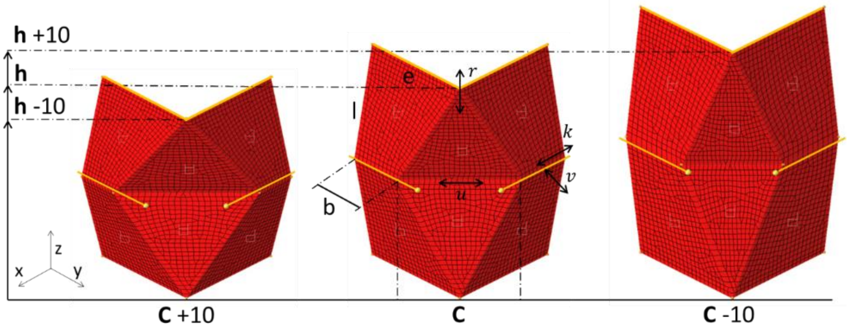

b)

Figure 4.4. Module geometry and morphing procedure description: a) a quarter of the origami module with symmetry planes evidenced (x-y view); b) baseline module and morphed configurations (iso view), after both c and h value modification.

Accordingly, when node 1 is moved along the z direction, the module is morphed in its height. A plane passing through the *b* edge and parallel to the *xy* plane is created to guarantee a symmetric morphing relation and equally stretches the two-half portions of the module. As the morphing of the structure requires preserving the planarity of the crash box edges (i.e., equation 4.1 must hold), the variation of the *c* parameter requires particular attention. The translational DOFs along the *x* and *y* directions of the nodes belonging respectively to the right and left vertical free edges (edges l in Figure 4.4b) are constrained. Consequently, the *b* edges can only rigidly translate orthogonally to their direction, i.e., along the *v* arrow in Figure 4.4b. The nodes of edge *b* are constrained to move only along the *k* direction. Accordingly, when the *c* value is increased, the *c* edge nodes move in the *u* direction, and the *b* edge elements shorten along *k.* Also*,* the *b* edges move along *v,* and the angle between the module faces decreases. Figure 4.4b shows two examples of geometrical morphing applied to the origami module. As can be noticed from the configuration C-10/h+10, as the *c* value decreases, the angle between the faces increases. Ideally, if *c* is reduced to 0, the origami module morphs into a square-section parallelepiped.

Once the input database is defined, the 1560 possible double module geometries given by the combination of the single modules combinations are computed and a subset of 100 configurations is sampled (shown in Figure 4.5). These 100 double module configurations have been sampled through a discrete LH algorithm, constrained to sample discrete points in the design space (i.e., the possible combinations), later simulated with *LS-Dyna*.

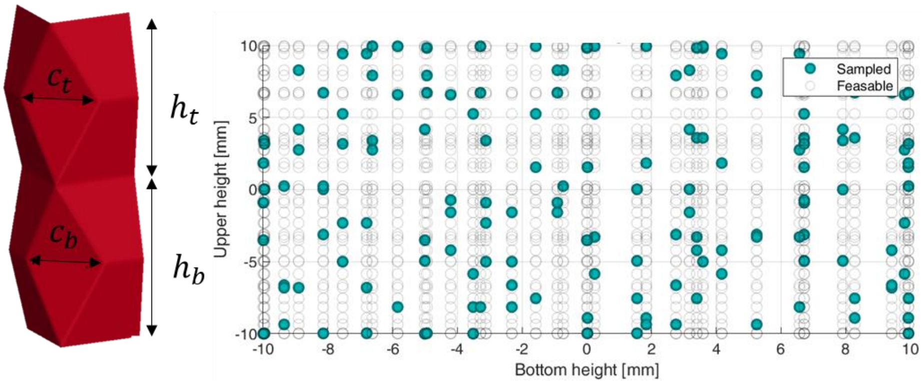

Figure 4.5. Discrete LH sampling of double module geometric feature

As described for the single modules, a double module Finite Element mesh is morphed following the same procedure. The double module configuration presents 4 geometrical variables: two for the bottom module (c_b and h_b) and two for the top module (c_t and h_t). The energy and force results of the crushing simulations are stored in an output database and later used to train the machine learning algorithms.

4.3.2 Mechanistic feature extraction

To enhance the performance of the machine learning algorithm for the prediction of the mechanical response of structures, it is crucial to properly pre-process the data and extract the most relevant features influencing the final response.

Specifically, two critical aspects should be accounted for:

- most machine learning algorithms take as input fixed shape variables, while the crushing response of the origami structures varies with the total height of the crushed tube,
- the arrangement of single-module responses into a single input vector should reflect the observed interaction of modules during the multi-module structure crush.

To get a coherent amount of data in each curve, the displacement vectors are normalized to their maximum value and N linearly spaced points are sampled. Following this procedure, every input simulation is described by two vectors (i.e., force and energy) with shape Nx1. Accordingly, the curves of the two single modules composing the bi-module crash tube have been concatenated into 2Nx1 vectors, following the bi-normalization transformation in Equation 4.2.

$$d_{norm} = \begin{cases} \dfrac{d}{h_{top}} & if\ d < h_{top} \\ 1 + \dfrac{d - h_{top}}{h_{bot}} & if\ d > h_{top} \end{cases} \tag{4.2}$$

Being the pre-processing steps defined, the neural network should map the single module responses, with dimension Nx1 each, into a double-module response of dimension 2Nx1. To build the input vector, the single module responses are concatenated to:

- fix the transition point from the top to the bottom module,
- reflect the mechanical behaviour of assembled structures, where the crushing takes place gradually, starting from the failure of the top module followed by the crush of the bottom sub-structure.

The resultant curve obtained with the described method is shown in Figure 4.6.

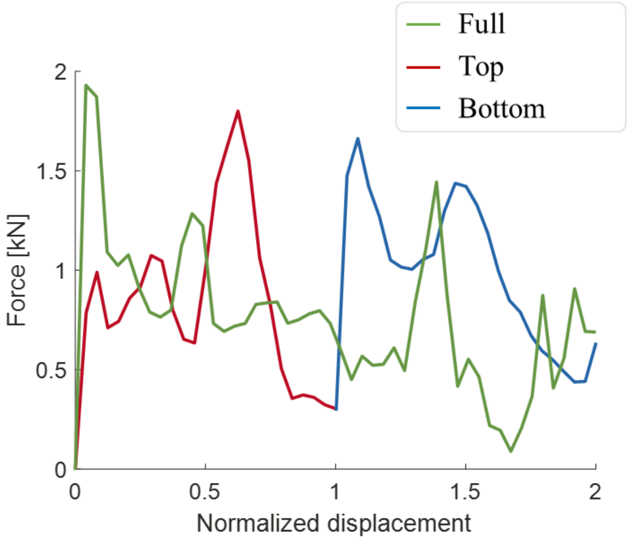

Figure 4.6. In green, the output curve is computed from the crashing response of the assembled structures. In red and blue, the curves obtained from the crashing of the single modules elaborated to feed the NN.

4.3.3 Feed-Forward Neural Network (FFNN)

A standard FFNN is trained on the generated data using a stochastic gradient descent method [20] and the trainable parameters are upgraded with a back-propagation procedure, to minimize the defined loss function. The backpropagation is perpetuated iteratively in each epoch over a subset of data defined as a batch; the number of training epochs is automatically defined by a stopping rule (i.e., early stopping). The loss function for the regression task is defined as the mean square error (MSE) in Equation 4.4.

$$MSE = \frac{\sum_i^{N_b} (\bar{y}_i - y_i)^2}{N_b} \tag{4.4}$$

where N_b is the batch size, $\bar{y}$ the true output and y the prediction. Further details on FFNN are given in Chapter 1.

4.3.4 Physic-informed Neural Network

The method that was originally proposed uses a PINN architecture tailored for the prediction of the axial crash response of assembled structures by embedding the equilibrium equation and energy conservation principles in the training stage. The proposed architecture, shown in Figure 4.3, is composed by:

1. a pre-processing block performing a bi-normalization of the substructure crash response,
2. a force prediction branch entitled to predict the force response of the assembled structure from the force response of substructures,
3. a physics layer assessing the energy balance error by computing the energy, i.e., the integral of the predicted force over displacement (Eq. 4.5):

$$E_{comp} = \int_0^{h_i} F(x)dx \qquad (4.5).$$

The model is trained with a regularised loss function $\mathcal{L}$ penalizing a non-monotone energy prediction, ensuring the energy conservation criteria are satisfied, as described by Eq. 4.6.

$$\begin{aligned}\mathcal{L} = {} & \frac{1}{N}\sum\left(\boldsymbol{F}_i^{pred} - \boldsymbol{F}_i^{true}\right)^2 + \\ & \alpha \cdot \sum\left(\int_0^{h_i} \boldsymbol{F}dx - \boldsymbol{E}_i\right) - \boldsymbol{\beta} \cdot \frac{\sum_i \ll \boldsymbol{E}_{i+1} - \boldsymbol{E}_i \gg}{\boldsymbol{N}},\end{aligned} \qquad (4.6)$$

where F_i^{true} and F_i^{pred} are the FEM computed and PINN predicted values of the crashing force at the ith frame, being N the total number of frames; h_i is the crashing displacement at the ith frame and E_i the computed energy.

The first term of Eq. 4.6 penalises the prediction errors on the force, while the other terms penalise the physical inconsistency of the predictions. The parameters α and β are non-negative scalars that weigh the influence of the physics-related terms on the total loss, scaling it to the same order of magnitude as the other contributions. In the last term of Eq. 4.6, the operator <<·>> gives one if the argument is positive and zero otherwise, penalizing the predictions with a decreasing trend of the absorbed energy.

4.4 Results

In this section, the results of the surrogate modelling approach for the design of the origami crash tube are presented. First, the FFNN and PINN are trained on the available results of FEA, then the crash response predicted with the NN models is compared with the reference curves from the FEM to assess the accuracy of the method and compare the FFNN with the PINN. Finally, the PINN is used to optimize the geometry of the origami tube and the prediction of the response of the optimized geometries is validated with the FE model.

4.4.1 Double module crash prediction: comparing FFNN and PINN

The architecture of the FFNN has been optimized based on the sensitivity analysis carried out on the model accuracy: the number of layers and the number of neurons per layer have been varied to identify the best architecture to be used. Figure 4.7 reports the value of the loss function after 500 epochs for different architectures: Figure 4.7b indicates that deep networks lead to low accuracy due to the increase of the network hyperparameters that compromise the convergence of the training; Figure 4.7a shows a small increase in the loss with the increasing width of the network. As a conclusion of this analysis, short and narrow architecture is suggested.

a)

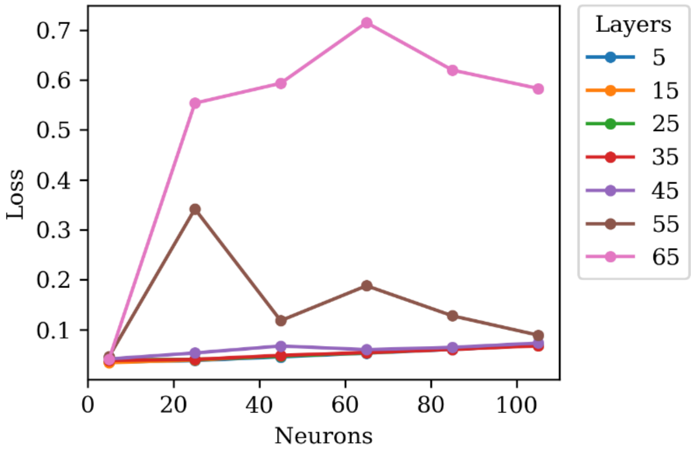

b)

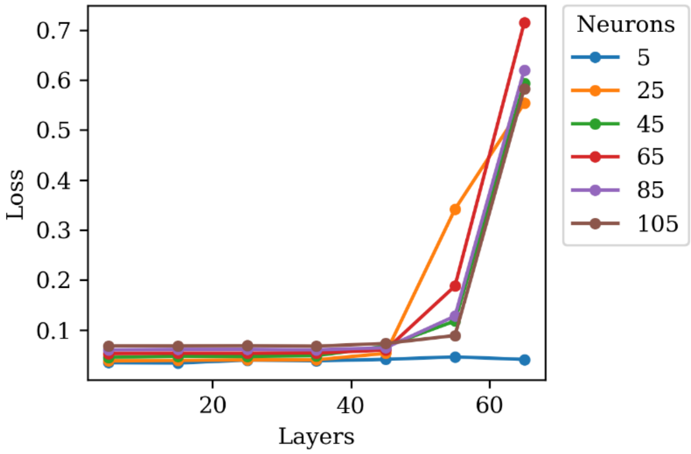

Figure 4.7. The value of the loss function at the end of the training of the FFNN with different numbers of neurons per layer (a) and number of layers (b).

On the base of the results of the sensitivity analysis, the FFNN architecture is made of 5 stacked layers with 15 neurons each. Further performed analysis suggested that the network accuracy is independent of the activation function used in the hidden layers for the case of ReLU, SELU and tanh, leading to the adoption of the ReLU due to its higher computational efficiency. The same architecture has been used for the PINN.

The activation function of the input and output layers is linear so that the output of the last layer is not biased by the activation function. The layered architecture of the FFNN is summarized in Table 4.2.

Table 4.2. Summary of FFNN optimized structures with activation function and number of neurons of each layer

Layer	Neurons	Activation function	Output shape
Input	2N	Linear	(2N, 1)
Dense 1	15	ReLU	(20, 1)
Dense 2	15	ReLU	(20, 1)
Dense 3	15	ReLU	(20, 1)
Dense 4	15	ReLU	(20, 1)
Dense 5	15	ReLU	(20, 1)
Output	2N	Linear	(2N, 1)

The FFNN was trained with 80% of the available data, while the remaining 20% was used as a validation dataset to check the eventual overfitting of training data. The neural network weights and bias were updated through a back-propagation algorithm by minimizing the Mean Square Error loss function of Eq. 4.4. The adaptive moment estimation optimizer algorithm Adam[20] has been adopted.

As previously described, the PINN takes as input the force response, the energy response, and the original displacement vector before normalization, which is used to compute absorbed energy from the predicted force. The displacement is not computed by a trainable layer and thus does not increase the number of hyperparameters of the neural network.

The values of the loss terms for the FFNN and PINN are compared in Figure 4.8. The FFNN archives smaller overall errors in the prediction of the force response while struggling to converge to an accurate prediction of the energy. As a result, the FFNN shows a 10% lower RMSE for the force, while the PINN performs better in the prediction of the absorbed energy with an approximately 70% lower RMSE.

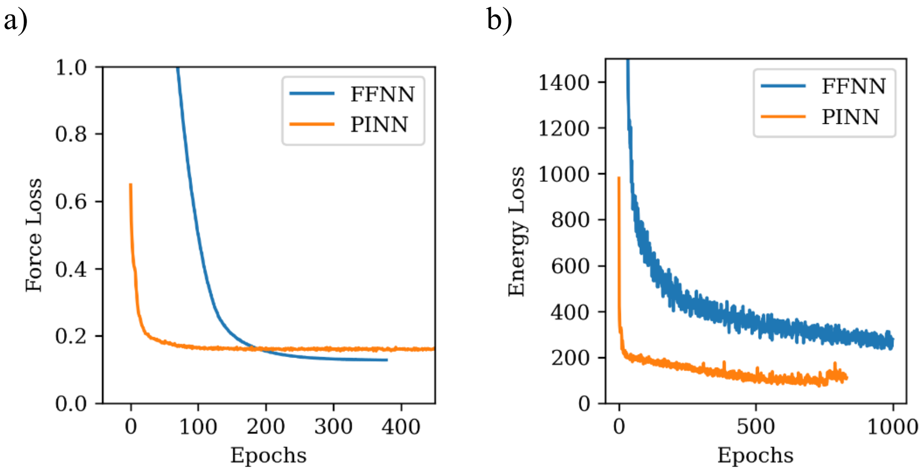

Figure 4.8. The loss values for the predicted force (a) and absorbed energy (b) during the training of the FFNN and PINN.

The training curve of the PINN is reported in Figure 4.9, to highlight the simultaneous convergence of the prediction towards accurate and yet physically compliant curves. Indeed, the values of the loss term associated with the PINN accuracy in predicting the force response are correlated with the loss curve of the energy balance term confirming that the interplay of such terms improves the training of the network.

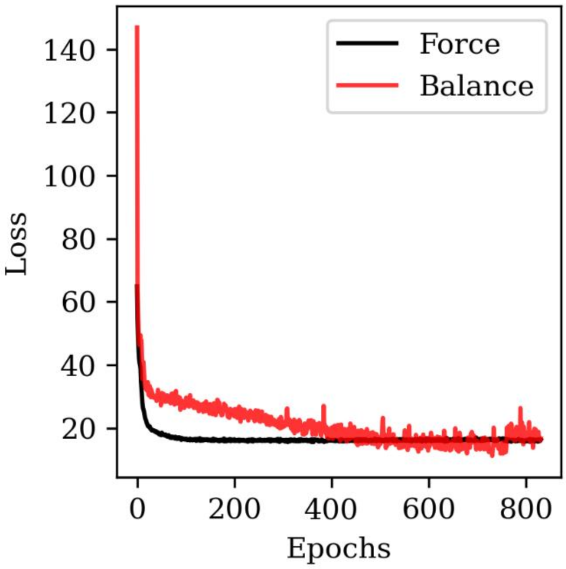

Figure 4.9. The values of the force and balance terms in the loss function of the PINN during the training.

The coupling of the force and energy prediction in the PINN limits the solution space of the Networks that reflects in higher RMSE for the force prediction but yields physic-compliant energy response. However, even if the values of the loss functions give an overall indication of the accuracy of the method, in the case of complex datasets with high variability, lower RMSE could be consequent to an input-insensitive network that outputs an average value regardless of the input data. Indeed, in the FFNN, the predicted force response is insensitive to the input configurations, while this is prevented in PINN by coupling the energy and force response with the physic layer, as shown in Figure 4.10.

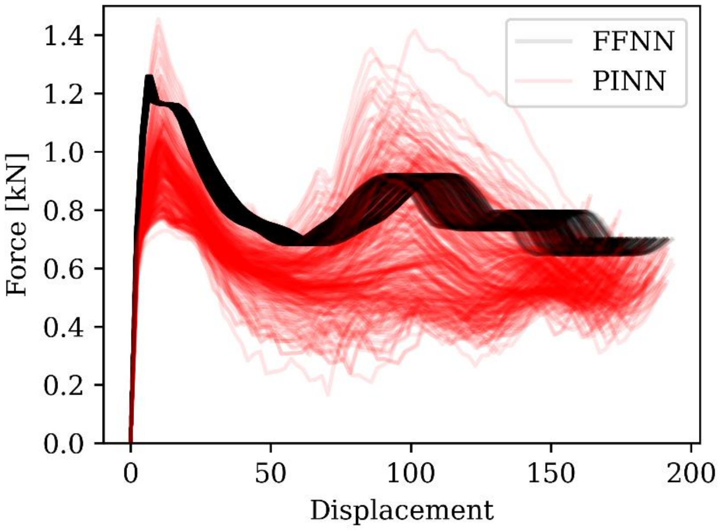

Figure 4.10. The force response predicted with the FFNN and the PINN for all the crash box configurations in the training dataset.

The curves precited with the FFNN and PINN for all the crashbox configurations in the training dataset are compared in Figure 4.10. The high variability of the force curves predicted by the PINN is in line with what was observed from the FEM in [127], while the FFNN predicts the same curve for every configuration (scaled back to the original displacement in the figure), being insensitive to the crashbox geometry and ultimately losing any predictive capability.

This confirms that the analysis of the results of ML methods applied to engineering problems should not be limited to the prediction errors described by the common data science metrics (e.g., MSE, RMSE, ...), but an extended analysis is needed to assess the usability of such methods for engineering problems.

Figure 4.10 highlights that the response of the assembled crashbox in the initial stage of the crashing has a defined trend, with a first peak and a following valley, whose values are mostly influenced by the top module geometry. While the force curve in the second stage of the crash, after the first module is completely crashed and the load is transferred to the lower part of the origami tube, has a variable trend governed by self-contact and complex failure phenomena leading to different average force and absorbed energies.

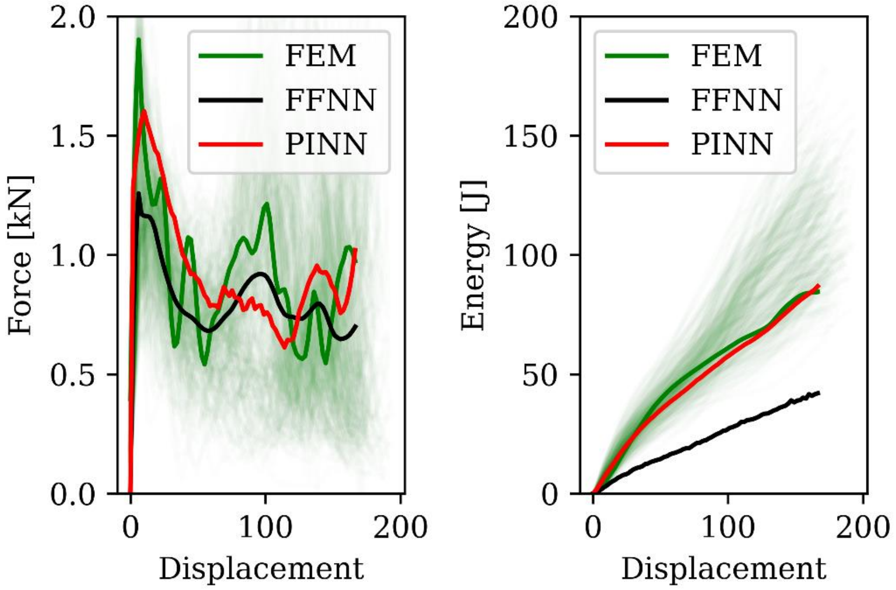

Figure 4.11. The force (a) and absorbed energy (b) predictions of the PINN and FFNN on a validation combination excluded from the training dataset (shaded curves) compared with FEM simulation (solid curve). The origami crash box has h_{bot} = 78.5, h_{top} = 84.5, c_{bot} = 47, c_{top} = 38.5.

Figure 4.11 reports the crushing response of an origami crash tube with lobe widths equal to 47 mm and 38 mm and a height of 78.5 mm and 84.5 mm, for the bottom and top modules, respectively. The result of the FEM model is compared with the prediction of the PINN and FFNN, both in terms of force and absorbed energy. The diagram of Figure 4.11a shows that in this specific case, the PINN model can predict the crush response with a 15% error on the peak load and an 8% error on the average force, while the FFNN shows a 34% error on the peak force and 7% error on the average. However, the FFNN is constant throughout the dataset, making its predictions ineffective for the design of the crashbox.

The diagram of Figure 4.11b provides evidence that the values of the absorbed energy during the crash stroke predicted by the PINN model are very close to those resulting from the FE simulation, while those predicted by the FFNN model are largely below those resulting from the FE simulation. Therefore, it can be concluded that the proposed PINN method is preferable to the FFNN, at least for this type of analysis.

a)

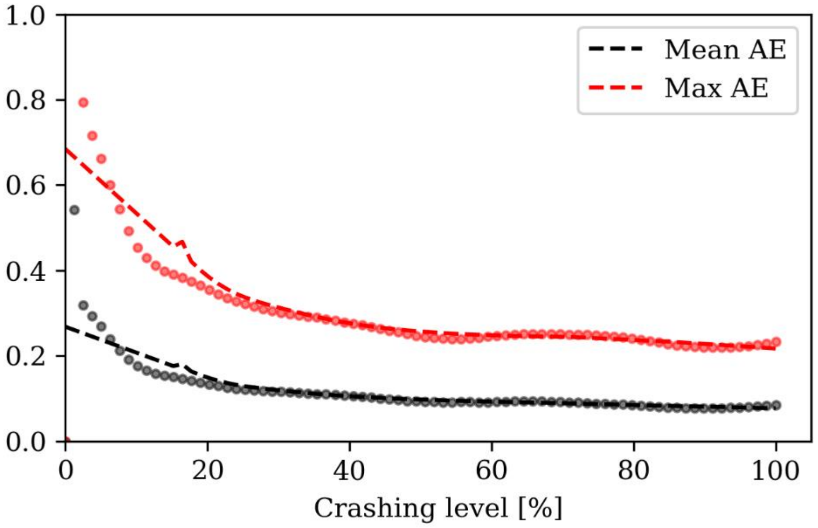

b)

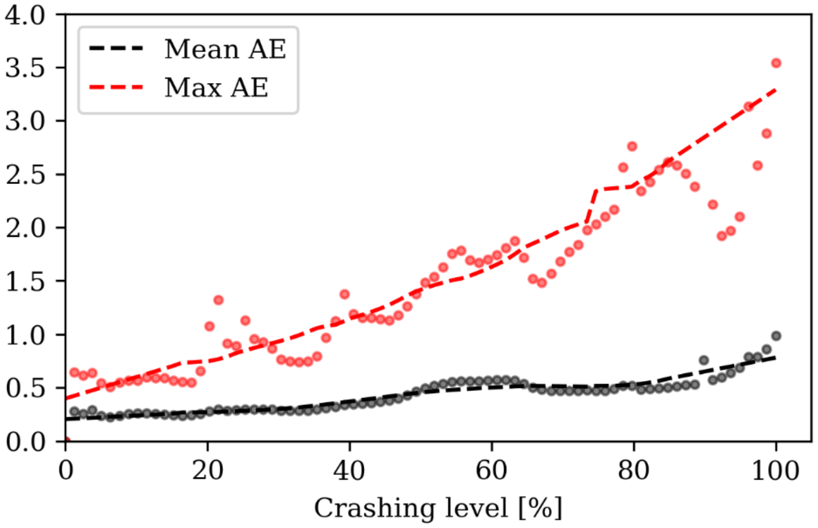

Figure 4.12. The mean and maximum Absolute Error (AE) of the PINN predictions for the absorbed energy (a) and force (b) predictions at different levels of crashing. Each point is the average of all the training errors, while the dashed lines represent an interpolation of the points.

Figure 4.12 analyses the results of the PINN at different crushing stages compared with the reference values from the FEM. It can be observed that the predicted energy has a larger error in the first stage of the crashing, due to the struggling of the model in accurately predicting the first peak force, while it converges around an average value of 0.1 after that 20% of the origami crashbox is crashed. On the other hand, it should be noted that the FE predicted value of the force at the collapse initialization (first peak) has high uncertainty and suffers the larger oscillation of the FEM results that are overall smoothed and averaged by the PINN that predicts smoother curves, resulting in larger errors in with the increasing crushing. However, the average error is almost constant toward the crashing, with higher values (between 0.2 and 0.3) in correspondence to the crashing of the second modulus where non-linear and history-dependent phenomena take place and negatively affect the predictive capability of the model.

4.4.2 Optimization of the origami tube with the PINN

The PINN model is used to optimize the geometry of the origami-shaped crash box by initially simulating 40 single modules (N=40) with different geometry. The full domain that the PINN can explore counts 1560 different configurations that can be predicted with the proposed algorithm. The energy response results are reported in Figure 4.13: the rapid exploration of the extended DoE confirms that the variation of origami geometry, even not affecting the total mass of the component, leads to a significant variation in the absorbed energy as observed in [127]. All the possible configurations of the 40 modules have been predicted with the PINN and are reported in Figure 4.13.

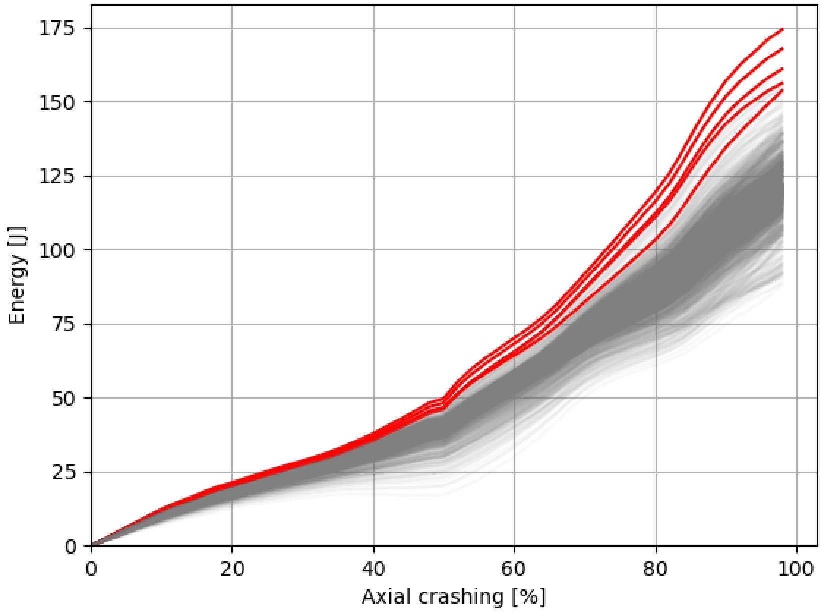

Figure 4.13. Machine learning predictions of 1560 different geometric configurations of a double module origami-inspired crash box, in red the five curves with the highest absorbed energy.

Figure 4.12 shows that the accuracy of the PINN in predicting the energy values varies within different crashing intervals, with more accurate prediction in the initial region, gradually decreasing until the complete crashing where a high non-linear failure mechanism combines. Considering this, a scoring method is introduced to evaluate the best curves by ranking all predicted responses at different intervals and assigning a score (5 to the best prediction and 0 to the worst prediction) to the best five predictions at each crashing level (Figure 4.14)

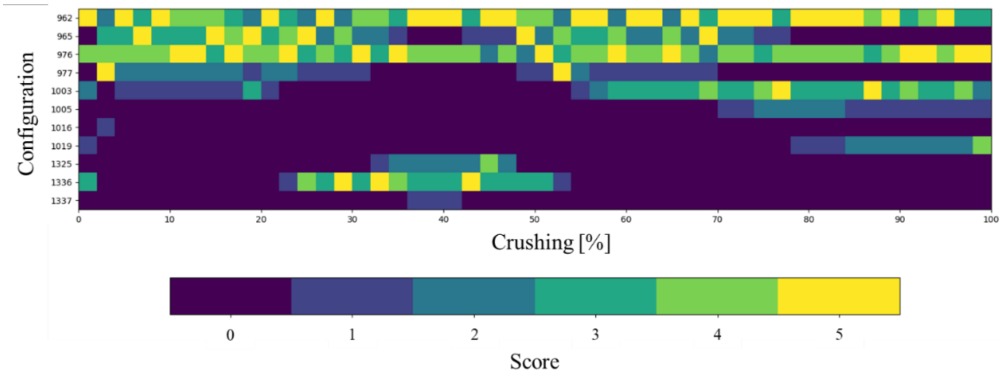

Figure 4.14. Scoring algorithm ranking a selection of the best different configurations at each crashing level by the normalized absorbed energy. Scores from 1 to 5 are assigned at each interval.

The proposed scoring strategy counters the accuracy decrease in the prediction of the absorbed energy close to the complete crushing, rewarding the crash tubes that show a consistently higher performance among all the configurations. Indeed, Figure 4.15 shows the normalized energy absorption of all predicted configurations at 40%, 70% and 90% of ultimate displacement, evidencing the existence of temporary peaks vanishing outside certain intervals. This is in line with the energy curves shown in Figure 4.13, where a small difference in the absorbed energy is evidenced for the first phase of the crashing where the curves are grouped. With the increasing displacement, the absorbed energy of the different origami tubes diverges from the average values, yielding the presence of optimal configurations with higher energy absorption capability. These reflect the yellow spots in the response map at 90% of the crashing in Figure 4.15.

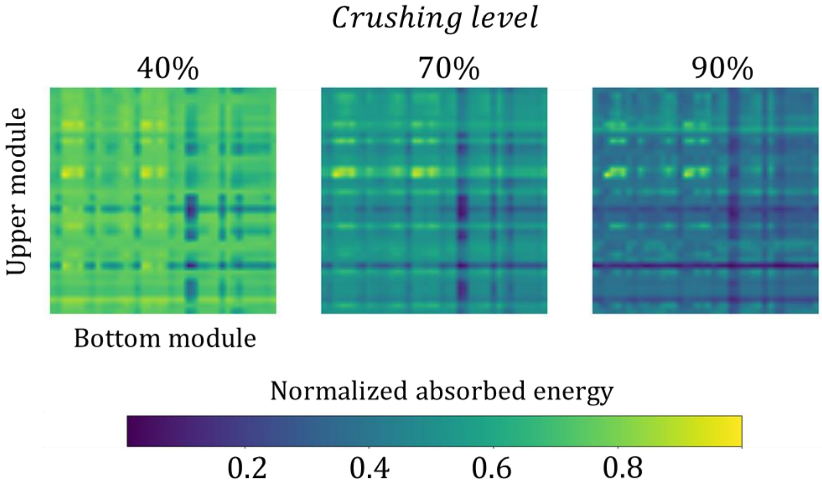

Figure 4.15. Heatmap of the normalized absorbed energy at 40%, 70% and 90% crashing intervals.

The best two configurations show (see Figure 4.14) absorbed energy of 175J and 171J, respectively, with their geometrical features reported in Table 4.3

Table 4.3. Geometrical features of the two configurations with the highest absorbed energy predicted by the PINN.

	c_bot [mm]	**c_top [mm]**	**h_bot [mm]**	**h_top [mm]**	**E [J]**
1	42.2	54.5	93.25	81.4	175
2	42.2	41.2	63.2	79.8	171

The crash response for these origami tubes is then computed using the FE model and the results are compared in terms of absorbed energy, to confirm the quality of the results and the efficiency of the machine learning-based optimization algorithm.

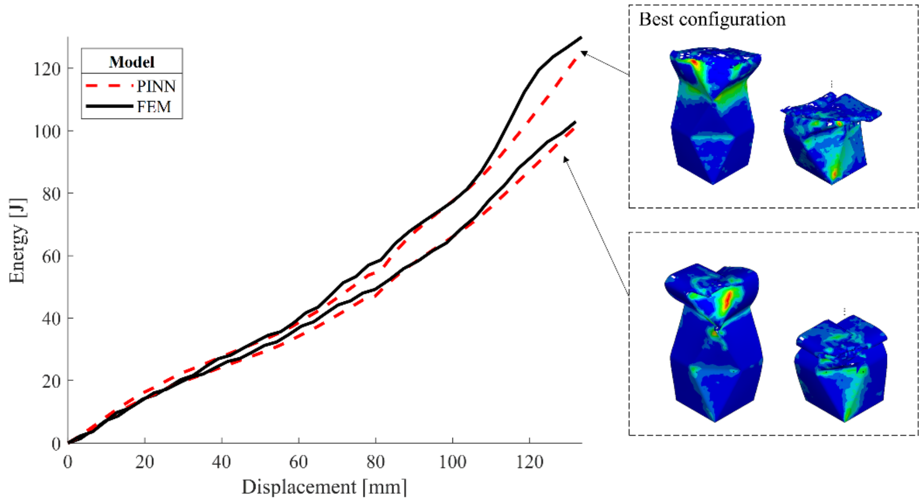

Figure 4.16. The absorbed crash energy of the optimized configurations predicted with the PINN model compared with the results of the FEM

The comparison is reported in Figure 4.16 and shows a good agreement between the response predicted by the PINN algorithm and that calculated through the FE analysis up to 80% of the total crashing. This proves that the proposed methodology can be reliably applied to the design of the origami tube and guarantees a remarkable reduction of the computational effort.

The presented PINN algorithm can predict the crashing response of the assembled structures with reduced computational efforts and an overall good accuracy; more specifically, given a set of N single module crash simulations, the algorithm can estimate the response of N!/(N-2)! geometric configurations of the double modules crash box by drastically reducing the computational cost. Indeed, once the model is trained, the assessment of the full crashbox response computed with the PINN takes approximately 0.1 seconds on a 16-CPU laptop, while an FEA of a crashbox with two modules takes around 35 minutes on a 40-CPU cluster. Figure 4.17 shows the computational saving in terms of simulation hours for different N, showing an average speed up of 30 times.

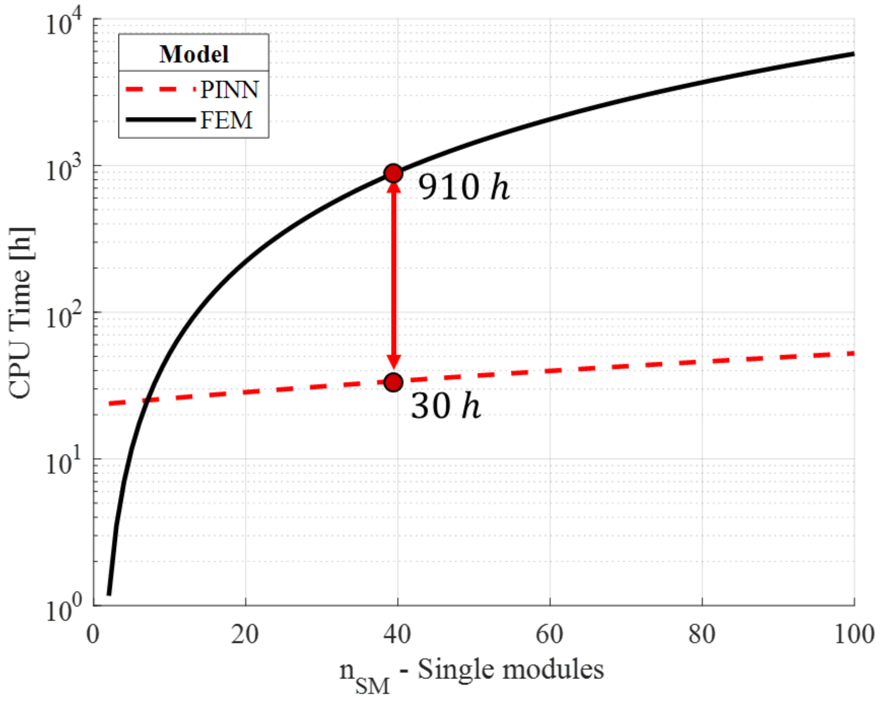

Figure 4.17. Computational time comparison between FEM and ANN optimization

4.5 Conclusions

In this Chapter, an MDS method to surrogate the FEA of origami-shaped composite tubes has been presented to reduce the computational cost of the crashing simulations and accelerate the exploration of the design space with overall good accuracy. The method demonstrates that with an experimentally calibrated FEM in the hands, a reliable database of structural responses can be generated to train a surrogate PINN that can further explore the design space learning from the FE results and rapidly predict the response of new structures. The importance of extracting the mechanistic information from the available data has been discussed and the efficiency in blending the physical knowledge with the predictive capability of NN has been demonstrated. Indeed, the MDS method showed a higher predictive capability of the standard NN that reflects the accuracy and reliability of the network. The proposed method has been used to optimize the geometry of the origami-shaped composite tubes under axial crashing and, after having optimized the structure, to achieve the maximum absorbed energy with a speed up of 30x, if compared to a FEA-driven optimization with a full exploration of the design space.

The proposed method is still limited by the analysed geometry, and it is expected to have lower performance if used to predict the response of composite tubes with different geometries of the modules. To have a more generic surrogate model different algorithms should be explored that can handle the structure geometry as input parameters, for example, the Graph-based NN (GNN) and the Geodesic Convolutional NN (GCNN) could be considered. Recent works [42,44,131] have demonstrated the applicability of this architecture to surrogate numerical models operating on mesh structures, opening the door for a geometry-independent surrogate model of the FEA.

5 Data driven method for the prediction of the fatigue response of additively manufactured parts from the process parameters

5.1 Introduction

In the previous Chapters, three different MDS methods have been introduced to model the structure-to-property relationship, assessing the material properties (Chapters 2 and 3) and the structural response (Chapter 4) of composite by leveraging on the availability of experimental data or FEM-generated data, respectively. Recalling the PSP paradigm of integrated computational materials engineering (ICME), a strong link exists between the process (i.e., the manufacturing) and the structure of materials, which eventually affects the mechanical properties. Therefore, modelling the process-to-structure link is of fundamental importance to effectively predict the mechanical properties of advanced materials which exhibit a variable microstructure (e.g., defects, fibre orientation in FRP, inclusion in metals, ...). Computational tools that predict the formation of defects and manufacturing-induced variation of the microstructure can be coupled with the mechanical models to cover the full PSP relationship in the modelling environment, but these usually require multi-disciplinary knowledge, extensive experimental campaigns to achieve an efficient calibration of the material models and a costly set of simulation suites. However, ML models have opened the door for a direct, easy-to-implement and data-driven solution to link the manufacturing process to the microstructural variations that eventually affect the mechanical response.

5.1.1 Fatigue Strength in Additive Manufacturing

The assessment of the manufacturing-induced defects is of paramount importance for predicting the fatigue strength of parts produced via Additive Manufacturing (AM). Although the strength and stiffness of metal structures produced with AM have been proven to be comparable, or even superior, to that of traditionally manufactured counterparts, the performance of AM components under cyclic loads is generally lower [132–135]. This discrepancy primarily arises from manufacturing defects, such as pores or lack of fusion defects [133,135–137], that inevitably originate during the manufacturing process. These defects serve as critical sites for crack nucleation.

Current research efforts are focused on identifying optimal process parameters that can minimize critical defects in AM parts. This strategy has been proven effective in enhancing the fatigue resistance of AM parts [132]. However, even if the combination of process parameters that minimize defect density is achieved, there is still a possibility of rare and significant defects forming in the final part. Consequently, ensuring the structural integrity of AM components under fatigue conditions requires considering the inherent defectiveness of the material during the design process and accounting for the impact of defects on fatigue response.

5.1.2 Design strategies to address the effect of defects

Various strategies can be employed to achieve this objective. For instance, performing a micro-CT scan of the part can provide comprehensive information regarding the material's defectiveness. Designing the part reliably can be accomplished by utilizing established literature models that assess fatigue strength in the presence of defects [138–140], such as the Murakami model [141] or the El Haddad model [142]. These literature approaches allow to model the dependency of the fatigue strength on the defect size distribution. However, these models do not establish a correlation between the estimated fatigue strength and the primary manufacturing process parameters, which primarily govern material defectiveness and, consequently, fatigue response. Therefore, the structural integrity of the part can only be verified after the production of the component or if the distribution of defect sizes is known in advance.

Nonetheless, critical manufacturing process parameters, such as beam diameter, beam power, layer thickness, powder size, and post-treatments (e.g., heat treatments), significantly affect the fatigue response [143]. Thus, they should be considered during the design phase. Neglecting their influence would render the design ineffective and less efficient since the defect population and final microstructure are influenced by the parameters. Therefore, an ideal approach would involve establishing a correlation between fatigue strength, the stress-life relationship, and the process parameters as well as the post-treatment. This correlation would provide a reliable assessment of the structural integrity of AM parts under fatigue conditions.

5.1.3 The influence of process parameters on the fatigue response

According to the literature [143–145], one of the main reasons for the variability of the fatigue strength of AM parts is associated with the large number of process parameters that differently affect the defect population and, consequently, the fatigue strength. Therefore, it is rather difficult to define a simple model that allows estimating and predicting the fatigue strength from the process parameters. For example, the effect of a specific parameter can be estimated with an appropriate experimental plan, like what is done in [143,146]. However, the main drawback associated with these approaches is that the interactions between the manufacturing process parameters can be only accounted for with extensive and, thus, unaffordable experimental plans.

ML algorithms are ideal candidates to understand the effect of process parameters, and their interaction, on the fatigue response of AM parts. In the literature, ML algorithms have been used for assessing the structural integrity of AM components. Zahan and Li [147] introduced a machine learning methodology trained on artificial data to assess the fatigue limit of AM Ti6Al4V and SS316L alloys. The effect of process parameters is embedded in the computational approach used to generate data, accounting for hatch spacing, speed, layer thickness and powder size. Maleki et al. [148] have studied the efficiency of both shallow and deep neural networks in predicting the effect of thermal and shot peening post-treatment on the fatigue life of AM AlSi10Mg parts. The models are trained on experimental data of notched specimens manufactured with a specific combination of printing parameters, thus not accounting for their effect on the fatigue response. Results show a 99% accuracy of deep learning autoencoders in predicting the post-processing effect on fatigue life, outlining the promising capabilities of ML for the prediction of the fatigue response of AM parts. Chen and Liu [149] recently proposed a probabilistic physics-guided model predicting the S-N curve of AM Ti6Al4V produced with Selective Laser Melting (SLM) from manufacturing parameters. Authors gained accuracy and efficiency by imposing soft constraints on the S-N curve trend, e.g., monotonicity, slope decreasing with the number of cycles at failure. [150] proposes an ML method to investigate the synergic influence of defect size, depth, location and building orientation on Ti-6Al-4V, achieving an accuracy of 98% in the prediction.

The main contributions of the referenced literature are reported in Table 5.1.

Table 5.1. Literature on fatigue response of AM

Reference	**F**ocus
[132-135]	Fatigue response of AM components and manufacturing defects.
[135-137]	Manufacturing defect of AMed metals.
[138-142]	Literature models for fatigue strength assessment in the presence of defects.
[143-146]	Effect of AM parameters on the fatigue response.
[147-150]	ML methods for assessing the fatigue response in Ame alloys.

Here, two ML algorithms have been designed to predict the S-N relationship of AM parts starting from the SLM process parameters (i.e., layer thickness, beam diameter, hatch distance, energy density, building orientation, and power) and heat treatment properties (i.e., heating temperature and duration), as described in [151].

The two models trained and tested to fulfil the objective, are a FFNN and a PINN model. The first is a standard FFNN that predicts the stress amplitude from the process parameters and the number of cycles that the part should withstand. This algorithm operates as a black box that approximates the relationship between process parameters with the S-N response of observed data. The second one is based on the experimental evidence that process parameters mainly affect the size of defects and the microstructure, whereas the heat treatment properties have a main influence on the resulting microstructure, thus differently affecting the fatigue response. To infuse the empirical knowledge into the network architecture, a novel modular architecture is introduced, where the input parameters are arranged to feed separate neural network branches, respectively accounting for defect and microstructure effects on fatigue life prediction. On the output side, the network modules are merged within a physics layer mimicking the Murakami equation [141]. The proposed hybrid data-driven and phenomenological model is novel and aims at preserving the mechanistic knowledge of fatigue modelling while leveraging the ability of machine learning methods to learn from the available data. The model architecture replicates the process-structure-property paradigm to get an insight into the mechanistic relationship that links the process with the fatigue properties.

Both models are trained and validated on experimental datasets taken from the literature obtained by testing AlSi10Mg alloy specimens. The advantages and the limitations of the two ML algorithms are highlighted and their capability of properly modelling the fatigue response and the influence of specific process parameters on the fatigue response is discussed.

5.2 Methods

5.2.1 Data driven framework

The fatigue response of materials in its simplest form is expressed as the relation between the applied stress amplitude (s) and the number of cycles to failure (N). Due to the stochastic nature of the fatigue phenomenon, the stress-life relationship is assessed through rather expensive and time-consuming experimental tests, to properly model the intrinsic scatter.

The fatigue response of AM parts is governed by defects [152], that are in turn related to the process parameters. These pones the challenge of defining the influence of the SLM process on the material strength under cyclic loads. First, the main parameters affecting the defect population, the microstructure, and, consequently, the fatigue response [153] are identified:

- Building orientation (α): has a relevant effect on the defect size and, accordingly, on the fatigue response [154,155].

- Input power (P) and scan speed (v): these two parameters can be condensed in the energy per unit length parameter, which should be appropriately selected, to avoid the formation of lack of fusion defects due to the insufficient power per unit length [156].
- Hatch distance (h): influences the defect size and the fatigue response, with the fatigue response improving as the hatch distance is reduced [157,158]. According to [159], a larger hatch spacing introduces larger pores and hence degrades fatigue life.
- Layer thickness (t): larger values induce higher porosity that eventually influences the fatigue response [153,160].
- Heating platform temperature (T_p): is proven to affect the fatigue response of different AM materials, like AlSi10Mg. According to [137], indeed, heating the building platform helps stabilise the melt pool, with a positive effect on the defect size. The fatigue strength of specimens produced with a heated platform is larger than that of specimens manufactured with a non-heated platform. Similarly, according to [161], specimens manufactured with a heated platform are more “damage tolerant”.
- Powder size [162,163]: although specimens produced with finer powder have revealed fewer defects, the critical defect sizes are considerably larger in specimens manufactured with this type of powder. Due to the presence of much larger defects in specimens produced with fine powder, a smaller fatigue response has been found for these specimens as compared with their counterparts fabricated from the coarse powder.
- Beam diameter (d): has a very important role in porosity formation. Porosity can increase significantly when using larger laser diameters [164] possibly due to a decrease in beam power density. Power density is defined as the power per unit area, usually expressed in $MWcm^{-2}$. Lower power density requires slower scanning speeds to manufacture samples without imperfections. In turn, slower speeds can cause larger and deeper melt pools which can promote the formation of keyhole porosity. Large beam diameters with slow speeds can thus limit the process window in the power-velocity graph, yielding a less efficient densification mechanism [164,165].

Beyond manufacturing parameters, post-treatments also induce the modification of the microstructure and the relaxation of the residual stresses, affecting the fatigue response [154], while their effect on the defect population is negligible [166].

According to the above analysis, the number of the involved parameters influencing the fatigue response of AM parts makes a fully experimental approach rather unpracticable, opening the path to data-driven methods. To train the models, a dataset composed of fatigue testing data has been populated with the results from the literature.

5.2.2 The dataset

The dataset used to train the ML models is composed of 561 data points (Table 5.2), each defined as a set of process parameters, heat treatment parameters, stress amplitude and the number of cycles at failure. The stress amplitude at stress ratio $R = -1$ is considered in the following analysis. If the experimental data in the literature datasets considered for the validation of the model have been obtained through tests at different stress ratios, the *Smith-Watson-Topper* (SWT) correction has been applied to assess the equivalent stress amplitude $s_{a,eq}$ at R=-1 (i.e., $s_{a,eq} = s_{max} \cdot \sqrt{\frac{1-R}{2}}$, being s_{max} the maximum applied stress in a load cycle).

Table 5.2. AM process parameters of data used to train the machine learning model.

α [°]	P [W]	h [mm]	v [mm/min]	d [µm]	t [µm]	T [°C]	Ref.
0	250	150	500	200	50	30	[167]
90	250	150	500	200	50	30	
45	250	150	500	200	50	30	
0	250	150	500	200	50	300	
90	250	150	500	200	50	300	
45	250	150	500	200	50	300	
0	300	80	2667	70	30	170	[145]
90	300	80	2667	70	30	170	

0	200	61	2667	70	30	170	
90	200	61	2667	70	30	170	
0	275	80	2667	70	30	170	
0	370	190	1300	100	-	35	[168]
90	370	190	1300	100	-	35	
90	350	190	1200	83	50	35	[169]
90	350	190	1200	83	50	200	
0	400	190	1200	83	50	35	[170]
0	400	190	1200	83	50	200	
0	370	160	1300	100	30	35	[159]
0	370	190	1300	100	30	35	
0	370	220	1300	100	30	35	
90	370	160	1300	100	30	35	
90	370	190	1300	100	30	35	
90	370	220	1300	100	30	35	
0	350	170	1150	80	50	150	[171]
90	350	170	1150	80	50	150	
0	400	200	1000	125	30	35	[172]

0	400	200	1000	125	30	35	[173]
0	400	200	1000	70	-	35	[174]
45	400	200	1000	70	-	35	
90	400	200	1000	70	-	35	

In case of missing data, an imputing approach has been used: first, a feature correlation study has been performed to assess the interdependency of process parameters; second, the most correlated feature to the missing field is used to train a regression model (i.e., imputer). The results of the correlation study are reported in Table 5.3, where it can be observed that larger beam diameters usually come with larger thicknesses while increasing the scanning speed requires reduced values of *t*.

Table 5.3. The correlation coefficient of process parameters used to select the relevant features to predict missing values.

Parameter	***t***	***h***	***d***	***v***
t	1	-0.04	0.33	-0.48
h	-0.04	1	-0.17	-0.18
d	0.33	-0.17	1	-0.75
v	-0.48	-0.18	-0.75	1

The missing values of layer thickness in [168] and [174] are obtained by training a regression model that predicts *t* from the beam diameter and scanning speed. The imputed values are 31 and 51 μm for the data referred to in the above-mentioned articles, respectively.

The database has been then used to train and validate the data-driven model described in the following.

5.2.3 ML models

The implemented FFNN has a conventional architecture, trained with a backpropagation algorithm using an Adam gradient descent optimization scheme. The MDS model is a mechanistic PINN with a modified architecture that mimics the fundamental theory of Murakami, as described in the following.

5.2.3.1 Mechanistic Neural Network

The method combines the knowledge of the effect of the defects and the material microstructures on the nucleation and propagation phenomena that govern the fatigue response with the neural network model.

Defects detrimentally affect the fatigue response as they represent critical sites from which the crack can favourably nucleate, and eventually propagate until failure. According to [141], the fatigue response is driven by the largest defect or the most critical from a fracture mechanic perspective. Accordingly, large, and rare defects, rather than the defect density (i.e., the number of defects in a unit material volume), control the fatigue response. Indeed, parts with a high defect density but with defects characterized by small size can show higher fatigue strength than parts with smaller defect density, but with rare large detrimental defects.

The dependency between the fatigue limit and the characteristic defect size can be expressed as:

$$s_l = \frac{C_1 \cdot (HV + 120)}{\left(\sqrt{a_c}\right)^{\frac{1}{6}}} \tag{5.1}$$

being s_l the fatigue limit, i.e., “the threshold for crack propagation”, HV the material Vickers hardness, a_c the characteristic defect size and C_1 a coefficient that accounts for the location of the defect (i.e., surface defects are more critical than internal defects since characterized by a larger Stress Intensity Factor (SIF)[141]). According to Equation 5.1, the defect characteristic size is accounted as the square root of the defect area in a direction perpendicular to the maximum applied stress.

Equation 5.1 puts into evidence that the material Vickers hardness also affects the fatigue response. Indeed, according to Murakami, the material Vickers hardness is the "microstructural parameter", i.e., it accounts for the influence of the microstructure on the fatigue response. The fatigue response thus depends on the defect size and on the material microstructure, which can be represented by the material Vickers hardness.

The Murakami formulation has proven to be valid for parts produced through AM processes, by considering an equivalent defect size in place of a_c[175]. Equation 5.1 can be also exploited to assess the dependency of the fatigue response in the presence of defects and the fatigue life, i.e., by normalizing the applied stress amplitude s_a by the corresponding fatigue limit s_l computed with Equation 5.2:

$$\frac{s_a}{s_l} = C \cdot {N_f}^k, \tag{5.2}$$

being N_f the number of cycles to failure and C and k two material parameters that must be estimated from the experimental data. Equation 5.2 has been employed in different forms to model the dependence between s_a, N_f and the defect size [141,176,177] and more complex trends, like the *duplex trend* [178].

Standing on what has been discussed so far, the fatigue design of AM parts requires a model able to correlate the defects and the material microstructure to the fatigue strength. Defect size and material microstructure are differently affected by the process and post-treatments parameters [152]. Heat treatments have an overall marginal influence on the defect size [166,179–181], while strongly affecting the final microstructure and, accordingly, the Vickers hardness, as experimentally shown in [182].

To summarize, Figure 5.1 clarifies the factors affecting the fatigue response of AM parts. Process parameters influence the defect size and the microstructure, whereas heat treatments affect only the microstructure. According to [179], the heating temperature can be considered the main factor that controls the microstructure and, consequently, the Vickers hardness.

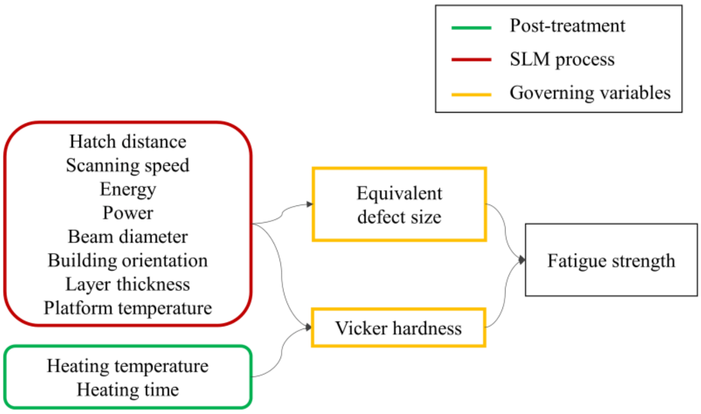

Figure 5.1. A flow chart that summarizes how the SLM and heat treatment factors affect the fatigue life of AM parts.

This physical evidence is exploited to build a PINN model that predicts the fatigue response of AM parts from the input process parameters, and heating treatment variables.

In the physically inspired model, the prior mechanistic knowledge about the relations between the process parameters and the microstructural properties is enforced in intermediate layers of the network.

The PINN modular structure is composed of two main branches:

- Defect estimation: vector of variables $\boldsymbol{\theta}$ (layer thickness, beam diameter, hatch distance, scanning speed, building orientation, power, and temperature of the platform) feeds the neural network $\mathbb{N}^1$ that predicts the effect of these parameters on the defect size.
- Microstructure estimation: vector of variables $\boldsymbol{\phi}$ (process parameters and duration and temperature of the thermal treatment) feeds the neural network $\mathbb{N}^2$ that predicts the microstructural strength parameter.

According to Equations 5.3-4, the fatigue strength, defined as the stress value at which the failure occurs after N_f cycles, is proportional to the microstructural strength and inversely proportional to the defect area. Following this prior knowledge, the ratio from the defect estimation branch and the microstructure branch results is computed in a custom layer of the network. The ratio is passed to a trainable layer to predict the fatigue strength s_a according to Equation 5.3:

$$s_a = \frac{f(HV)}{f\left(\sqrt{a_c}\right)} f\left(N_f\right), \tag{5.3}$$

where $f(HV)$ is a function of the Vickers hardness (and, accordingly, of the part microstructure), $f\left(\sqrt{a_c}\right)$ is a function of the defect size, whereas $f\left(N_f\right)$ is a function of N_f. Equation 5.3 correlates the fatigue strength (s_a) to the fatigue life (N_f) and model the influence of defects and microstructure on fatigue life. These quantities, $f(HV)$, $f\left(\sqrt{a_c}\right)$ and $f\left(N_f\right)$ are unknown in the design phase and are estimated by the NN. For this reason, a custom layer replicating Equation 5.3 with trainable parameters $\boldsymbol{w_C}$ is built. This final layer takes as input the latent scalar variables Φ and Θ, and the input N_f to predict the fatigue strength s_a at the number of cycles N_f:

$$s_a = \frac{\mathbb{N}^1(\boldsymbol{\theta}; \boldsymbol{w_\theta}, \boldsymbol{b_\theta})}{\mathbb{N}^2\left(\boldsymbol{\phi}; \boldsymbol{w_\phi}, \boldsymbol{b_\phi}\right)} \left(\frac{w_C^1}{N_f}\right)^{w_C^2} = \frac{\Theta}{\Phi} \left(\frac{w_C^1}{N_f}\right)^{w_C^2} \tag{5.4}$$

In Equation 5.4, $\boldsymbol{w}$ and $\boldsymbol{b}$ are the trainable weight and bias of the microstructural and defect networks, respectively indicated with ϕ and θ.

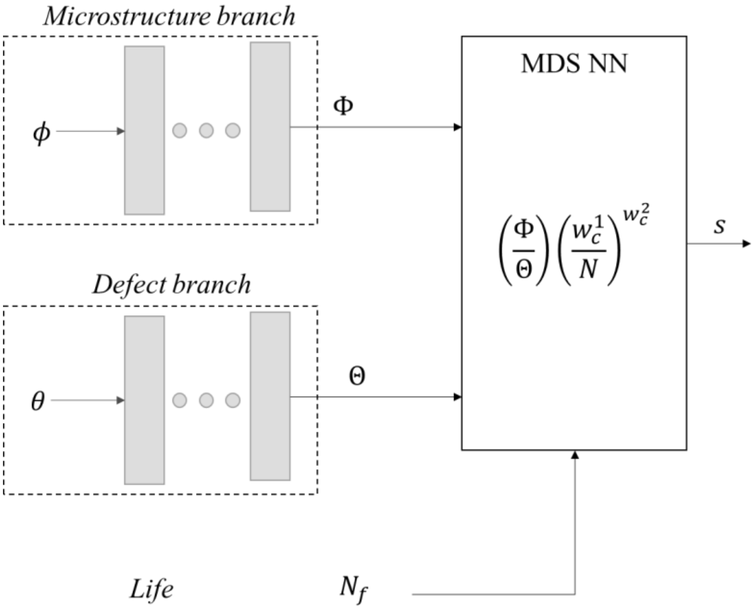

Figure 5.2. Schematic representation of the modular MDS NN.

Since the output layer takes as input the latent parameters Φ and Θ, the encoded process parameters are related to the $s_a - N_f$ trend and the network can learn the effect of these variables on the shape of the fatigue response over the entire life. It is worth noting that the c1 coefficient in the Murakami formulation depends on the defect location, accounting for the larger criticality of surface defects. The injected physic in the NN model mimics the Murakami formulation in its form and constrains the interaction between defect-correlated and microstructure-correlated features, enforcing the prediction of interpretable latent variables (Figure 5.2), but does not directly estimate the C parameter of Equation 5.2. Most of the analysed datasets do not report information on the defect size and location, precluding the direct usage of the defect information for the model training. Superficial defects have a decremental effect on the fatigue strength, yielding a 10% fatigue strength reduction for internal defects, therefore the uncertainty on the locations of the defects is estimated to influence the model accuracy of the same quantity.

The loss function of the NN is expressed as follows:

$$\mathcal{L} = \frac{1}{N}\left| \boldsymbol{S} - \frac{\mathbb{N}^1(\boldsymbol{\theta}; \boldsymbol{w_\theta}, \boldsymbol{b_\theta})}{\mathbb{N}^2(\boldsymbol{\phi}; \boldsymbol{w_\phi}, \boldsymbol{b_\phi})}\left(\frac{w_C^1}{\boldsymbol{N_f}}\right)^{w_C^2} \right|_{F2} \tag{5.5}$$

Where operator $|\cdot|_{F2}$ stands for the Frobenius norm.

The designed PINN intrinsically complies with the S-N monotonicity constraint, being the derivative of the output layer with respect to the number of cycles always negative.

5.3 Results

5.3.1 FFNN

The structure of the neural networks used in this section is summarised in Table 5.4.

Table 5.4. Summary of FFNN optimized structures with activation function and number of neurons of each layer

Layer	Neurons	Activation function	Output shape
Input	40	ReLU	(40, 1)
Dense 1	50	ReLU	(50, 1)
Dense 2	50	ReLU	(50, 1)
Dense 3	40	ReLU	(40, 1)
Output	40	ReLU	(1, 1)

The model has been trained with three different subsets of the available parameters:

a) Orientation, energy, beam diameter, hatch, layer thickness, number of cycles, and plate temperature.
b) Same of configuration a) with duration and temperature of thermal treatment.
c) Same as configuration b) with powder size.

To assess the approximation capability of the ML models, neural networks are trained with 80% of the available data, while the remaining 20% is used as a validation dataset to check that the network is not overfitting the training observations. The network MSE is minimized with the adaptive optimizer algorithm Adam, setting a learning rate of 0.07 and an exponential decay rate of 0.9. Network weights and bias are updated at each iteration with a standard back-propagation algorithm and the training is stopped when an increase of 5% on the MSE is not registered for 20 iterations.

The mean squared errors of the three FFNN models are compared in Figure 5.3.

a)

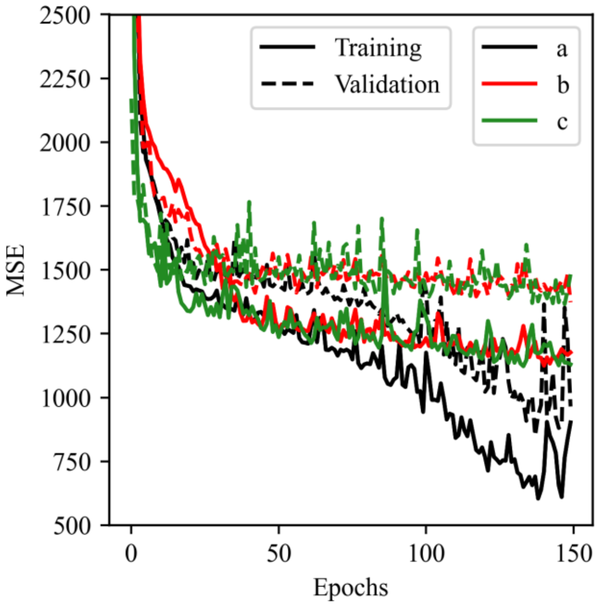

b)

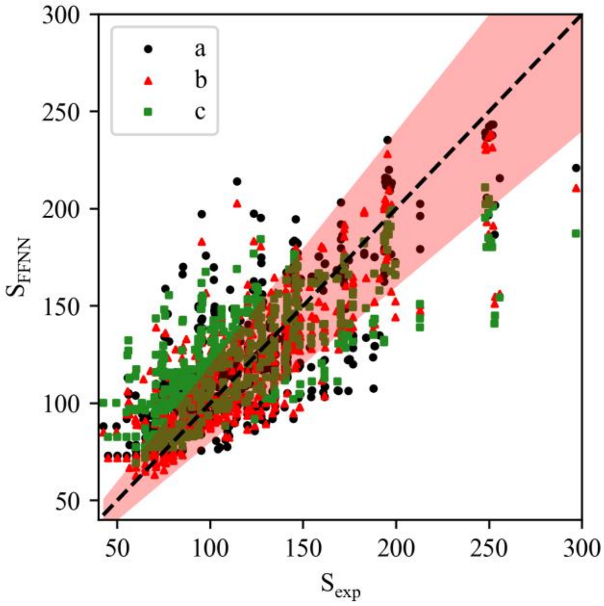

Figure 5.3. A comparison of the FFNN loss on training and validation data over the training epochs (a) and the accuracy plot of the trained model (b) for the three analysed configurations (*a, b* and *c*).

Configuration *a* of the FFNN architectures reveals the best accuracy, with an MSE of 700 and 800 on the training and validation datasets (i.e., there is no overfitting on training observation), respectively (see Figure 5.3a). Results are reported in the accuracy plot (Figure 5.3b) where a ±30% error band is reported in shaded red. It can be concluded that FFNN struggles to learn the effect of post-treatment parameters and powder size effect on the fatigue response, the reduced parameters set configuration being the most effective in predicting the fatigue stress. From here on, results referring to FFNN are obtained with configuration *a*).

5.3.2 Mechanistic NN

The combined PINN is composed of three main subnetworks:

- Microstructural branch: predicting the influence of AM manufacturing parameters and heat treatment effect on the final microstructure.
- Defect branch: predicting the effect of AM manufacturing parameters on the defects.
- Output branch: a single custom layer computing the interaction of the previous branch predictions with the finite lifetime.

A schematic representation of the proposed PINN is presented in Figure 5.4.

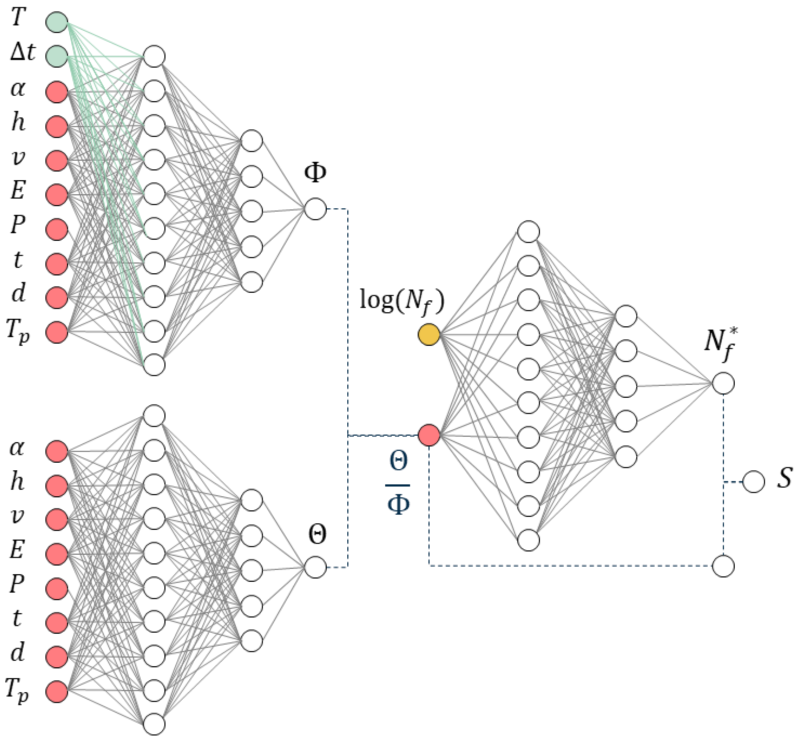

Figure 5.4. The neural network architecture of the PINN. In red are the manufacturing parameters, in green, are heat treatment variables and in yellow is the life cycle. Dashed lines indicate custom layers, while continuous lines indicate neural network connections.

The two branches - accounting for the effect of manufacturing parameters on microstructure and defects, respectively - predict the latent variables Θ and Φ. Following the latent variables prediction, a custom layer calculates the ratio Θ/Φ, recalling Equation 5.3. The characteristic ratio and the number of cycles to failure are concatenated into a vector that feeds the last NN block, where Equation 5.4 is performed. The interaction between the ratio Θ/Φ, and the number of cycles N_f, allows the network to learn an S-N relation whose trend depends on the interaction of the manufacturing parameters with N_f. In other words, the parameters w_1^* and w_2^* of Equation 5.4 depend on the manufacturing process; otherwise, the network could only predict S-N curves with a fixed trend, scaled by a factor Θ/Φ.

The hyperparameters of the model architecture are summarised in Table 5.5.

Table 5.5. Physic-informed neural network architecture

NN branch	Layer	Neurons	Activation function
$\mathbb{N}^1$	Input 1	10	SELU
	Dense 1	5	SELU
	Dense 2	1	Linear
$\mathbb{N}^2$	Input 2	10	SELU
	Dense 3	5	SELU
	Dense 4	1	Linear
Output	Dense 5	10	ReLU
	Dense 6	5	Linear
	Dense 7	1	Linear
	Custom	-	-

The weights of dense layers are regularized with an L1 regularization penalties algorithm, adding to the loss function the L1 norm of the layer weights. In this way, the training process converges to a simpler network, suppressing weak connections with low weights, and gaining robustness against noisy data. The activation functions of the input and hidden layers of the $\mathbb{N}^1$ and $\mathbb{N}^2$ networks have been selected with sensitivity analysis on the network performance, varying the activation function among linear, ReLU, Hyperbolic tangent, Exponential Linear Unit (ELU) and SELU. The network has been trained ten times with each activation function, with a random selection of the training data. Table 5.6 summarizes the results of this analysis, comparing the mean and the standard deviation of the mean squared error of the PINN with different activation functions.

Table 5.6. Mean and standard deviation of the mean squared error of the PINN with different activation functions. Results refer to ten repetitions of the training process with training data randomly sampled.

	MSE	
Activation	Mean	St. dev.
Linear	728	314
Tanh	1639	415
ReLU	5060	6602
ELU	2530	4438
SELU	666	189

The best activation function is the SELU, leading to a consistently lower error in the predictions. The higher non-linearity of the SELU function lets the network capture the complex interaction of the process parameters and its effect on the latent variables. The results of the model are shown in the accuracy plot of Figure 5.5, where the predicted fatigue life is compared with the experimental data on a scatter plot, where the dashed lines indicate the perfect accuracy, which is impossible to achieve due to the intrinsic scatter of the experimental results, while the red shaded band refers to the ±50 MPa error band. Most of the data, from both training and validation sets, falls within the error band, while only a few points deviate more than 50 MPa from the exact values.

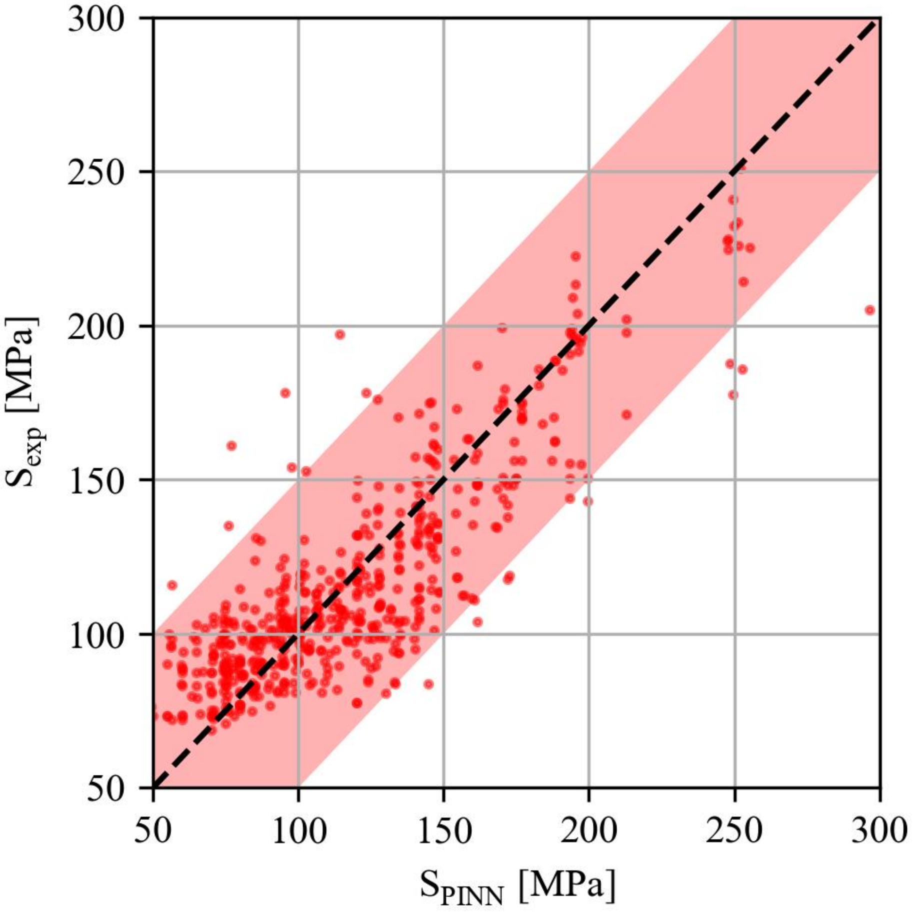

Figure 5.5. A comparison of the PINN prediction with the experimental observation for all the available data. The shaded area represents the ±50MPa error band

Since the scatter in the fatigue response of AM parts increases with the number of cycles, i.e., at lower stresses, in the left portion of the plot we observe a lower accuracy of the model. The reason behind this behaviour relies on the deterministic nature of the proposed approach, in contrast with the stochastic nature of the fatigue phenomenon; a modification of the PINN predicting a probabilistic result is under study and will be the object of future research.

Figure 5.6 shows the predicted S-N curves of three different process configurations comprised in the dataset. The datasets have been selected to show the strong influence of the process parameters on the fatigue response of AlSi10Mg parts manufactured with AM and the ability of the model to predict it. The PINN can efficiently assess the fatigue behaviour of parts produced with different process conditions that yield remarkable variation in the S-N plots, e.g., 80 MPa (blue circle), 100 MPa (green squares) and 120 MPa (orange triangles) strength at 10^6 cycles. Beyond an overall good precision, the model shows robustness to the outliers. As can be observed for the green curve, the physical behaviour is preserved against scattered data.

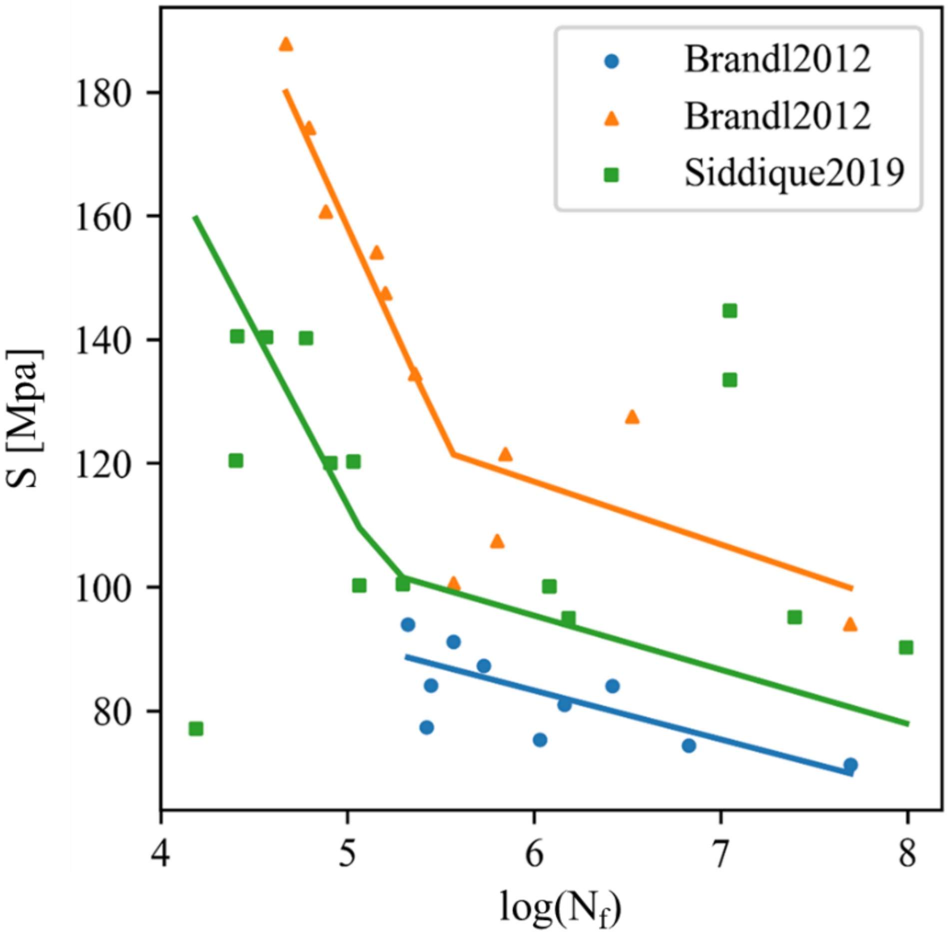

Figure 5.6. Fatigue curves predicted with the PINN algorithm and compared with the experimental data. The process parameters and experimental data are referred to [167,183]

Moreover, Figure 5.6 shows that the predicted stress-life curves of the PINN reflect distinguishable characteristics of the fatigue response of the AlSi10Mg alloy [184]:

- The bi-linear trend within a lifetime range above 10^4 cycles.
- A knee point, defined as the value of N_f where the slope of the S-N curves changes, between 10^4 and 10^6 cycles.
- The slope decreases after the knee point.

The bi-linear trend is enabled by selecting a ReLU activation function of the network operating on N_f. The possible occurrence of a bilinear trend must be considered for the investigated aluminium alloy, according to the experimental evidence [185,186].

5.3.2.1 Interpretability

The model can be interpreted as a physics-informed encoder that embeds the effect of process parameters into two latent variables, Θ and Φ, controlling the variation of AM material strength due to defects and microstructural properties, respectively. While complying with the empirical findings and established models, this architecture introduces interpretable mechanisms of the ML model. Indeed, $\mathbb{N}^1$ and $\mathbb{N}^2$ subnetworks can be independently analysed to assess the effect of microstructural ($\boldsymbol{\theta}$) and defect-associated ($\boldsymbol{\phi}$) variables on the fatigue response.

Figure 5.7a shows the effect of latent variables Θ and Φ on the fatigue strength at 10^6 cycles. It can be observed that an increase of the defect-associated variable Φ leads to a fatigue strength reduction (moving right in the graph from the diagonal, while the microstructure-associated variable Θ has the opposite effect. The physics latent space encodes the process effect on the fatigue response, making the NN interpretable from an engineering perspective. The latent variables map indicates the best manufacture condition at the desired lifetime N_f and, can thus be used to optimize the process parameters to enhance the fatigue response. Figure 5.7b shows the effect of the output layer on the relation between the stress amplitude and the characteristic ratio at different values of N_f. It can be observed that the number of cycles affects the slope of the curve, modelling different latent parameter effects at the different number of cycles.

a)

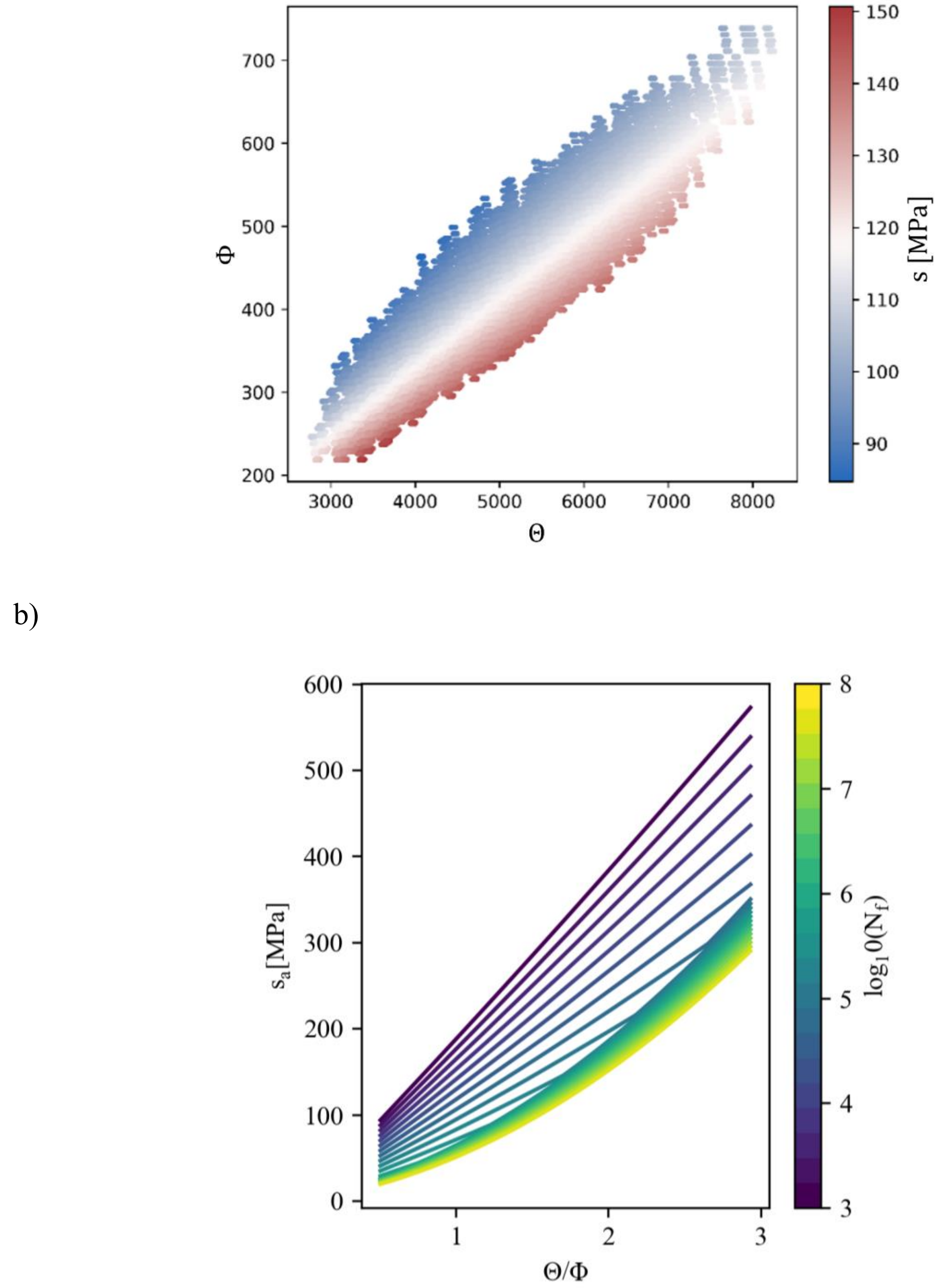

Figure 5.7. a) Fatigue strength variation with latent variables at N_f=10^6 b) Correlation of the fatigue strength with Θ/Φ at different N_f

5.3.3 Comparison

In this subsection, the results of the PINN and FFNN are compared, and the models are evaluated in terms of overall accuracy, ability to extrapolate results beyond the observed domain and efficiency in capturing the process parameters effect. Finally, a new testing set of experimental data is introduced to test the models beyond the training and validation domains.

5.3.3.1 Model accuracy

Figure 5.8a reports the model prediction compared to the experimental data, with the black dashed line indicating the exact predictions, and the red shaded area evidencing the ±50MPa error interval. The proposed modular PINN enhances the prediction accuracy of the ML model, efficiently predicting the fatigue strength in the finite life region (at higher stress levels). The loss history plot during the training process (Figure 5.8b) shows that the PINN achieves an approximately 20% lower MSE (626 respect to 756), by introducing the physical relations between the mechanistic feature of the phenomena.

a)

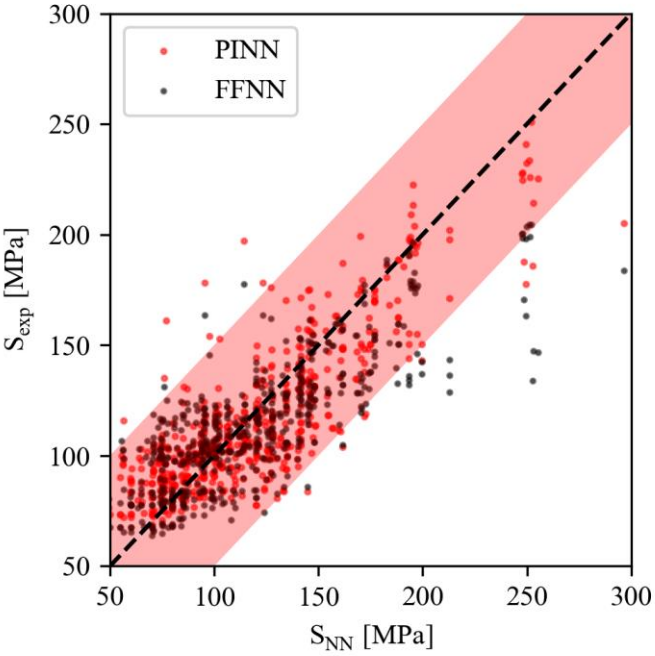

b)

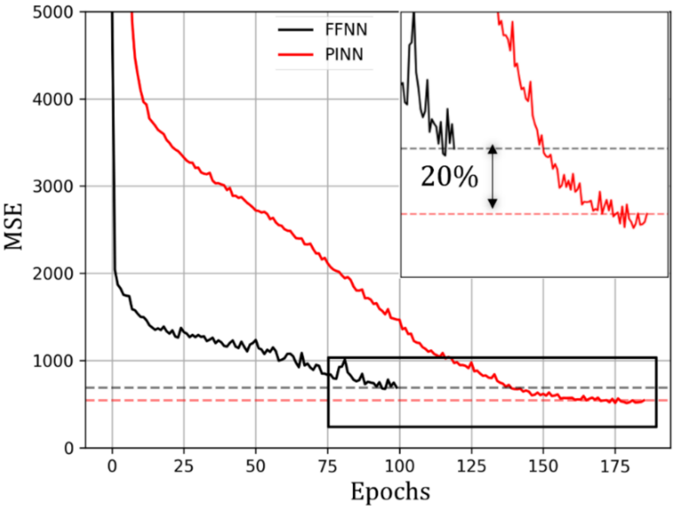

Figure 5.8. a) FFNN and PINN predictions compared to experimental observation. The shaded band refers to a 20% error. b) MSE of PINN and FFNN during the training process.

The MSE of the testing dataset is 730 and 1100 for the PINN and FFNN, respectively.

5.3.3.2 Extrapolation outside the observed domain

The trained models can be used to assess the S-N relation in the Very-High-Cycle Fatigue (VHCF) range, i.e., beyond 10^6 cycles. The VHCF response learned from the available data can be extended to manufacturing configurations not yet tested above 10^6 cycles. Accordingly, the VHCF response of aluminium alloys with a different set of parameters can be extrapolated by transferring the learned relation from the tested manufacturing configurations. Figure 5.9 shows a representative example of the predicted VHCF response for two different datasets [145,187] obtained with a different combination of manufacturing process parameters, reported in Table 5.2.

a)

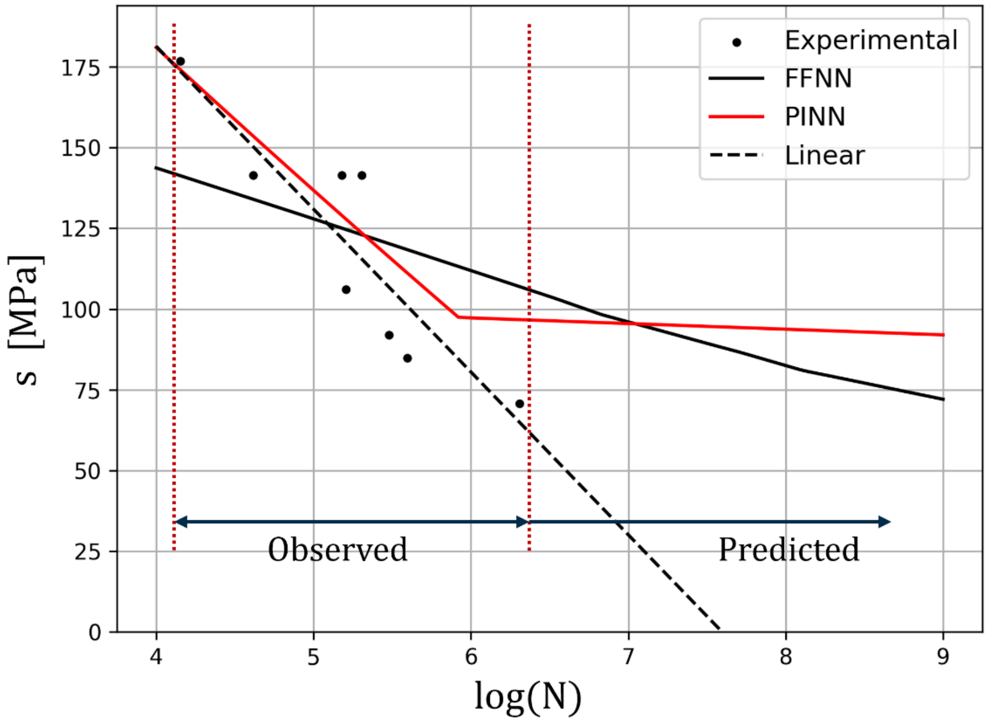

b)

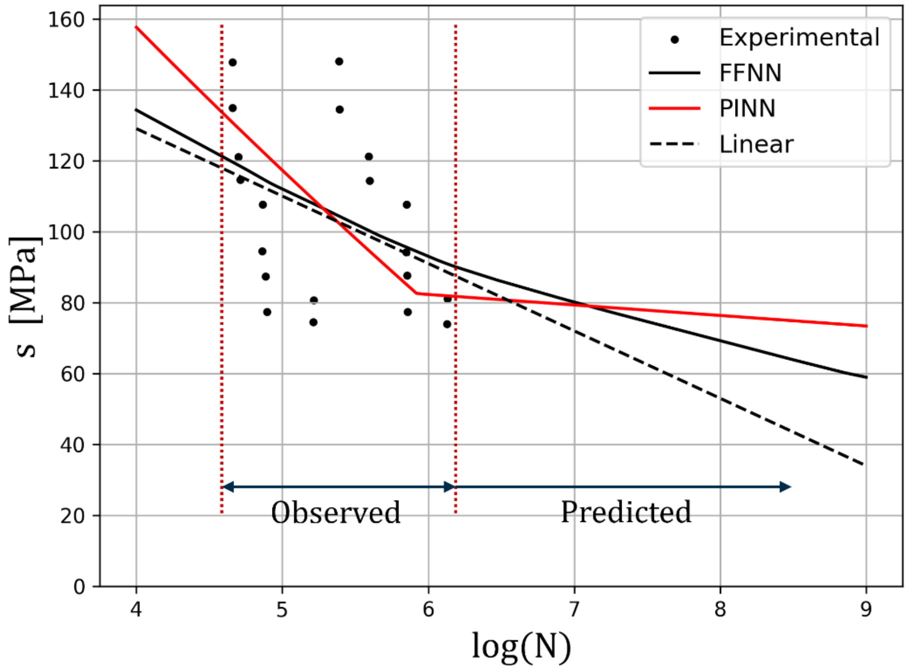

Figure 5.9. Extrapolated predictions of NN models outside the observed interval for fatigue data in a) [145] and b) [167]

Enforcing the physics constraint during the training of the neural networks leads towards a more reliable extrapolation model that predicts the physics-compliant fatigue response of AM alloy beyond the observed domain. FFNN predictions decrease monotonically within the entire lifecycle domain, even above 10^6 cycles, whereas the PINN curves exhibit a double linear trend in agreement with the experimental observations. This analysis proves the best predicting capability of the PINN model, where the training process is guided by experimental evidence on the influence of defects and microstructure on the fatigue response. On the other hand, a "black box" approach would perform better only if a significantly larger dataset was considered for training the network. Accordingly, a PINN approach should be preferred since its results are interpretable and the physical mechanisms of the fatigue response of AM parts are preserved.

5.3.3.3 Process parameters sensitivity

In this section, the ML models are used to predict the effect of individual parameters on the fatigue response of AlSi10Mg alloys. The sensitivity analysis of the fatigue response to the AM process parameters is performed on the baseline configuration described in Table 5.7.

Table 5.7. AM process parameter configuration used for the sensitivity analysis

	α [°]	**P** [W]	h [µm]	**v** [m/min]	**d** [µm]	**t** [µm]	**T_p** [°C]
A	0	250	80	2	100-200	50	80
B	0	250	80	2	100	30-70	80

Figure 5.10 shows the predicted fatigue response sensitivity to the beam diameter (Figure 5.10a) and the layer thickness (Figure 5.10b). The prediction of the PINN model (red) is compared with the FFNN (black) at different levels of the process variables.

a)

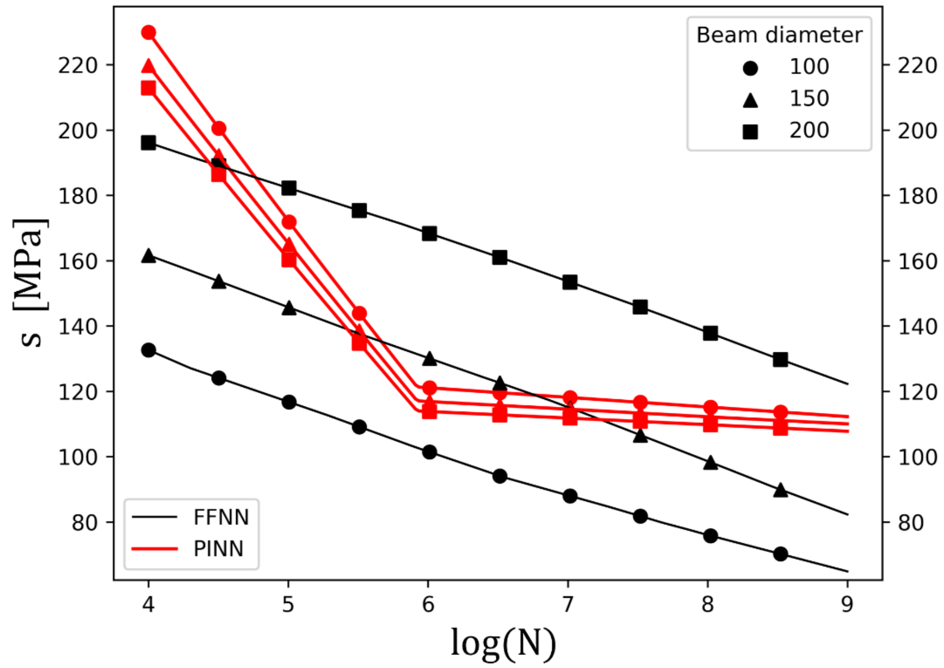

b)

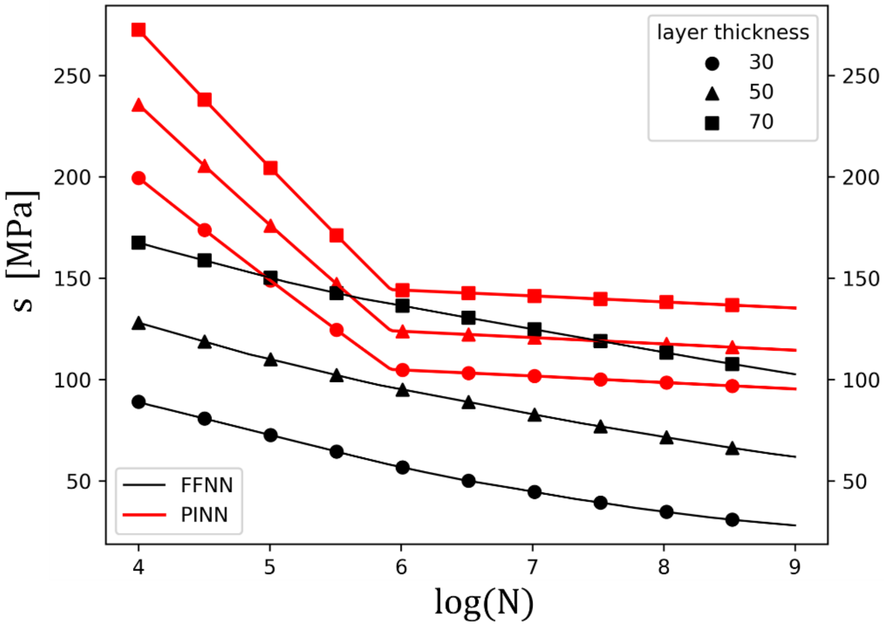

Figure 5.10. Predicted SN curve sensitivity to the AM process parameters: a) beam diameter; b) layer thickness.

The PINN prediction of the fatigue response of additively manufactured AlSi10Mg parts with different beam diameter values reflects the trend found experimentally in the literature. For example, the analysis carried out in [164] shows that larger defects tend to form as the diameter of the laser beam is increased, thus negatively affecting the fatigue response. A similar trend can be observed in Figure 5.10a, where the S-N curves obtained with increasing diameters of the laser beam move downward.

The sensitivity of the ML models to the hatch distance h parameter has been investigated by comparing the FFNN and PINN results with the experimental results in [188], where h has been varied between 160, 190 and 200 µm and specimens have been tested at a stress amplitude of 100 MPa and 80 MPa with a stress ratio of 0.1 (Figure 5.11). These data were used as a testing set, meaning that are not included neither in the training nor in the testing dataset. After having applied the STW corrections, the number of cycles to failure at 80MPa and 100MPa has been predicted with the PINN (Fig. 5.11a) and the FFNN (Fig. 5.11b) models. Cross markers indicate the predicted life at 100 MPa, plus markers refer to 80 MPa amplitude.

a)

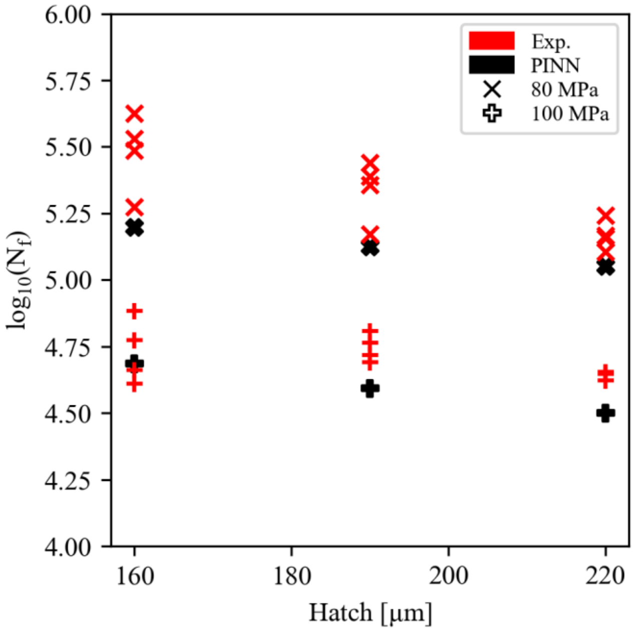
6.00
5.75
5.50
5.25
5.00
4.75
4.50
4.25
4.00
$\log_{10}(N_f)$
160
180
200
220
Hatch [µm]
Exp.
PINN
80 MPa
100 MPa

b)

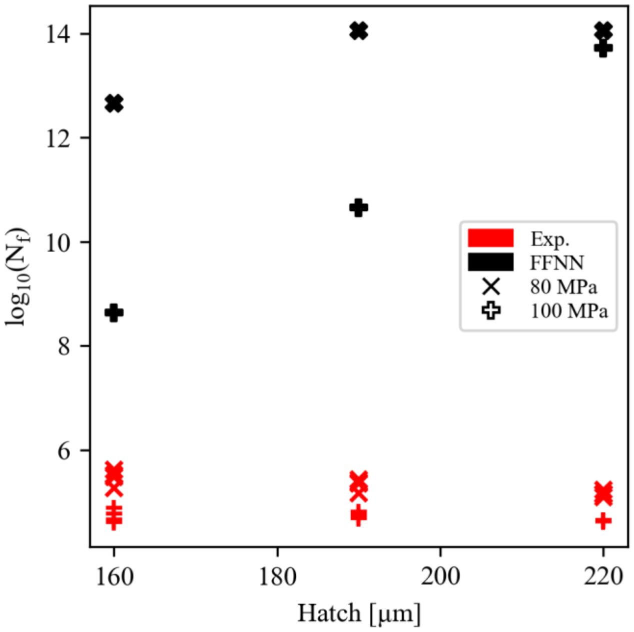
14
12
10
8
6
$\log_{10}(N_f)$
160
180
200
220
Hatch [µm]
Exp.
FFNN
80 MPa
100 MPa

.

Figure 5.11. The predicted number of cycles at failure with PINN (a) and FFNN (b) by considering the process parameters and experimental data in [159]. Cross markers indicate the predicted life at 100 MPa, plus markers refer to 80 MPa amplitude (both at R=0.1).

Figure 5.11a demonstrates the efficiency of the PINN to capture a linearly decreasing trend of Nf with increasing *h*, in line with the experimental evidence. Additionally, the decrement of the fatigue life with the increased stress amplitude is in agreement with the experimental results, with most of the experimental and PINN results coinciding with the PINN predictions being slightly conservative. FFNN, on the contrary, significantly overestimates the fatigue life. Results in Figure 5.11b confirm that the FFNN model struggles in predicting fatigue behaviour under processing conditions different from the one contained in the training database.

Figure 5.12 shows the Pearson's correlation coefficient between the AM parameters with the stress amplitude, for both FFNN and PINN predictions compared with experiments. The 95% confidence interval of the experimental data is described by the black lines, highlighting the stochastic nature of the fatigue response. In contrast, the PINN predictions are deterministic and represent the mean value of the fatigue response. Looking at the results of the correlation analysis between the process parameters and the fatigue strength, it can be concluded that the PINN accurately captures the mechanistic relations on the mean of the observed data. Future work will be implementing a statistical model capable of predicting a scattered response, as observed in experiments.

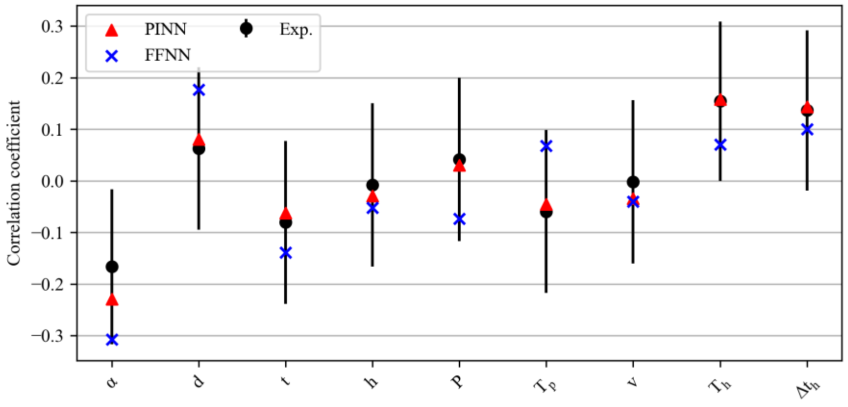

Figure 5.12. Correlation study of process parameters with stress amplitude. Results from the FFNN and PINN are compared with the experimental observation.

5.3.3.4 Validation

In this section, the trained ML algorithms are validated against an additional dataset, not considered in previous analyses, which process parameters are reported in Table 5.8.

Table 5.8. AM manufacturing parameters of the validation dataset

α [°]	P [W]	h [mm]	v [m/min]	d [μm]	t [μm]	T_p [°C]	T_h [°C]	Ref.
90	350	130	1.65	-	50	150	200	[189]

Being the laser beam diameter not reported in the article, multiple predictions are performed varying its value in the range between 70 and 200 μm (i.e., the maximum and minimum values of beam diameter observed in the full dataset). The results of the multiple predictions are compared with the experimental data in Figure 5.13.

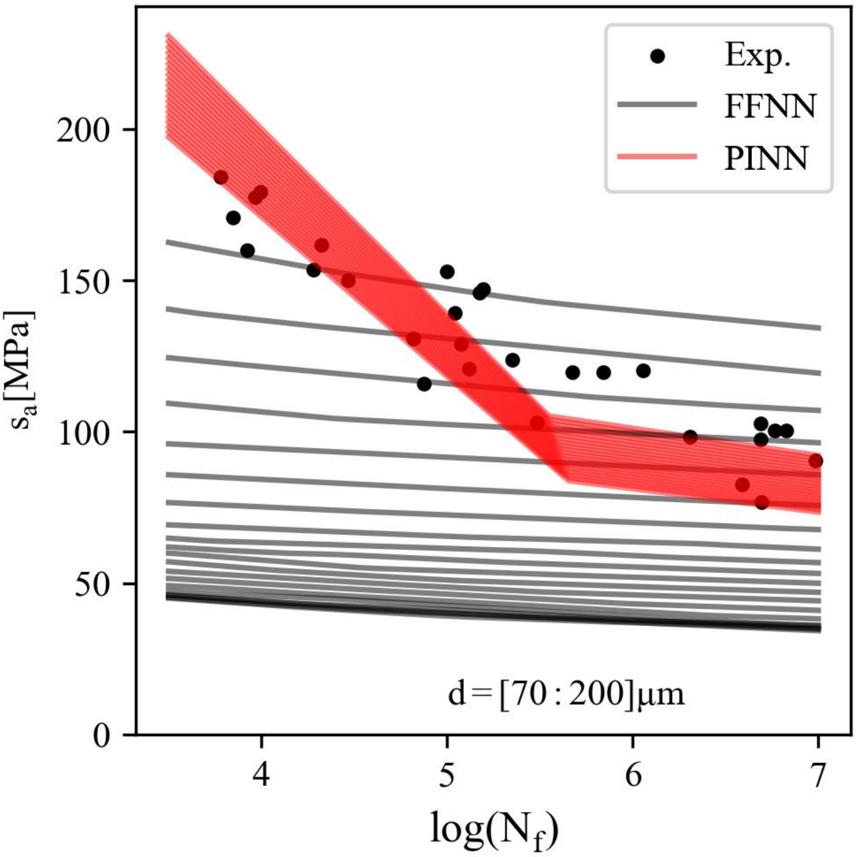

Figure 5.13. PINN predictions of the testing dataset compared with experimental results. Multiple lines refer to different values of the beam diameter, varied in the range of 70 to 200 µm, whereas black dots indicate the experimental data.

Figure 5.13 shows that the S-N curve estimated with the PINN models is in good agreement with the experimental data. On the other side, the FFNN overestimates the effect of the beam diameter on the fatigue response, leading to inaccurate predictions. The PINN predicts the fatigue strength of the AlSi10Mg with an average error of 4% and a maximum error of 17% (computed on a fatigue curve obtained with a beam diameter of 135 μm).

This further validation confirms the power of using ML approaches for estimating the fatigue response of AM parts starting from the process parameters. Indeed, once the network has been trained, the optimal process parameters ensuring the best fatigue performances can be attained without the need for time-consuming and expensive experimental tests to assess the S-N curve or the defect population.

Moreover, the larger efficiency of PINN approaches instead of a “black box” has been further proven with this validation, since the predicted S-N curve is close to that estimated from the experimental data.

5.4 Conclusions

A novel data driven method based on established fatigue models has been developed to predict the influence of the AM process parameters on the fatigue strength of AlSi10Mg parts. Using the experimental results of SLM alloy fatigue testing, a standard FFNN and the MDS NN models have been trained to assess the fatigue life directly from the layer thickness, beam diameter, hatch distance, energy density, building orientation, and heat treatment properties. The PINN combines a custom architecture with a modified loss function to merge the damage-tolerant fatigue equations with the NN in a streamlined pipeline: the process parameters are used to predict two latent variables associated with the material defectiveness and the resultant microstructure with separate networks, which are passed to a custom layer that mimics the Murakami equations to predict the fatigue strength. As a result, the proposed architecture enforces proper constraints on the S-N curves to get physics-consistent predictions.

The FFNN and PINN are compared, highlighting the PINN's higher accuracy, and ability to predict S-N curves with the characteristic features of fatigue curves like the bi-linear trend, and knee point around 10^4 cycles. The physics-based model is interpreted and the relation between the latent variables representing the microstructure and defect effect on the fatigue response is investigated, confirming the physics compliance of the proposed architecture. The parameter sensitivity of the trained model is also verified, showing, for example, that the beam diameter reduced the fatigue strength, in agreement with the literature results. Finally, the FFNN and PINN are validated against an AlSi10Mg dataset [189] not included in the training and validation database. The FFNN cannot predict the fatigue response properly, overestimating the effect of the beam diameter, leading to unphysical curves with large errors. The PINN instead, shows a good agreement with the experimental data (mean error of 4% and maximum error of 17%). This validation further proved the effectiveness of the strategy developed to model the influence of defects and microstructure on the fatigue response and to consider the experimental evidence in the model.

In conclusion, the PINN model designed to enforce the physics knowledge on the fatigue of metals has been shown to accurately predict the S-N response of AM AlSi10Mg from the process parameters and heat treatment properties and should be preferred to FFNN "black box" approach, due to its better predictive capability. The developed model allows designers to assess the fatigue strength directly from the process parameters and heat treatment properties, thus without the need to perform time-consuming and expensive experimental fatigue tests. Moreover, it can be reliably used to optimize the part design to achieve the best fatigue performance. The proposed methodology is inspired by macroscale phenomenological methods that do not explicitly model the microscale mechanism that governs the nucleation and propagation of cracks; hence the model cannot capture this lower scale phenomena. Future research will focus on the extension of the present framework to other classes of materials (i.e., transfer learning) and the implementation of probabilistic models to capture the epistemic nature of the fatigue phenomenon with probabilistic ML models combined with physics-informed architectures.

Appendix

Appendix A. Homogenization method

A.1. Two-scale equilibrium problem

The macroscopic response of heterogeneous materials is governed by deformation mechanisms taking place at two different scales: the microscale and the macroscale. The microscale is defined by the RVE which has a characteristic dimension l, while the macroscale is defined by the scale of the analysed structure L. Under the assumption of linear elasticity, the two scales can be studied separately (l<<L), and the heterogeneous response of the material can be replaced by homogenized behaviour. At the macroscale, the constitutive model of the material is given by:

$$\bar{\sigma} = \bar{C}\bar{\varepsilon}\,, \qquad (A.1)$$

With $\bar{C}$ the elastic tensor, $\bar{\sigma}$ and $\bar{\varepsilon}$ the average stress and strain fields that comply with the microscale equilibrium are given by:

$$\begin{cases} div\sigma = 0, & in\,\Omega, \\ \varepsilon(\mathrm{x}) = \nabla^{\mathrm{S}}(u^{*}(x)) + \bar{\varepsilon}, & in\,\Omega, \\ \sigma(x) = C_i\colon \varepsilon(x), & in\,\Omega_i, \\ \nabla^{s}\big(u^{*}(x)\big) = 0, & in\,\Omega, \end{cases} \qquad (A.2)$$

where C_i is the stiffness tensor of phase i, and $\nabla^{\mathrm{S}}(u^{*}(x))$ is the fluctuating part of the strain in the RVE, whose average should vanish over the RVE.

A.2 Fast Fourier Transform (FFT) method

Under the assumption of periodic boundary conditions, the microscale problem can be solved using the FFT method developed by H. Moulinec and P. Suquet[190]. The method proposes an auxiliary problem to A.2, introducing a reference material with a stiffness tensor C^0 and a polarization stress field $\tau(x)$. The problem can be expressed as:

$$\begin{cases} div\sigma = 0, & in\,\Omega, \\ \varepsilon(\mathrm{x}) = \nabla^{\mathrm{S}}(u^*(x)) + \bar{\varepsilon}, & in\,\Omega, \\ \sigma(x) = C^0\colon \varepsilon(x) + \tau(x), & in\,\Omega_i, \\ \tau(x) = \left(C^i - C^0\right)\colon \varepsilon(x), & in\,\Omega_i, \\ \nabla^s\left(u^*(x)\right) = 0, & in\,\Omega. \end{cases} \qquad (A.3)$$

That leads to:

$$\nabla \cdot (C^0\colon \bar{\varepsilon}) + \nabla \cdot (C^0\colon \hat{\varepsilon}) + \nabla \cdot \left(\tau(x)\right) = 0, \qquad (A.4)$$

giving:

$$\nabla \cdot (C^0\colon \hat{\varepsilon}) = -\nabla \cdot \tau(x), \qquad (A.5)$$

The solution to this problem can be expressed by introducing the isotropic Green's operator Γ^0 based on the reference material C^0:

$$\hat{\varepsilon}(x) = -\Gamma^0 * \tau(x), \qquad in\,\Omega, \qquad (A.6)$$

with * indicating the convolution product. Leading to:

$$\varepsilon(x) = \bar{\varepsilon} - \Gamma^0(x) * \left(\sigma(x) - C^0\colon \varepsilon(x)\right), \qquad (A.7)$$

Green's function for isotropic materials with applied periodic boundary conditions in the Fourier space is given by:

$$\hat{\Gamma}^0_{ijkl} = \frac{1}{4\mu^0|\xi|}\left(\delta_{ki}\xi_h\xi_j + \delta_{li}\xi_l\xi_i + \delta_{kj}\xi_k\xi_j + \delta_{jl}\xi_j\xi_l\right) - \frac{\lambda^0 + \mu^0}{\mu^0(\lambda^0 + 2\mu^0)}\frac{\xi_i\xi_j\xi_k\xi_l}{|\xi|^4}, (A.8)$$

where ξ is the coordinate in the Fourier space, μ^0 and $\lambda^0$are the Lame's constants of the reference materials.

The problem can then be solved iteratively with a fixed-point solution scheme, as described in Table A0.1:

Real space		**Fourier space**
Initialize	$\boldsymbol{\varepsilon^i(x) = \bar{\varepsilon}}$	

$\boldsymbol{\sigma}^{\boldsymbol{i}}(\boldsymbol{x}) = \boldsymbol{C}(\boldsymbol{x}): \boldsymbol{\varepsilon}^{\boldsymbol{i}}(\boldsymbol{x})$	
$\boldsymbol{\tau}(\boldsymbol{x}) = \boldsymbol{\sigma}^{\boldsymbol{i}}(\boldsymbol{x}) - \boldsymbol{C}^{\boldsymbol{0}}: \boldsymbol{\varepsilon}^{\boldsymbol{i}}(\boldsymbol{x})$	$\hat{\boldsymbol{\tau}}^{i}(\boldsymbol{\xi})$
	$\hat{\boldsymbol{\varepsilon}}^{i+1}(\boldsymbol{\xi}) = \hat{\boldsymbol{\varepsilon}}^{i} - \hat{\boldsymbol{\Gamma}}(\boldsymbol{\xi}): \hat{\boldsymbol{\tau}}^{i}(\boldsymbol{\xi})$
$\boldsymbol{\varepsilon}^{\boldsymbol{i+1}}(\boldsymbol{x})$	$\hat{\boldsymbol{\varepsilon}}^{i+1}(0) = \bar{\boldsymbol{\varepsilon}}$

Table A0.1. FFT fixed-point iterative solution scheme

The iteration is completed until the convergence of the strain tensor.

Conclusions

In this thesis, four Physically Informed Data Science methods have been presented to model the mechanistic relationship in the process-structure-property paradigm of advanced materials. First, the main methodologies that combine physical knowledge with data science methods have been introduced and a uniform taxonomy has been proposed. In the second Chapter, a data-driven method to characterize the mechanical response of heterogeneous materials with a model-free approach is described. A PINN with a modified architecture has been designed to learn the macroscale constitutive model of heterogeneous materials from the distributed strain measured with the DIC. The method complies with the governing equations of energy balance and force equilibrium while preserving the strain convexity and constitutive symmetry. A data reduction method based on the k-means clustering algorithm is introduced to reduce the computational cost of the model training while filtering the noise in the experimental observation. The method has been first tested on artificial data of an off-axis tensile test of an elastic orthotropic material simulated with a FEM, which demonstrated the ability of the method to learn all the elastic constants of the orthotropic constitutive equation with a single test. A linear and a cubic continuum damage law have been introduced in the FEM to assess the ability of the method to learn the nonlinear material response. Finally, the distributed strain measured during tensile tests of carbon fibre woven reinforced epoxy has been used to test the method, which efficiently learns the nonlinear shear response of the composite material. The damage characterized with the PINN is compared to the strain maps of the specimen, revealing a remarkable accuracy in the identification of the damaged zone with the reduced dataset. In the third Chapter, the reconstructed microstructure of a fibre-reinforced composite obtained with microCT analysis is processed together with the DIC data to calibrate the mechanical properties of the composite constituents accounting for the manufacturing-induced defectiveness. The microstructure data fed a multiscale model based on the FFT method, whose results are statistically compared with the DIC measurements, and the parameters of the multiscale models are calibrated with an optimization procedure. As a result, a microscale representation of the FRP is calibrated, which presents a variable microstructure defined with the microCT analysis and the variable material properties defined with the optimization procedure, defined as a Stochastic Volume Element (SVE). A multiscale model of a FRP part is developed using the SVE and the buckling response has been investigated, comparing the results of the method with a standard hierarchical multiscale approach. The results of the virtual case study revealed that the material uncertainty could propagate to the part scale and induce a structural response that cannot be predicted with standard procedure, which is reflected in a 20 to 30% reduction of the maximum bearing load. In Chapter 4, a data-driven method to predict the crushing response of origami-shaped composite structures is presented, moving from the material scale to a structural application. A physic-informed model is trained on simulation results generated with a FEM model, previously calibrated with experimental tests, to assess the absorbed energy and the crushing force of a modular origami-shaped tube, while preserving the physical constraints between the energy balance and the crushing force. Being the full structure composed of two axially stacked submodules with different geometries, the PINN can predict the response of the crash box by elaborating the crushing response of the single submodules, substantially reducing the computational cost. The efficient surrogate model has been used to optimize the tube geometry by rapidly exploring the design space with the PINN to define the configuration with the highest absorbed energy. The response of the optimized structures has been simulated with the FEM, showing a remarkable accuracy while yielding a consistent time reduction (i.e., 30 times faster) when compared with FEM-based optimization. In the last Chapter, the fatigue response of the aluminium alloy manufactured with the AM technology is modelled using a neural network designed to mimic the Murakami models that link the fatigue strength with the material microstructure and its defectiveness. The proposed MDS model assesses the fatigue response from the main manufacturing parameters of the SLM process, intending to reduce the experimental test necessary to methodically explore the correlation between the process parameters and the material strength under cyclic loads. The method learns the process-properties relationship by combining the predictive capability of the neural networks with the physic knowledge about the defect and microstructure effect on the fatigue response, which is embedded in the model through a custom architecture of the neural network. The results show the ability of the method to establish a relation between the processing conditions and the resultant fatigue strength with an overall good accuracy, efficiently predicting the effect of the SLM parameters on the material response. The method has been tested on a validation dataset and compared with standard NN, showing a superior accuracy of the predictions and a remarkable extrapolation capability outside the training domain.

The goal of this work was to explore the capabilities of the data science methods to model mechanical engineering phenomena in the field of advanced materials, where the traditional approaches are continuously evolving to keep pace with increasing complexity. Beyond the established machine learning models, physic-based data-driven models can enhance the predictive capabilities while constraining the fundamental principles of the mechanics through modified training schemes, custom architectures, or hybrid approaches. Following the fundamental steps of the MDS, a framework should be specifically designed for the modelled phenomenon, defining mechanistic relevant quantities from the data, designing the preprocessing pipeline, defining the mechanistic knowledge to bring in the picture and developing the machine learning architecture that can efficiently predict the quantity of interest. Furthermore, this work wanted to apply data-driven approaches with experimental data to overcome the common material characterization and model calibration approaches, demonstrating the advantages of these methods when abundant experimental observations are available. In conclusion, the results obtained in this thesis have demonstrated the potential for the application of data-driven methods in the characterization and modelling of advanced materials (e.g., composites and AMed metals) when combined with the knowledge about governing physics. More work should be done in the development of the method to overcome the limitations in terms of extrapolation predictivity outside the training domain, universal applicability to similar yet different materials or structures (e.g., transfer learning and mesh-based methods), uncertainty quantification and model explainability (e.g., probabilistic machine learning models and explainable architectures), and method integration into common engineering tools (e.g., PINN material model integrated into FEM, PINN structure surrogate integrated into assembly models).

References

[1] T. Hey, S. Tansley, K. Tolle, The Fourth Paradigm: Data-Intensive Scientific Discovery, 2009. https://www.microsoft.com/en-us/research/publication/fourth-paradigm-data-intensive-scientific-discovery/ (accessed January 10, 2023).

[2] W.K. Liu, Z. Gan, M. Fleming, Mechanistic Data Science for STEM Education and Applications, Springer International Publishing, Cham, 2021. https://doi.org/10.1007/978-3-030-87832-0.

[3] S. Lo Piano, Ethical principles in machine learning and artificial intelligence: cases from the field and possible ways forward, Humanities and Social Sciences Communications 2020 7:1. 7 (2020) 1–7. https://doi.org/10.1057/s41599-020-0501-9.

[4] T. Miller, Explanation in artificial intelligence: Insights from the social sciences, Artif Intell. 267 (2019) 1–38. https://doi.org/10.1016/J.ARTINT.2018.07.007.

[5] J. Grimmer, M.E. Roberts, B.M. Stewart, Machine Learning for Social Science: An Agnostic Approach, Annual Review of Political Science. 24 (2021) 395–419. https://doi.org/10.1146/ANNUREV-POLISCI-053119-015921.

[6] E.J. Topol, High-performance medicine: the convergence of human and artificial intelligence, Nature Medicine 2019 25:1. 25 (2019) 44–56. https://doi.org/10.1038/s41591-018-0300-7.

[7] J. He, S.L. Baxter, J. Xu, J. Xu, X. Zhou, K. Zhang, The practical implementation of artificial intelligence technologies in medicine, Nature Medicine 2019 25:1. 25 (2019) 30–36. https://doi.org/10.1038/s41591-018-0307-0.

[8] W. Raghupathi, V. Raghupathi, Big data analytics in healthcare: promise and potential, Health Inf Sci Syst. 2 (2014) 1–10. https://doi.org/10.1186/2047-2501-2-3.

[9] C. Sommer, D.W. Gerlich, Machine learning in cell biology-teaching computers to recognize phenotypes, J Cell Sci. 126 (2013) 5529–5539. https://doi.org/10.1242/JCS.123604/263567/AM/MACHINE-LEARNING-IN-CELL-BIOLOGY-TEACHING.

[10] M. Zitnik, F. Nguyen, B. Wang, J. Leskovec, A. Goldenberg, M.M. Hoffman, Machine learning for integrating data in biology and medicine: Principles, practice, and opportunities, Information Fusion. 50 (2019) 71–91. https://doi.org/10.1016/J.INFFUS.2018.09.012.

[11] A.L. Tarca, V.J. Carey, X. wen Chen, R. Romero, S. Drăghici, Machine Learning and Its Applications to Biology, PLoS Comput Biol. 3 (2007) e116. https://doi.org/10.1371/JOURNAL.PCBI.0030116.

[12] G. Russo, P. Reche, M. Pennisi, F. Pappalardo, The combination of artificial intelligence and systems biology for intelligent vaccine design, Expert Opin Drug Discov. 15 (2020) 1267–1281. https://doi.org/10.1080/17460441.2020.1791076.

[13] D.T. Jones, Setting the standards for machine learning in biology, Nature Reviews Molecular Cell Biology 2019 20:11. 20 (2019) 659–660. https://doi.org/10.1038/s41580-019-0176-5.

[14] S.P. Xiao, T. Belytschko, A bridging domain method for coupling continua with molecular dynamics, Comput Methods Appl Mech Eng. 193 (2004) 1645–1669. https://doi.org/10.1016/J.CMA.2003.12.053.

[15] S. Saha, Z. Gan, L. Cheng, J. Gao, O.L. Kafka, X. Xie, H. Li, M. Tajdari, H.A. Kim, W.K. Liu, Hierarchical Deep Learning Neural Network (HiDeNN): An artificial intelligence (AI) framework for computational science and engineering, Comput Methods Appl Mech Eng. 373 (2021) 113452. https://doi.org/10.1016/j.cma.2020.113452.

[16] K. Fukushima, Cognitron: A self-organizing multilayered neural network, Biol Cybern. 20 (1975) 121–136. https://doi.org/10.1007/BF00342633/METRICS.

[17] G. Klambauer, T. Unterthiner, A. Mayr, S. Hochreiter, Self-Normalizing Neural Networks, Adv Neural Inf Process Syst. 2017-December (2017) 972–981. https://doi.org/10.48550/arxiv.1706.02515.

[18] A. Gholamy, V. Kreinovich, O. Kosheleva, Why 70/30 or 80/20 Relation Between Training and Testing Sets : A Pedagogical Explanation, Departmental Technical Reports (CS). 1209 (2018) 1–6.

[19] D.E. Rumelhart, G.E. Hinton, R.J. Williams, Learning representations by back-propagating errors, Nature 1986 323:6088. 323 (1986) 533–536. https://doi.org/10.1038/323533a0.

[20] D.P. Kingma, J.L. Ba, Adam: A Method for Stochastic Optimization, 3rd International Conference on Learning Representations, ICLR 2015 - Conference Track Proceedings. (2014). https://doi.org/10.48550/arxiv.1412.6980.

[21] J. Duchi JDUCHI, Y. Singer, Adaptive Subgradient Methods for Online Learning and Stochastic Optimization * Elad Hazan, Journal of Machine Learning Research. 12 (2011) 2121–2159.

[22] J. Kiefer, J. Wolfowitz, Stochastic Estimation of the Maximum of a Regression Function, Https://Doi.Org/10.1214/Aoms/1177729392. 23 (1952) 462–466. https://doi.org/10.1214/AOMS/1177729392.

[23] X. Liu, S. Tian, F. Tao, H. Du, W. Yu, Machine learning-assisted modeling of composite materials and structures: a review, (2021) 1–21. https://doi.org/10.2514/6.2021-2023.

[24] I.B.C.M. Rocha, P. Kerfriden, F.P. van der Meer, On-the-fly construction of surrogate constitutive models for concurrent multiscale mechanical analysis through probabilistic machine learning, Journal of Computational Physics: X. 9 (2021) 100083. https://doi.org/10.1016/j.jcpx.2020.100083.

[25] D.W. Abueidda, S. Koric, N.A. Sobh, H. Sehitoglu, Deep learning for plasticity and thermo-viscoplasticity, Int J Plast. 136 (2021) 102852. https://doi.org/10.1016/j.ijplas.2020.102852.

[26] I.B.C.M. Rocha, P. Kerfriden, F.P. van der Meer, Micromechanics-based surrogate models for the response of composites: A critical comparison between a classical mesoscale constitutive model, hyper-reduction and neural networks, European Journal of Mechanics, A/Solids. 82 (2020) 103995. https://doi.org/10.1016/j.euromechsol.2020.103995.

[27] H. El Kadi, Modeling the mechanical behavior of fiber-reinforced polymeric composite materials using artificial neural networks-A review, (2005). https://doi.org/10.1016/j.compstruct.2005.01.020.

[28] S. Yan, X. Zou, M. Ilkhani, A. Jones, An efficient multiscale surrogate modelling framework for composite materials considering progressive damage based on artificial neural networks, Composites Part B. 194 (2020) 108014. https://doi.org/10.1016/j.compositesb.2020.108014.

[29] A. Bhaduri, A. Gupta, L. Graham-Brady, Stress field prediction in fiber-reinforced composite materials using a deep learning approach, Compos B Eng. 238 (2022) 109879. https://doi.org/10.1016/J.COMPOSITESB.2022.109879.

[30] J. Li, Z. Yang, G. Qian, F. Berto, Machine learning based very-high-cycle fatigue life prediction of Ti-6Al-4V alloy fabricated by selective laser melting, Int J Fatigue. 158 (2022) 106764. https://doi.org/10.1016/j.ijfatigue.2022.106764.

[31] L. Gan, H. Wu, Z. Zhong, On the use of data-driven machine learning for remaining life estimation of metallic materials based on Ye-Wang damage theory, Int J Fatigue. 156 (2022) 106666. https://doi.org/10.1016/j.ijfatigue.2021.106666.

[32] E. Maleki, S. Bagherifard, S.M.J. Razavi, M. Bandini, A. du Plessis, F. Berto, M. Guagliano, On the efficiency of machine learning for fatigue assessment of post-processed additively manufactured

AlSi10Mg, Int J Fatigue. 160 (2022) 106841. https://doi.org/10.1016/j.ijfatigue.2022.106841.

[33] Z. Zhan, H. Li, A novel approach based on the elastoplastic fatigue damage and machine learning models for life prediction of aerospace alloy parts fabricated by additive manufacturing, Int J Fatigue. 145 (2021) 106089. https://doi.org/10.1016/J.IJFATIGUE.2020.106089.

[34] J. Reiner, R. Vaziri, N. Zobeiry, Machine Learning Assisted Characterisation and Simulation of Compressive Damage in Composite Laminates, Compos Struct. (2021). https://doi.org/10.1016/j.compstruct.2021.114290.

[35] N. Zobeiry, J. Reiner, R. Vaziri, Theory-guided machine learning for damage characterization of composites, Compos Struct. 246 (2020) 112407. https://doi.org/10.1016/j.compstruct.2020.112407.

[36] X. Liu, F. Tao, H. Du, W. Yu, K. Xu, Learning Nonlinear Constitutive Laws Using Neural Network Models Based on Indirectly Measurable Data, J Appl Mech. 87 (2020). https://doi.org/10.1115/1.4047036.

[37] Z. Liu, M.A. Bessa, W.K. Liu, Self-consistent clustering analysis: An efficient multi-scale scheme for inelastic heterogeneous materials, Comput Methods Appl Mech Eng. 306 (2016) 319–341. https://doi.org/10.1016/j.cma.2016.04.004.

[38] Z. Liu, M. Fleming, W.K. Liu, Microstructural material database for self-consistent clustering analysis of elastoplastic strain softening materials, Comput. Methods Appl. Mech. Engrg. 330 (2018) 547–577. https://doi.org/10.1016/j.cma.2017.11.005.

[39] K. Xu, D.Z. Huang, E. Darve, Learning constitutive relations using symmetric positive definite neural networks, J Comput Phys. 428 (2021). https://doi.org/10.1016/j.jcp.2020.110072.

[40] Z. Liu, Cell division in deep material networks applied to multiscale strain localization modeling, (2021). http://arxiv.org/abs/2101.07226.

[41] Z. Liu, Progresses in deep material networks and materials design, (2019).

[42] N.N. Vlassis, W. Sun, Geometric learning for computational mechanics Part II: Graph embedding for interpretable multiscale plasticity, Comput Methods Appl Mech Eng. 404 (2023) 115768. https://doi.org/10.1016/J.CMA.2022.115768.

[43] N.N. Vlassis, R. Ma, W.C. Sun, Geometric deep learning for computational mechanics Part I: anisotropic hyperelasticity, Comput Methods Appl Mech Eng. 371 (2020). https://doi.org/10.1016/J.CMA.2020.113299.

[44] M. Maurizi, C. Gao, F. Berto, Predicting stress, strain and deformation fields in materials and structures with graph neural networks, Sci Rep. 12 (2022). https://doi.org/10.1038/S41598-022-26424-3.

[45] L. Zhang, L. Cheng, H. Li, J. Gao, C. Yu, R. Domel, Y. Yang, S. Tang, W.K. Liu, Hierarchical deep-learning neural networks: finite elements and beyond, Comput Mech. 67 (2020) 207–230. https://doi.org/10.1007/s00466-020-01928-9.

[46] M. Raissi, P. Perdikaris, G.E. Karniadakis, Physics-informed neural networks: A deep learning framework for solving forward and inverse problems involving nonlinear partial differential equations, J Comput Phys. 378 (2019) 686–707. https://doi.org/10.1016/J.JCP.2018.10.045.

[47] J. Chen, Y. Liu, Fatigue property prediction of additively manufactured Ti-6Al-4V using probabilistic physics-guided learning, Addit Manuf. 39 (2021) 101876. https://doi.org/10.1016/J.ADDMA.2021.101876.

[48] E. Haghighat, M. Raissi, A. Moure, H. Gomez, R. Juanes, A physics-informed deep learning framework for inversion and surrogate modeling in solid mechanics, Comput Methods Appl Mech Eng. 379 (2021) 113741. https://doi.org/10.1016/J.CMA.2021.113741.

[49] A. Henkes, H. Wessels, R. Mahnken, Physics informed neural networks for continuum micromechanics, Comput Methods Appl Mech Eng. 393 (2022) 114790. https://doi.org/10.1016/J.CMA.2022.114790.

[50] F. Pierron, M. Grediac, The virtual fields method: Extracting constitutive mechanical parameters from full-field deformation measurements, The Virtual Fields Method: Extracting Constitutive Mechanical Parameters from Full-Field Deformation Measurements. 9781461418245 (2012) 1–517. https://doi.org/10.1007/978-1-4614-1824-5/COVER.

[51] S. Avril, M. Bonnet, A.S. Bretelle, M. Grediac, F. Hild, P. Ienny, F. Latourte, D. Lemosse, S. Pagano, E. Pagnacco, A. Stéphane, A.-S. Bretelle, Overview of identification methods of mechanical parameters based on full-field measurements, (2008). https://hal.science/hal-00274639v1 (accessed February 8, 2023).

[52] D. Lecompte, A. Smits, H. Sol, J. Vantomme, D. Van Hemelrijck, Mixed numerical–experimental technique for orthotropic parameter identification using biaxial tensile tests on cruciform specimens, Int J Solids Struct. 44 (2007) 1643–1656. https://doi.org/10.1016/J.IJSOLSTR.2006.06.050.

[53] K. Hornik, M. Stinchcombe, H. White, Multilayer feedforward networks are universal approximators, Neural Networks. 2 (1989) 359–366. https://doi.org/10.1016/0893-6080(89)90020-8.

[54] S. Jung, J. Ghaboussi, Neural network constitutive model for rate-dependent materials, Comput Struct. 84 (2006) 955–963. https://doi.org/10.1016/J.COMPSTRUC.2006.02.015.

[55] Y.M.A. Hashash, S. Jung, J. Ghaboussi, Numerical implementation of a neural network based material model in finite element analysis, Int J Numer Methods Eng. 59 (2004) 989–1005. https://doi.org/10.1002/NME.905.

[56] J. Ghaboussi, J.H. Garrett, X. Wu, Knowledge-Based Modeling of Material Behavior with Neural Networks, J Eng Mech. 117 (1991) 132–153. https://doi.org/10.1061/(ASCE)0733-9399(1991)117:1(132).

[57] Y. Shen, K. Chandrashekhara, W.F. Breig, L.R. Oliver, Finite element analysis of V-ribbed belts using neural network based hyperelastic

material model, Int J Non Linear Mech. 40 (2005) 875–890. https://doi.org/10.1016/J.IJNONLINMEC.2004.10.005.

[58] B.A. Le, J. Yvonnet, Q.C. He, Computational homogenization of nonlinear elastic materials using neural networks, Int J Numer Methods Eng. 104 (2015) 1061–1084. https://doi.org/10.1002/NME.4953.

[59] J. Ling, R. Jones, J. Templeton, Machine learning strategies for systems with invariance properties, J Comput Phys. 318 (2016) 22–35. https://doi.org/10.1016/J.JCP.2016.05.003.

[60] T. Furukawa, G. Yagawa, Implicit constitutive modelling for viscoplasticity using neural networks, Int J Numer Methods Eng. 43 (1998) 195–219. https://doi.org/10.1002/(SICI)1097-0207(19980930)43:2<195::AID-NME418>3.0.CO;2-6.

[61] K. Wang, W.C. Sun, A multiscale multi-permeability poroplasticity model linked by recursive homogenizations and deep learning, Comput Methods Appl Mech Eng. 334 (2018) 337–380. https://doi.org/10.1016/J.CMA.2018.01.036.

[62] D.Z. Huang, K. Xu, C. Farhat, E. Darve, Learning constitutive relations from indirect observations using deep neural networks, J Comput Phys. 416 (2020) 109491. https://linkinghub.elsevier.com/retrieve/pii/S0021999120302655 (accessed March 6, 2023).

[63] X. Liu, F. Tao, H. Du, W. Yu, K. Xu, Learning Nonlinear Constitutive Laws Using Neural Network Models Based on Indirectly Measurable Data, J Appl Mech. 87 (2020) 1–8. https://doi.org/10.1115/1.4047036.

[64] X. Liu, F. Tao, W. Yu, A neural network enhanced system for learning nonlinear constitutive law and failure initiation criterion of composites using indirectly measurable data, (2020). https://doi.org/10.1016/j.compstruct.2020.112658.

[65] M. Liu, L. Liang, W. Sun, A generic physics-informed neural network-based constitutive model for soft biological tissues, Comput

Methods Appl Mech Eng. 372 (2020) 113402. https://doi.org/10.1016/J.CMA.2020.113402.

[66] E. Zhang, M. Dao, G.E. Karniadakis, S. Suresh, Analyses of internal structures and defects in materials using physics-informed neural networks, Sci Adv. 8 (2022) 644. https://doi.org/10.1126/SCIADV.ABK0644.

[67] H.T. Hahn, S.W. Tsai, Nonlinear Elastic Behavior of Unidirectional Composite Laminae, J Compos Mater. 7 (1973) 102–118. https://doi.org/10.1177/002199837300700108.

[68] H. Schreier, J.J. Orteu, M.A. Sutton, Image correlation for shape, motion and deformation measurements: Basic concepts, theory and applications, Springer US, 2009. https://doi.org/10.1007/978-0-387-78747-3.

[69] X. Glorot, Y. Bengio, Understanding the difficulty of training deep feedforward neural networks, (2010) 249–256. https://proceedings.mlr.press/v9/glorot10a.html (accessed April 28, 2023).

[70] D. Van Hemelrijck, A. Makris, C. Ramault, E. Lamkanfi, W. Van Paepegem, D. Lecompte, Biaxial testing of fibre-reinforced composite laminates, (2008). https://doi.org/10.1243/14644207JMDA199.

[71] C. McVeigh, F. Vernerey, W.K. Liu, L. Cate Brinson, Multiresolution analysis for material design, Comput Methods Appl Mech Eng. 195 (2006) 5053–5076. https://doi.org/10.1016/J.CMA.2005.07.027.

[72] D.K. Patel, A.M. Waas, Multiscale analysis of notched fiber reinforced laminates, Compos B Eng. 173 (2019) 106986. https://doi.org/10.1016/J.COMPOSITESB.2019.106986.

[73] S.Z.H. Shah, P.S.M. Megat-Yusoff, S. Karuppanan, R.S. Choudhry, Z. Sajid, Multiscale damage modelling of 3D woven composites under static and impact loads, Compos Part A Appl Sci Manuf. 151 (2021) 106659. https://doi.org/10.1016/J.COMPOSITESA.2021.106659.

[74] B. Koohbor, S. Ravindran, A. Kidane, A multiscale experimental approach for correlating global and local deformation response in woven composites, Compos Struct. 194 (2018) 328–334. https://doi.org/10.1016/J.COMPSTRUCT.2018.04.016.

[75] E. Tikarrouchine, A. Benaarbia, G. Chatzigeorgiou, F. Meraghni, Non-linear FE2 multiscale simulation of damage, micro and macroscopic strains in polyamide 66-woven composite structures: Analysis and experimental validation, Compos Struct. 255 (2021) 112926. https://doi.org/10.1016/J.COMPSTRUCT.2020.112926.

[76] J. Chevalier, P.P. Camanho, F. Lani, T. Pardoen, Multi-scale characterization and modelling of the transverse compression response of unidirectional carbon fiber reinforced epoxy, (2018). https://doi.org/10.1016/j.compstruct.2018.10.076.

[77] J. Fish, Practical multiscaling, 2013. http://link.springer.com/10.1007/978-94-009-3489-4.

[78] C.T. Sun, R.S. Vaidya, Prediction of composite properties from a representative volume element, Compos Sci Technol. 56 (1996) 171–179. https://doi.org/10.1016/0266-3538(95)00141-7.

[79] D. Cule, S. Torquato, Generating random media from limited microstructural information via stochastic optimization, J Appl Phys. 86 (1999) 3428. https://doi.org/10.1063/1.371225.

[80] M. Li, S. Ghosh, O. Richmond, H. Weiland, T.N. Rouns, Three dimensional characterization and modeling of particle reinforced metal matrix composites: part I: Quantitative description of microstructural morphology, Materials Science and Engineering: A. 265 (1999) 153–173. https://doi.org/10.1016/S0921-5093(98)01132-0.

[81] S. Sankaran, N. Zabaras, Computing property variability of polycrystals induced by grain size and orientation uncertainties, Acta Mater. 55 (2007) 2279–2290. https://doi.org/10.1016/J.ACTAMAT.2006.11.025.

[82] A.A. Al-Ostaz Anipindi Diwakar AE Khalid I Alzebdeh, Statistical model for characterizing random microstructure of inclusion-matrix composites, (n.d.). https://doi.org/10.1007/s10853-006-1117-1.

[83] G. Kamgaing Somoh, R. Ben Toumi, J. Renard, M. Monin, Statistical approach of elastic properties of continuous fiber composite, Compos Struct. 119 (2015) 287–297. https://doi.org/10.1016/J.COMPSTRUCT.2014.08.039.

[84] H.J. Lim, H. Choi, G.J. Yun, Multiscale failure and damage analysis of sheet molding compound (SMC) composites using Micro-CT image-based reconstruction model, Compos B Eng. 231 (2022) 109593. https://doi.org/10.1016/J.COMPOSITESB.2021.109593.

[85] T. Huang, J. Gao, Q. Sun, D. Zeng, X. Su, W. Kam Liu, W. Chen, Stochastic nonlinear analysis of unidirectional fiber composites using image-based microstructural uncertainty quantification, Compos Struct. 260 (2021) 113470. https://doi.org/10.1016/j.compstruct.2020.113470.

[86] X. Yin, W. Chen, A. To, C. McVeigh, W.K. Liu, Statistical volume element method for predicting microstructure–constitutive property relations, Comput Methods Appl Mech Eng. 197 (2008) 3516–3529. https://doi.org/10.1016/J.CMA.2008.01.008.

[87] Y.Y. Li, J.Z. Cui, The multi-scale computational method for the mechanics parameters of the materials with random distribution of multi-scale grains, Compos Sci Technol. 65 (2005) 1447–1458. https://doi.org/10.1016/J.COMPSCITECH.2004.12.016.

[88] B. Wang, G. Fang, H. Wang, J. Liang, F. Dai, S. Meng, Uncertainty modelling and multiscale simulation of woven composite twisted structure, Compos Sci Technol. 217 (2022) 109118. https://doi.org/10.1016/J.COMPSCITECH.2021.109118.

[89] W. Tao, P. Zhu, C. Xu, Z. Liu, Uncertainty quantification of mechanical properties for three-dimensional orthogonal woven composites. Part II: Multiscale simulation, Compos Struct. 235 (2020) 111764. https://doi.org/10.1016/J.COMPSTRUCT.2019.111764.

[90] M. Vinot, C. Liebold, T. Usta, M. Holzapfel, N. Toso, H. Voggenreiter, Stochastic modelling of continuous glass-fibre reinforced plastics–considering material uncertainty in microscale simulations, J Compos Mater. 2022 (2022) 1–13. https://doi.org/10.1177/00219983221139790/ASSET/IMAGES/LARGE/10.1177_00219983221139790-FIG14.JPEG.

[91] S.L. Gao, E. Mäder, Characterisation of interphase nanoscale property variations in glass fibre reinforced polypropylene and epoxy resin composites, Compos Part A Appl Sci Manuf. 33 (2002) 559–576. https://doi.org/10.1016/S1359-835X(01)00134-8.

[92] M.R. Vanlandingham, R.R. Dagastine, R.F. Eduljee, R.L. McCullough, J.W. Gillespie, Characterization of nanoscale property variations in polymer composite systems: 1. Experimental results, Compos Part A Appl Sci Manuf. 30 (1999) 75–83. https://doi.org/10.1016/S1359-835X(98)00098-0.

[93] M. Hardiman, T.J. Vaughan, C.T. McCarthy, Fibrous composite matrix characterisation using nanoindentation: The effect of fibre constraint and the evolution from bulk to in-situ matrix properties, Compos Part A Appl Sci Manuf. 68 (2015) 296–303. https://doi.org/10.1016/J.COMPOSITESA.2014.09.022.

[94] A. Bahrami, X. Morelle, L.D. Hông Minh, T. Pardoen, C. Bailly, B. Nysten, Curing dependent spatial heterogeneity of mechanical response in epoxy resins revealed by atomic force microscopy, Polymer (Guildf). 68 (2015) 1–10. https://doi.org/10.1016/J.POLYMER.2015.04.084.

[95] B. Koohbor, S. Ravindran, A. Kidane, Experimental determination of Representative Volume Element (RVE) size in woven composites, Opt Lasers Eng. 90 (2017) 59–71. https://doi.org/10.1016/j.optlaseng.2016.10.001.

[96] B. Koohbor, C.B. Montgomery, N.R. Sottos, Identification of RVE length scale in fiber composites via combined optical and SEM digital image correlation, Compos Sci Technol. 227 (2022) 109613. https://doi.org/10.1016/J.COMPSCITECH.2022.109613.

[97] A. Ciampaglia, Data driven statistical method for the multiscale characterization and modelling of fiber reinforced composites, Compos Struct. 320 (2023) 117215. https://doi.org/10.1016/J.COMPSTRUCT.2023.117215.

[98] F.J. Massey, The Kolmogorov-Smirnov Test for Goodness of Fit, Source: Journal of the American Statistical Association. 46 (1951) 68–78.

[99] VGSTUDIO MAX High-End Industrial CT Software, (n.d.). www.volumegraphics.com/en/frost (accessed June 21, 2023).

[100] A.A. Gusev, Representative volume element size for elastic composites: A numerical study, J Mech Phys Solids. 45 (1997) 1449–1459. https://doi.org/10.1016/S0022-5096(97)00016-1.

[101] D. Ivanov, S. Ivanov, S. Lomov, I. Verpoest, Strain mapping analysis of textile composites, Opt Lasers Eng. 47 (2009) 360–370. https://doi.org/10.1016/J.OPTLASENG.2008.05.013.

[102] D.S. Ivanov, S. V. Lomov, S.G. Ivanov, I. Verpoest, Stress distribution in outer and inner plies of textile laminates and novel boundary conditions for unit cell analysis, Compos Part A Appl Sci Manuf. 41 (2010) 571–580. https://doi.org/10.1016/j.compositesa.2010.01.004.

[103] A. Kaddour, M. Hinton, Input data for test cases used in benchmarking triaxial failure theories of composites, J Compos Mater. 46 (2012) 2295–2312. https://doi.org/10.1177/0021998312449886.

[104] F.J. Massey, The Kolmogorov-Smirnov Test for Goodness of Fit, Source: Journal of the American Statistical Association. 46 (1951) 68–78.

[105] R.H. Byrd, M.E. Hribar, J. Nocedal, An Interior Point Algorithm for Large-Scale Nonlinear Programming, Https://Doi.Org/10.1137/S1052623497325107. 9 (2006) 877–900. https://doi.org/10.1137/S1052623497325107.

[106] S. Boria, A. Scattina, G. Belingardi, Experimental evaluation of a fully recyclable thermoplastic composite, Compos Struct. 140 (2016) 21–35. https://doi.org/10.1016/J.COMPSTRUCT.2015.12.049.

[107] S. Boria, A. Scattina, G. Belingardi, Axial energy absorption of CFRP truncated cones, Compos Struct. 130 (2015) 18–28. https://doi.org/10.1016/J.COMPSTRUCT.2015.04.026.

[108] S. Boria, G. Belingardi, D. Fiumarella, A. Scattina, Experimental crushing analysis of thermoplastic and hybrid composites, Compos Struct. 226 (2019) 111241. https://doi.org/10.1016/j.compstruct.2019.111241.

[109] J. Ma, Z. You, A Novel Origami Crash Box With Varying Profiles, Proceedings of the ASME Design Engineering Technical Conference. 6 B (2014). https://doi.org/10.1115/DETC2013-13495.

[110] X. ZHAO, Y. HU, I. HAGIWARA, Shape Optimization to Improve Energy Absorption Ability of Cylindrical Thin-Walled Origami Structure, Journal of Computational Science and Technology. 5 (2011) 148–162. https://doi.org/10.1299/JCST.5.148.

[111] Y. Li, Z. You, Origami concave tubes for energy absorption, Int J Solids Struct. 169 (2019) 21–40. https://doi.org/10.1016/J.IJSOLSTR.2019.03.026.

[112] C. Zhou, Y. Zhou, B. Wang, Crashworthiness design for trapezoid origami crash boxes, Thin-Walled Structures. 117 (2017) 257–267. https://doi.org/10.1016/J.TWS.2017.03.022.

[113] H. Ye, J. Ma, X. Zhou, H. Wang, Z. You, Energy absorption behaviors of pre-folded composite tubes with the full-diamond origami patterns, Compos Struct. 221 (2019) 110904. https://doi.org/10.1016/J.COMPSTRUCT.2019.110904.

[114] M. Boreanaz, G. Belingardi, C.D.F. Maia, Application of the origami shape in the development of automotive crash box, Material Design & Processing Communications. 2 (2020) e181. https://doi.org/10.1002/MDP2.181.

[115] J. Wu, Y. Zhang, K. Li, L. Su, Origami-inspired metamaterials hierarchical structure with tailorable crushing behavior, Constr Build Mater. 345 (2022) 128328. https://doi.org/10.1016/J.CONBUILDMAT.2022.128328.

[116] H. Ye, X. Zhou, J. Ma, H. Wang, Z. You, Axial crushing behaviors of composite pre-folded tubes made of KFRP/CFRP hybrid laminates, Thin-Walled Structures. 149 (2020) 106649. https://doi.org/10.1016/J.TWS.2020.106649.

[117] J. Ma, S. Chai, Y. Chen, Geometric design, deformation mode, and energy absorption of patterned thin-walled structures, Mechanics of Materials. 168 (2022) 104269. https://doi.org/10.1016/J.MECHMAT.2022.104269.

[118] H. Baler, Ill-posed problems in structural optimization and their practical consequences, Springer-Verlag, 1994.

[119] J. Hadamard, Sur les problèmes aux dérivées partielles et leur signification physique, Princeton Univ. Bull. 13 (1902) 49–52.

[120] S. Hou, Q. Li, S. Long, X. Yang, W. Li, Design optimization of regular hexagonal thin-walled columns with crashworthiness criteria, Finite Elements in Analysis and Design. 43 (2007) 555–565. https://doi.org/10.1016/J.FINEL.2006.12.008.

[121] M. Avalle, G. Chiandussi, G. Belingardi, Design optimization by response surface methodology: application to crashworthiness design of vehicle structures, (n.d.). https://doi.org/10.1007/s00158-002-0243-x.

[122] E. Raponi, D. Fiumarella, S. Boria, A. Scattina, G. Belingardi, Methodology for parameter identification on a thermoplastic composite crash absorber by the Sequential Response Surface Method and Efficient Global Optimization, Compos Struct. 278 (2021) 114646. https://doi.org/10.1016/j.compstruct.2021.114646.

[123] D. Fiumarella, E. Raponi, EXPERIMENTAL ANALYSIS AND NUMERICAL OPTIMIZATION OF A THERMOPLASTIC COMPOSITE IN CRASHWORTHINESS, (2020).

[124] J.P. Dias, R.N. Cadete, M.S. Pereira, Optimization in vehicle crashworthiness design using surrogate models COST TU1101 View project 6 th World Congresses of Structural and Multidisciplinary Optimization Optimization in vehicle crashworthiness design using surrogate models, in: 2005. https://www.researchgate.net/publication/250092920 (accessed December 15, 2022).

[125] E. Sakaridis, N. Karathanasopoulos, D. Mohr, Machine-learning based prediction of crash response of tubular structures, Int J Impact Eng. 166 (2022) 104240. https://doi.org/10.1016/J.IJIMPENG.2022.104240.

[126] P. Zhang, Z. Sun, H. Wang, X. Xiang, Performance Study of Origami Crash Tubes Based on Energy Dissipation History, Energies (Basel). 15 (2022). https://doi.org/10.3390/en15093109.

[127] A. Ciampaglia, D. Fiumarella, C. Boursier Niutta, R. Ciardiello, G. Belingardi, Impact response of an origami-shaped composite cras hbox: experimental analysis and numerical optimization, Compos Struct. 256 (2020) 113093. https://doi.org/10.1016/j.compstruct.2020.113093.

[128] ASTM International, Astm D3410-03, 08 (n.d.) 1–16.

[129] A. International, ASTM 5379: Standard Test Method for Shear Properties of Composite Materials by the V-Notched, Annual Book of ASTM Standards. (2011) 1–13.

[130] I. Nemeth, Standard Test Method for Tensile Properties of Polymer Matrix Composite Materials, (n.d.).

[131] Y. Heider, K. Wang, W.C. Sun, SO(3)-invariance of informed-graph-based deep neural network for anisotropic elastoplastic materials, Comput Methods Appl Mech Eng. 363 (2020) 112875. https://doi.org/10.1016/J.CMA.2020.112875.

[132] A. Yadollahi, N. Shamsaei, Additive manufacturing of fatigue resistant materials: Challenges and opportunities, Int J Fatigue. 98 (2017) 14–31. https://doi.org/10.1016/j.ijfatigue.2017.01.001.

[133] Y. Murakami, H. Masuo, Y. Tanaka, M. Nakatani, Defect Analysis for Additively Manufactured Materials in Fatigue from the Viewpoint of Quality Control and Statistics of Extremes, Procedia Structural Integrity. 19 (2019) 113–122. https://doi.org/10.1016/j.prostr.2019.12.014.

[134] R. Molaei, A. Fatemi, Fatigue Design with Additive Manufactured Metals: Issues to Consider and Perspective for Future Research, Procedia Eng. 213 (2018) 5–16. https://doi.org/10.1016/j.proeng.2018.02.002.

[135] Y. Yamashita, T. Murakami, R. Mihara, M. Okada, Y. Murakami, Defect analysis and fatigue design basis for Ni-based superalloy 718 manufactured by selective laser melting, Int J Fatigue. 117 (2018) 485–495. https://doi.org/10.1016/j.ijfatigue.2018.08.002.

[136] N. Sanaei, A. Fatemi, N. Phan, Defect characteristics and analysis of their variability in metal L-PBF additive manufacturing, Mater Des. 182 (2019) 108091. https://doi.org/10.1016/j.matdes.2019.108091.

[137] J. Tenkamp, M. Awd, S. Siddique, P. Starke, F. Walther, Fracture–mechanical assessment of the effect of defects on the fatigue lifetime and limit in cast and additively manufactured aluminum–silicon alloys from hcf to vhcf regime, Metals (Basel). 10 (2020) 1–18. https://doi.org/10.3390/met10070943.

[138] S. Romano, S. Miccoli, S. Beretta, A new FE post-processor for probabilistic fatigue assessment in the presence of defects and its application to AM parts, Int J Fatigue. 125 (2019) 324–341. https://doi.org/10.1016/j.ijfatigue.2019.04.008.

[139] G. Meneghetti, D. Rigon, C. Gennari, An analysis of defects influence on axial fatigue strength of maraging steel specimens produced by additive manufacturing, Int J Fatigue. 118 (2019) 54–64. https://doi.org/10.1016/J.IJFATIGUE.2018.08.034.

[140] A. du Plessis, S. Beretta, Killer notches: The effect of as-built surface roughness on fatigue failure in AlSi10Mg produced by laser powder bed fusion, Addit Manuf. 35 (2020) 101424. https://doi.org/10.1016/J.ADDMA.2020.101424.

[141] Y. Murakami, Metal fatigue: Effects of small defects and nonmetallic inclusions, Metal Fatigue: Effects of Small Defects and Nonmetallic Inclusions. (2019) 1–758. https://doi.org/10.1016/C2016-0-05272-5.

[142] M.H. el Haddad, T.H. Topper, K.N. Smith, Prediction of non propagating cracks, Eng Fract Mech. 11 (1979) 573–584. https://doi.org/10.1016/0013-7944(79)90081-X.

[143] L. Du, G. Qian, L. Zheng, Y. Hong, Influence of processing parameters of selective laser melting on high-cycle and very-high-cycle fatigue behaviour of Ti-6Al-4V, Fatigue Fract Eng Mater Struct. 44 (2021) 240–256. https://doi.org/10.1111/ffe.13361.

[144] M. Zhang, C.N. Sun, X. Zhang, J. Wei, D. Hardacre, H. Li, Predictive models for fatigue property of laser powder bed fusion stainless steel 316L, Mater Des. 145 (2018) 42–54. https://doi.org/10.1016/j.matdes.2018.02.054.

[145] P. Ferro, A. Fabrizi, F. Berto, G. Savio, R. Meneghello, S. Rosso, Defects as a root cause of fatigue weakening of additively manufactured AlSi10Mg components, Theoretical and Applied Fracture Mechanics. 108 (2020) 102611. https://doi.org/10.1016/J.TAFMEC.2020.102611.

[146] M. Tang, P.C. Pistorius, Fatigue life prediction for AlSi10Mg components produced by selective laser melting, Int J Fatigue. 125 (2019) 479–490. https://doi.org/10.1016/J.IJFATIGUE.2019.04.015.

[147] Z. Zhan, H. Li, A novel approach based on the elastoplastic fatigue damage and machine learning models for life prediction of aerospace alloy parts fabricated by additive manufacturing, Int J Fatigue. 145 (2021) 106089. https://doi.org/10.1016/J.IJFATIGUE.2020.106089.

[148] E. Maleki, S. Bagherifard, S.M.J. Razavi, M. Bandini, A. du Plessis, F. Berto, M. Guagliano, On the efficiency of machine learning for fatigue assessment of post-processed additively manufactured AlSi10Mg, Int J Fatigue. 160 (2022) 106841. https://doi.org/10.1016/j.ijfatigue.2022.106841.

[149] J. Chen, Y. Liu, Fatigue property prediction of additively manufactured Ti-6Al-4V using probabilistic physics-guided learning, Addit Manuf. 39 (2021) 101876. https://doi.org/10.1016/J.ADDMA.2021.101876.

[150] J. Li, Z. Yang, G. Qian, F. Berto, Machine learning based very-high-cycle fatigue life prediction of Ti-6Al-4V alloy fabricated by selective laser melting, Int J Fatigue. 158 (2022). https://doi.org/10.1016/J.IJFATIGUE.2022.106764.

[151] A. Ciampaglia, A. Tridello, D.S. Paolino, F. Berto, Data driven method for predicting the effect of process parameters on the fatigue response of additive manufactured AlSi10Mg parts, Int J Fatigue. 170 (2023) 107500. https://doi.org/10.1016/J.IJFATIGUE.2023.107500.

[152] N. Sanaei, A. Fatemi, Defects in additive manufactured metals and their effect on fatigue performance: A state-of-the-art review, Prog Mater Sci. 117 (2021) 100724. https://doi.org/10.1016/J.PMATSCI.2020.100724.

[153] L. Du, G. Qian, L. Zheng, Y. Hong, Influence of processing parameters of selective laser melting on high-cycle and very-high-cycle fatigue behaviour of Ti-6Al-4V, Fatigue Fract Eng Mater Struct. 44 (2021) 240–256. https://doi.org/10.1111/ffe.13361.

[154] A. Tridello, J. Fiocchi, C.A. Biffi, G. Chiandussi, M. Rossetto, A. Tuissi, D.S. Paolino, Effect of microstructure, residual stresses and building orientation on the fatigue response up to 109 cycles of an SLM AlSi10Mg alloy, Int J Fatigue. 137 (2020). https://doi.org/10.1016/j.ijfatigue.2020.105659.

[155] G. Qian, Y. Li, D.S. Paolino, A. Tridello, F. Berto, Y. Hong, Very-high-cycle fatigue behavior of Ti-6Al-4V manufactured by selective laser melting: Effect of build orientation, Int J Fatigue. 136 (2020) 105628. https://doi.org/10.1016/j.ijfatigue.2020.105628.

[156] T. Mukherjee, T. DebRoy, Mitigation of lack of fusion defects in powder bed fusion additive manufacturing, J Manuf Process. 36 (2018) 442–449. https://doi.org/10.1016/j.jmapro.2018.10.028.

[157] M. Tang, P.C. Pistorius, Fatigue life prediction for AlSi10Mg components produced by selective laser melting, Int J Fatigue. 125 (2019) 479–490. https://doi.org/10.1016/j.ijfatigue.2019.04.015.

[158] A. Tridello, C. Boursier Niutta, F. Berto, G. Qian, D.S. Paolino, Fatigue failures from defects in additive manufactured components: A statistical methodology for the analysis of the experimental results, Fatigue Fract Eng Mater Struct. 44 (2021) 1944–1960. https://doi.org/10.1111/ffe.13467.

[159] M. Tang, P.C. Pistorius, Fatigue life prediction for AlSi10Mg components produced by selective laser melting, Int J Fatigue. 125 (2019) 479–490. https://doi.org/10.1016/J.IJFATIGUE.2019.04.015.

[160] C. Fischer, C. Schweizer, Lifetime assessment of the process-dependent material properties of additive manufactured AlSi10Mg under low-cycle fatigue loading, MATEC Web of Conferences. 326 (2020) 07003. https://doi.org/10.1051/matecconf/202032607003.

[161] J.G. Santos Macías, T. Douillard, L. Zhao, E. Maire, G. Pyka, A. Simar, Influence on microstructure, strength and ductility of build platform temperature during laser powder bed fusion of AlSi10Mg, Acta Mater. 201 (2020) 231–243. https://doi.org/10.1016/j.actamat.2020.10.001.

[162] A. Soltani-Tehrani, M.S. Yasin, S. Shao, M. Haghshenas, N. Shamsaei, Effects of Powder Particle Size on Fatigue Performance of Laser Powder-Bed Fused Ti-6Al-4V, Procedia Structural Integrity. 38 (2022) 84–93. https://doi.org/10.1016/j.prostr.2022.03.010.

[163] Z.M. Jian, G.A. Qian, D.S. Paolino, A. Tridello, F. Berto, Y.S. Hong, Crack initiation behavior and fatigue performance up to very-high-cycle regime of AlSi10Mg fabricated by selective laser melting with two powder sizes, Int J Fatigue. 143 (2021) 106013. https://doi.org/10.1016/J.IJFATIGUE.2020.106013.

[164] M. Zavala-Arredondo, T. London, M. Allen, T. Maccio, S. Ward, D. Griffiths, A. Allison, P. Goodwin, C. Hauser, Use of power factor and specific point energy as design parameters in laser powder-bed-fusion

(L-PBF) of AlSi10Mg alloy, Mater Des. 182 (2019). https://doi.org/10.1016/j.matdes.2019.108018.

[165] C. Weingarten, D. Buchbinder, N. Pirch, W. Meiners, K. Wissenbach, R. Poprawe, Formation and reduction of hydrogen porosity during selective laser melting of AlSi10Mg, J Mater Process Technol. 221 (2015) 112–120. https://doi.org/10.1016/j.jmatprotec.2015.02.013.

[166] K. Solberg, D. Wan, F. Berto, Fatigue assessment of as-built and heat-treated Inconel 718 specimens produced by additive manufacturing including notch effects, Fatigue Fract Eng Mater Struct. 43 (2020) 2326–2336. https://doi.org/10.1111/ffe.13300.

[167] E. Brandl, U. Heckenberger, V. Holzinger, D. Buchbinder, Additive manufactured AlSi10Mg samples using Selective Laser Melting (SLM): Microstructure, high cycle fatigue, and fracture behavior, Mater Des. 34 (2012) 159–169. https://doi.org/10.1016/J.MATDES.2011.07.067.

[168] G. Qian, Z. Jian, Y. Qian, X. Pan, X. Ma, Y. Hong, Very-high-cycle fatigue behavior of AlSi10Mg manufactured by selective laser melting: Effect of build orientation and mean stress, Int J Fatigue. 138 (2020) 105696. https://doi.org/10.1016/J.IJFATIGUE.2020.105696.

[169] M. Awd, S. Siddique, J. Johannsen, C. Emmelmann, F. Walther, Very high-cycle fatigue properties and microstructural damage mechanisms of selective laser melted AlSi10Mg alloy, Int J Fatigue. 124 (2019) 55–69. https://doi.org/10.1016/J.IJFATIGUE.2019.02.040.

[170] J. Tenkamp, M. Awd, S. Siddique, P. Starke, F. Walther, Fracture–Mechanical Assessment of the Effect of Defects on the Fatigue Lifetime and Limit in Cast and Additively Manufactured Aluminum–Silicon Alloys from HCF to VHCF Regime, Metals 2020, Vol. 10, Page 943. 10 (2020) 943. https://doi.org/10.3390/MET10070943.

[171] A. Tridello, J. Fiocchi, C.A. Biffi, G. Chiandussi, M. Rossetto, A. Tuissi, D.S. Paolino, Effect of microstructure, residual stresses and building orientation on the fatigue response up to 109 cycles of an SLM AlSi10Mg alloy, Int J Fatigue. 137 (2020) 105659. https://doi.org/10.1016/j.ijfatigue.2020.105659.

[172] N.E. Uzan, R. Shneck, O. Yeheskel, N. Frage, Fatigue of AlSi10Mg specimens fabricated by additive manufacturing selective laser melting (AM-SLM), Materials Science and Engineering: A. 704 (2017) 229–237. https://doi.org/10.1016/J.MSEA.2017.08.027.

[173] N.E. Uzan, S. Ramati, R. Shneck, N. Frage, O. Yeheskel, On the effect of shot-peening on fatigue resistance of AlSi10Mg specimens fabricated by additive manufacturing using selective laser melting (AM-SLM), Addit Manuf. 21 (2018) 458–464. https://doi.org/10.1016/J.ADDMA.2018.03.030.

[174] Z. Wu, S. Wu, J. Bao, W. Qian, S. Karabal, W. Sun, P.J. Withers, The effect of defect population on the anisotropic fatigue resistance of AlSi10Mg alloy fabricated by laser powder bed fusion, Int J Fatigue. 151 (2021) 106317. https://doi.org/10.1016/J.IJFATIGUE.2021.106317.

[175] H. Masuo, Y. Tanaka, S. Morokoshi, H. Yagura, T. Uchida, Y. Yamamoto, Y. Murakami, Influence of defects, surface roughness and HIP on the fatigue strength of Ti-6Al-4V manufactured by additive manufacturing, Int J Fatigue. 117 (2018) 163–179. https://doi.org/10.1016/J.IJFATIGUE.2018.07.020.

[176] D.S. Paolino, A. Tridello, G. Chiandussi, M. Rossetto, S-N curves in the very-high-cycle fatigue regime: statistical modeling based on the hydrogen embrittlement consideration ORIGINAL CONTRIBUTION, (2016). https://doi.org/10.1111/ffe.12431.

[177] H. Mayer, R. Schuller, M. Fitzka, D. Tran, B. Pennings, Very high cycle fatigue of nitrided 18Ni maraging steel sheet, Int J Fatigue. 64 (2014) 140–146. https://doi.org/10.1016/J.IJFATIGUE.2014.02.003.

[178] A. Tridello, C. Boursier Niutta, M. Rossetto, F. Berto, D.S. Paolino, Statistical models for estimating the fatigue life, the stress–life relation, and the P-S–N curves of metallic materials in Very High Cycle Fatigue: A review, Fatigue Fract Eng Mater Struct. 45 (2022) 332–370. https://doi.org/10.1111/FFE.13610.

[179] A. Tridello, J. Fiocchi, C.A. Biffi, G. Chiandussi, M. Rossetto, A. Tuissi, D.S. Paolino, Effect of microstructure, residual stresses and

building orientation on the fatigue response up to 109 cycles of an SLM AlSi10Mg alloy, Int J Fatigue. 137 (2020) 105659. https://doi.org/10.1016/J.IJFATIGUE.2020.105659.

[180] S. Siddique, M. Imran, F. Walther, Very high cycle fatigue and fatigue crack propagation behavior of selective laser melted AlSi12 alloy, Int J Fatigue. 94 (2017) 246–254. https://doi.org/10.1016/j.ijfatigue.2016.06.003.

[181] C. Colombo, C.A. Biffi, J. Fiocchi, D. Scaccabarozzi, B. Saggin, A. Tuissi, L.M. Vergani, Modulating the damping capacity of SLMed AlSi10Mg trough stress-relieving thermal treatments, Theoretical and Applied Fracture Mechanics. 107 (2020) 1–6. https://doi.org/10.1016/j.tafmec.2020.102537.

[182] A. Tridello, J. Fiocchi, C.A. Biffi, G. Chiandussi, M. Rossetto, A. Tuissi, D.S. Paolino, Effect of microstructure, residual stresses and building orientation on the fatigue response up to 109 cycles of an SLM AlSi10Mg alloy, Int J Fatigue. 137 (2020) 105659. https://doi.org/10.1016/j.ijfatigue.2020.105659.

[183] M. Awd, S. Siddique, J. Johannsen, C. Emmelmann, F. Walther, Very high-cycle fatigue properties and microstructural damage mechanisms of selective laser melted AlSi10Mg alloy, Int J Fatigue. 124 (2019) 55–69. https://doi.org/10.1016/J.IJFATIGUE.2019.02.040.

[184] F. Maschinenbau, Analytical strength assessment of components : made of steel, cast iron and aluminum materials in mechanical engineering ; FKM Guideline, 2013.

[185] C.M. Sonsino, Course of SN-curves especially in the high-cycle fatigue regime with regard to component design and safety, Int J Fatigue. 29 (2007) 2246–2258. https://doi.org/10.1016/j.ijfatigue.2006.11.015.

[186] S. Romano, A. Brückner-Foit, A. Brandão, J. Gumpinger, T. Ghidini, S. Beretta, Fatigue properties of AlSi10Mg obtained by additive manufacturing: Defect-based modelling and prediction of fatigue strength, Eng Fract Mech. 187 (2018) 165–189. https://doi.org/10.1016/j.engfracmech.2017.11.002.

[187] E. Brandl, U. Heckenberger, V. Holzinger, D. Buchbinder, Additive manufactured AlSi10Mg samples using Selective Laser Melting (SLM): Microstructure, high cycle fatigue, and fracture behavior, Mater Des. 34 (2012) 159–169. https://doi.org/10.1016/J.MATDES.2011.07.067.

[188] M. Tang, P.C. Pistorius, Fatigue life prediction for AlSi10Mg components produced by selective laser melting, Int J Fatigue. 125 (2019) 479–490. https://doi.org/10.1016/J.IJFATIGUE.2019.04.015.

[189] F. Sausto, C. Tezzele, S. Beretta, Analysis of Fatigue Strength of L-PBF AlSi10Mg with Different Surface Post-Processes: Effect of Residual Stresses, Metals (Basel). 12 (2022) 898. https://doi.org/10.3390/met12060898.

[190] H. Moulinec, P. Suquet, A fast numerical method for computing the linear and nonlinear mechanical properties of composites, (n.d.). https://hal.science/hal-03019226 (accessed February 17, 2023).